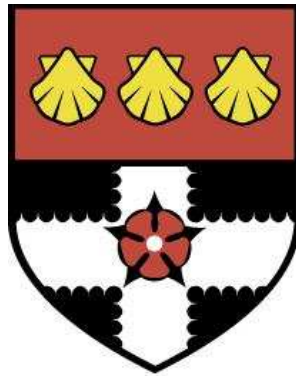


THE UNIVERSITY OF READING

Department of Meteorology



**Boundary-Layer Processes in  
Mid-latitude Cyclones**

IAN BOUTLE

A thesis submitted for the degree of Doctor of Philosophy

October 2009

# DECLARATION

I confirm that this is my own work and the use of all material from other sources has been properly and fully acknowledged.

Ian Boutle

# ABSTRACT

The atmospheric boundary layer is known to affect the development of mid-latitude cyclones, but exactly how do boundary-layer dynamics communicate surface effects to the free troposphere? Cyclones are key contributors to the transport of atmospheric water vapour, but less is known about the role of the boundary layer in this transport. These questions are answered using the Met Office Unified Model to simulate idealised cyclones.

The mechanism by which the boundary layer spins down a cyclone is investigated. Ekman pumping is compared to a recently-proposed baroclinic potential vorticity (PV) mechanism, and it is shown that both mechanisms work together to spin down the cyclone. Ekman pumping aids the ventilation of PV from the boundary layer, and shapes the resulting PV anomaly into one of increased static stability, which then damps the cyclone growth rate. Different sea-surface temperature distributions are used to demonstrate why surface sensible heat fluxes only affect cyclone spin down when the PV generated is well-placed for ventilation.

Secondly, the processes controlling moisture transport within the cyclone are investigated, in order to identify the roles of boundary-layer processes and large-scale dynamics. A budgeting technique demonstrates that moisture is evaporated from the ocean behind the cold front and transported large distances within the boundary layer into the footprint of the warm-conveyor belt (WCB). The WCB forms one of the two main processes of boundary-layer ventilation, with shallow cumulus convection being of similar importance. Once ventilated, moisture can be transported eastwards and polewards by the cyclone, before being returned to the surface as precipitation.

Finally, scaling arguments are presented to quantify the dependence of moisture transport on large-scale and boundary-layer parameters. It is shown that ventilation varies strongly with atmospheric temperature and the meridional temperature gradient. Ventilation by shallow convection and WCB advection vary in the same way with changes to large-scale parameters, but in a markedly different way when boundary-layer parameters are changed.

# ACKNOWLEDGEMENTS

My first acknowledgement must go to my supervisors – Stephen Belcher and Bob Plant. They have gladly shared their wealth of experience and knowledge with me, helping with every aspect of this project. Thanks also go to my CASE supervisors – Andy Brown and Bob Beare. They provided technical support with the Unified Model, and also gave a fresh perspective on many problems when it was required. I must also thank my monitoring committee – Anthony Illingworth and Sue Gray, for quizzing me in detail on many aspects of my thesis and making me think deeply about how and why I had approached some problems.

Thanks to the occupants of 2U06 for being the coolest office in the department, and to the PhD students past and present for many coffee breaks, pub crawls, pantomimes etc, which were excellent distractions from real work!

My final thanks must go to my family, for giving me such an enjoyable place to go home to. To Mum and Dad for supporting me through too many years of university, and to Mark and Samantha for making the last few months a lot less stressful. Finally, I cannot thank Sam enough, not only for all her reminders that I didn't have a real job, but mainly for all her love and support over the years.

- Ian Boutle - October 2009

# CONTENTS

<b>1</b>	<b>INTRODUCTION</b>	<b>1</b>
1.1	INTRODUCTION . . . . .	1
1.2	MID-LATITUDE CYCLOGENESIS . . . . .	2
1.2.1	BAROCLINIC INSTABILITY . . . . .	3
1.2.2	THE EADY MODEL . . . . .	5
1.2.3	NONLINEAR STUDIES . . . . .	7
1.3	CONCEPTUAL MODELS OF MID-LATITUDE CYCLONES . . . . .	8
1.3.1	CYCLONE STRUCTURE . . . . .	8
1.3.2	TYPE-A AND TYPE-B CYCLOGENESIS . . . . .	10
1.4	FRICTIONAL EFFECTS ON CYCLOGENESIS . . . . .	11
1.4.1	EKMAN PUMPING . . . . .	11
1.4.2	POTENTIAL VORTICITY . . . . .	13
1.5	MOIST CYCLOGENESIS . . . . .	15
1.6	THESIS OUTLINE . . . . .	17
<b>2</b>	<b>IDEALISED CYCLONE-WAVE LIFE CYCLES</b>	<b>20</b>
2.1	INTRODUCTION . . . . .	20

2.2	OVERVIEW OF THE METUM . . . . .	21
2.2.1	LARGE-SCALE DYNAMICS . . . . .	21
2.2.2	PHYSICAL PARAMETERISATIONS . . . . .	22
2.3	THE ATMOSPHERIC BOUNDARY LAYER . . . . .	24
2.3.1	REYNOLDS DECOMPOSITION . . . . .	24
2.3.2	SURFACE FLUXES . . . . .	25
2.3.3	FLUXES IN THE BOUNDARY LAYER INTERIOR . . . . .	29
2.3.4	DEFINITION OF THE BOUNDARY-LAYER TOP . . . . .	32
2.4	DRY TYPE-A LIFE CYCLES . . . . .	33
2.4.1	INITIALISATION . . . . .	33
2.4.2	DYNAMICS ONLY LIFE CYCLES . . . . .	35
2.4.3	DRY LIFE-CYCLE WITH BOUNDARY LAYER . . . . .	38
2.5	MOIST TYPE-A LIFE CYCLES . . . . .	40
2.5.1	INITIALISATION AND LIFE CYCLES WITHOUT A BOUNDARY LAYER . . . . .	40
2.5.2	MOIST LIFE-CYCLE WITH BOUNDARY LAYER . . . . .	45
2.5.3	INCLUSION OF RADIATION . . . . .	47
2.6	TYPE-B LIFE CYCLES . . . . .	49
2.6.1	DRY SIMULATIONS . . . . .	49
2.6.2	MOIST SIMULATIONS . . . . .	51
2.7	SUMMARY . . . . .	52

<b>3</b>	<b>BOUNDARY-LAYER PROCESSES IN DRY LIFE CYCLES</b>	<b>54</b>
3.1	INTRODUCTION . . . . .	54
3.2	FRICTION ONLY SIMULATIONS . . . . .	56
3.2.1	BAROTROPIC VORTEX . . . . .	56
3.2.2	EADY MODEL . . . . .	59
3.2.3	TYPE-A CYCLOGENESIS . . . . .	62
3.2.4	TYPE-B CYCLOGENESIS . . . . .	64
3.3	SURFACE HEAT-FLUX EFFECTS . . . . .	66
3.4	PV INVERSION . . . . .	71
3.4.1	INVERSION TECHNIQUE . . . . .	71
3.4.2	INVERSION RESULTS . . . . .	72
3.4.3	PROBLEMS WITH PV INVERSION . . . . .	76
3.5	INTERACTION BETWEEN MECHANISMS . . . . .	77
3.5.1	BOUNDARY-LAYER MODIFICATION . . . . .	77
3.5.2	SURFACE ROUGHNESS EFFECTS . . . . .	80
3.6	CONCLUSIONS . . . . .	81
<b>4</b>	<b>BOUNDARY-LAYER PROCESSES IN MOIST LIFE CYCLES</b>	<b>84</b>
4.1	INTRODUCTION . . . . .	84
4.2	BOUNDARY-LAYER STRUCTURE . . . . .	86
4.2.1	SURFACE FLUXES . . . . .	86

4.2.2	BOUNDARY-LAYER STRUCTURE . . . . .	88
4.3	MOISTURE REGIMES . . . . .	91
4.4	BOUNDARY-LAYER BUDGETS . . . . .	93
4.4.1	DERIVATION OF MOISTURE BUDGET . . . . .	93
4.4.2	APPLICATION OF MOISTURE BUDGET . . . . .	95
4.5	MOISTURE CYCLE OF A CYCLONE-WAVE . . . . .	99
4.6	CONCLUSIONS . . . . .	103
<b>5</b>	<b>FACTORS CONTROLLING CYCLONE MOISTURE TRANSPORT</b>	<b>107</b>
5.1	INTRODUCTION . . . . .	107
5.2	LARGE-SCALE CONTROLS . . . . .	109
5.2.1	RELATIVE HUMIDITY . . . . .	110
5.2.2	ABSOLUTE TEMPERATURE . . . . .	114
5.2.3	MERIDIONAL TEMPERATURE GRADIENT . . . . .	116
5.3	SCALING MOISTURE VENTILATION . . . . .	118
5.3.1	SCALING VENTILATION BY THE WARM CONVEYOR BELT . . . . .	118
5.3.2	SCALING VENTILATION BY SHALLOW CONVECTION . . . . .	121
5.3.3	COMPARISON OF SCALINGS WITH SIMULATIONS . . . . .	122
5.4	SURFACE MOISTURE AVAILABILITY . . . . .	125
5.5	CONCLUSIONS . . . . .	129
<b>6</b>	<b>CONCLUSIONS</b>	<b>132</b>

6.1	SUMMARY AND MAIN CONCLUSIONS . . . . .	132
6.2	FUTURE WORK . . . . .	136
<b>A</b>	<b>NOMENCLATURE</b>	<b>139</b>
A.1	SYMBOLS AND PHYSICAL CONSTANTS . . . . .	139
A.2	MATHEMATICAL OPERATORS . . . . .	143
A.3	SUBSCRIPTS AND SUPERSCRIPTS . . . . .	143
A.4	ABBREVIATIONS . . . . .	144
	<b>BIBLIOGRAPHY</b>	<b>145</b>

# CHAPTER 1:

# INTRODUCTION

## 1.1 INTRODUCTION

Extratropical cyclones are everyday phenomena that drive the weather over much of the Earth's mid-latitude regions. Much of this weather tends to be benign (e.g. cloudiness and showers), but occasionally strong cyclones can bring gales and torrential rains, which can have significant socio-economic impacts (Burt and Mansfield, 1988; Fink *et al.*, 2009). They are also of considerable climatological importance, forming a crucial part of the atmospheric heat engine (Barry *et al.*, 2002), transporting large amounts of heat and moisture polewards.

The scientific study of mid-latitude cyclones began in the early 20th century with the work of Bjerknes (1919) and Bjerknes and Solberg (1922) at the Bergen School of Meteorology. They provided the first conceptual model of the life-cycle of an extratropical cyclone, describing how cyclones form as disturbances to the polar front. The pioneering work of Charney (1947) and Eady (1949) added mathematical rigour to the Bergen School concepts, introducing the theory of cyclone formation due to baroclinic instability. The age of supercomputers allowed non-linear simulations of cyclogenesis to be performed (e.g. Simmons and Hoskins, 1976, 1978). These studies were able to demonstrate how cyclones could form and dissipate due to large-scale, dynamical processes, and as computational resources grew, so did the level of complexity within the models, allowing physical processes to be modelled and their effects on cyclogenesis understood. Meanwhile, conceptual models of cyclogenesis (Browning, 1985; Shapiro and Keyser, 1990) continued to be improved, utilising remote sensing techniques such as radar and satellite to provide a detailed description of the winds, clouds and precipitation organised within a mid-latitude cyclone.

This thesis aims to understand, in a systematic way, the affect of near-surface atmospheric physics on cyclone evolution. How do surface characteristics influence the cyclone dynamics?

How are these characteristics transmitted through the atmospheric boundary layer into the free troposphere? Understanding how near-surface physics is communicated to the cyclone interior is important for accurate representation of cyclones in numerical weather prediction (NWP) models. One key variable of interest is moisture. Most water is contained on the Earth's surface, but evaporation and precipitation processes continually cycle moisture between the atmosphere and surface. What role do cyclones play in this process? How does the moisture transported by the cyclone feed back onto the cyclone development?

Atmospheric water vapour is a key variable in the climate system, and with the current and anticipated changes taking place in the global climate, a key research objective is to “develop an integrated, quantitative understanding of the changes taking place in the global water cycle” (Natural Environment Research Council, 2009, p. 3). Therefore, this thesis aims to contribute to this objective by providing a quantitative understanding of the water cycle in an extratropical cyclone. Current climate projections suggest that as the climate evolves, the total number of extratropical cyclones will reduce, but there will be more extreme events (Meehl *et al.*, 2007). However, there is uncertainty in these projections, with climate models giving differing results (Bengtsson *et al.*, 2006). An improved understanding of moisture feedbacks at the scale of an individual storm should uncover which physical processes are important in determining how cyclones react to different climatological conditions.

The remainder of this introductory chapter reviews the current state of the literature, discussing what can be considered to be well understood and where room for improvement exists. Some specific thesis questions and objectives are then given in Section 1.6.

## **1.2 MID-LATITUDE CYCLOGENESIS**

The orientation and orbit of our planet results in more solar radiation being incident at the equator than the pole. The equator is therefore warmed to a greater extent than the pole, producing a meridional temperature gradient. This forms the basis of the atmospheric heat engine, and mid-latitude cyclones form in response to this unstable basic state, mixing warm air polewards and cold air equatorwards, reducing the temperature gradient.

Formally, the meridional temperature gradient produces a mid-latitude jet in thermal wind balance with it<sup>1</sup>

$$\frac{\partial \theta}{\partial y} = \frac{-f\theta}{g} \frac{\partial u}{\partial z} \Rightarrow u(z) = - \int_0^z \frac{g}{f\theta} \frac{\partial \theta}{\partial y} dz, \quad (1.1)$$

where  $u$  is the zonal windspeed,  $\theta$  is the potential temperature,  $f$  is the Coriolis parameter and  $g$  is the gravitational acceleration. This jet stores a large amount of potential energy, and small perturbations to it can quickly grow into cyclones, feeding off this reservoir of potential energy and converting it into eddy kinetic energy (James, 1994, Chapter 5). The basic mechanism for this is “baroclinic instability”.

### 1.2.1 BAROCLINIC INSTABILITY

The mechanism of baroclinic instability can be best explained in terms of potential vorticity (PV), a concept first introduced by Rossby (1940) and Ertel (1942). The Ertel-Rossby PV is defined as

$$PV = \frac{1}{\rho} \zeta \cdot \nabla \theta, \quad (1.2)$$

where  $\rho$  is the density of air and  $\zeta$  is the absolute vorticity. Ertel’s theorem (Ertel, 1942) proves that for frictionless, adiabatic fluid motion, the PV is conserved following a fluid parcel, i.e.  $\frac{D(PV)}{Dt} = 0$ . Typically, the PV in the troposphere is small and positive (of order  $10^{-7} \text{ Kkg}^{-1}\text{m}^2\text{s}^{-1} = 0.1 \text{ PVU}$ ), driven by a positive vertical component of absolute vorticity, from the Coriolis force ( $\zeta_z \approx f \sim 10^{-4} \text{ s}^{-1}$ ), and a small increase in potential temperature with height ( $\frac{\partial \theta}{\partial z} \sim 10^{-3} \text{ Km}^{-1}$ ). However, within the stratosphere, the PV is much higher due to much stronger vertical temperature gradients ( $\frac{\partial \theta}{\partial z} \sim 10^{-2} \text{ Km}^{-1}$ ). Due to the conservation property, the stratosphere can be thought of as a “reservoir” of high PV that can influence the dynamics of the troposphere.

Figure 1.1 shows schematically the PV views of how baroclinic instability leads to cyclone formation. A small southwards or downwards perturbation at the tropopause could lead to some high PV air moving from the stratosphere into the troposphere. This air has higher PV than its surroundings, and will have both increased relative vorticity ( $\xi$ ) and increased static stability ( $N^2 = \frac{g}{\theta} \frac{\partial \theta}{\partial z}$ ) associated with it. Figure 1.1(a) shows this positive PV anomaly at the tropopause,

---

<sup>1</sup>Here and throughout this thesis standard meteorological symbols are used. All symbols and mathematical notation are defined in Appendix A and numerical values given for any constants.

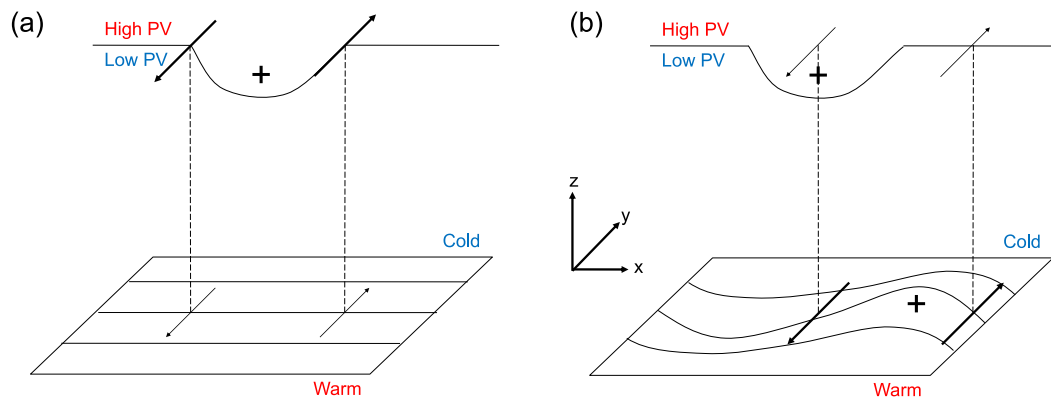


**Figure 1.1** Schematic showing contours of near-surface temperature and the tropopause location, with + indicating the location of positive PV anomalies and arrows indicating the location and strength of airflows associated with PV anomalies. (a) The effect of a tropopause PV anomaly on the surface temperature field. (b) The effect of a surface temperature anomaly on the tropopause PV field. See text for further description.

with the thick arrows showing the positive cyclonic circulation associated with it. A second key property of PV is the “invertibility principle” (Hoskins *et al.*, 1985), which states that given a global PV distribution, an appropriate balance condition for the flow (e.g. geostrophic balance) and complete boundary conditions, the PV distribution can be inverted to obtain the wind and potential temperature fields everywhere in the domain. A direct consequence of this is “action at a distance” – since the positive PV anomaly has cyclonic vorticity associated with it, this vorticity does not just stop at the edge of the anomaly, but extends throughout the depth of the troposphere, decaying in magnitude with distance from the anomaly. This causes the PV anomaly to create a weak cyclonic vorticity at the surface, shown by the thin arrows in Figure 1.1(a).

The surface circulation acts to distort the surface meridional temperature gradient, moving warm air polewards ahead of the PV anomaly, and cold air equatorwards behind the anomaly. This results in a distorted pattern of surface temperature, as shown in Figure 1.1(b). Bretherton (1966) discusses how a warm anomaly in the surface temperature field has the same dynamic affect as a positive PV anomaly located below the surface. The surface temperature anomaly can be thought of as a manifestation of the increased static stability associated with this PV anomaly, and there must also be a cyclonic circulation associated with it, which is shown by the thick arrows in Figure 1.1(b). The action at a distance principle implies that this circulation extends up

to the tropopause, the effect of which is shown by the thin arrows.

Baroclinic instability occurs when, as shown in Figure 1.1, the effect of the surface temperature anomaly is to re-intensify the tropopause PV anomaly which caused it. The two features become phase-locked, mutually intensifying each other and forming a baroclinic wave. The surface warm anomaly, with its cyclonic circulation, forms the low-pressure part of the wave, whilst the surface cold anomaly, which has an anticyclonic circulation associated with it, forms the high-pressure part of the wave.

### 1.2.2 THE EADY MODEL

Charney (1947) and Eady (1949) independently produced mathematical descriptions of baroclinic instability. Focus will be made on the Eady model since it captures the main features of cyclogenesis, but is mathematically simpler than the Charney model. The Eady model utilises the conservation of Quasi-Geostrophic Potential Vorticity (QGPV), which in perturbation form is given by

$$QGPV' = \nabla_2^2 \psi_g + \frac{f^2}{N^2} \frac{\partial^2 \psi_g}{\partial z^2}, \quad (1.3)$$

where  $\psi_g$  is the geostrophic streamfunction and  $\nabla_2$  is the 2D gradient operator  $(\frac{\partial}{\partial x}, \frac{\partial}{\partial y})$ . The QGPV is a simplified form of the Ertel PV (Eqn. 1.2) under the approximations of Quasi-Geostrophic (QG) theory (which assumes that the flow remains close to geostrophic at all times). The Eady model assumes a basic state with zero initial  $QGPV'$  in the interior (i.e. a constant value of the Coriolis parameter,  $f$ ), and a windspeed linearly increasing from zero at the surface ( $z = 0$ ) to  $U$  at the tropopause ( $z = \mathcal{H}$ ). The conservation property implies that  $QGPV' = 0$  for all time, and boundary conditions are applied at the tropopause and the frictionless surface by the linearised thermodynamic equation:

$$f \frac{\partial^2 \psi_g}{\partial t \partial z} + u f \frac{\partial^2 \psi_g}{\partial x \partial z} + \frac{g}{\theta_0} \frac{\partial \theta}{\partial y} \frac{\partial \psi_g}{\partial x} = -N^2 w, \quad (1.4)$$

where  $\theta_0$  is a reference potential temperature and  $w$  is the vertical velocity. The Eady model is solved by assuming  $w = 0$  on the boundaries and seeking normal mode solutions to Equation 1.3:

$$\psi_g = \exp(i(kx - \omega t)) \left( A \cosh \frac{Nk}{f} z + B \sinh \frac{Nk}{f} z \right), \quad (1.5)$$

where  $k$  is the zonal wavenumber,  $\omega$  is the frequency, and  $A$  and  $B$  are constants to be determined. Boundary conditions from Equation 1.4 are given by

$$(-\omega Nk)B + \left(\frac{g}{\theta_0} \frac{\partial \theta}{\partial y} k\right)A = 0, \quad (1.6a)$$

$$\left(-\omega Nkc + Uk^2 Nc + \frac{\partial b}{\partial y} ks\right)B + \left(-\omega Nks + Uk^2 Ns + \frac{g}{\theta_0} \frac{\partial \theta}{\partial y} kc\right)A = 0, \quad (1.6b)$$

where  $s = \sinh\left(\frac{Nk}{f} \mathcal{H}\right)$  and  $c = \cosh\left(\frac{Nk}{f} \mathcal{H}\right)$ . Equations 1.6 are of the form

$$\begin{pmatrix} x & y \\ w & z \end{pmatrix} \begin{pmatrix} A \\ B \end{pmatrix} = \begin{pmatrix} 0 \\ 0 \end{pmatrix}, \quad (1.7)$$

and non-trivial solutions to Equation 1.7 are obtained if the matrix cannot be inverted, i.e.  $xz - wy = 0$ . This yields a quadratic equation for  $\omega$  and the following dispersion relation between  $\omega$  and  $k$ :

$$\omega = \frac{kU}{2} - i \left(\frac{g}{N\theta_0} \frac{\partial \theta}{\partial y}\right) \sqrt{\left(\frac{kL_{R0}}{2} - \tanh \frac{kL_{R0}}{2}\right) \left(\coth \frac{kL_{R0}}{2} - \frac{kL_{R0}}{2}\right)}, \quad (1.8)$$

where  $L_{R0} = N\mathcal{H}/f$  is the Rossby radius of deformation. The first term represents propagation of the wave, whilst the second (complex) term gives the growth rate, the imaginary part of which is often denoted  $\sigma$ .

Equation 1.8 shows that the cyclone growth rate is directly proportional to the meridional temperature gradient  $\left(\frac{\partial \theta}{\partial y}\right)$ . This is as expected, since if there were no meridional temperature gradient, no cyclones would form. It also shows the growth rate to be inversely proportional to the static stability ( $N$ ). This implies that for higher static stabilities, the cyclone growth rate is reduced. This can be understood from the conceptual description of baroclinic instability given in Section 1.2.1. At higher static stabilities, the circulation induced by the PV anomalies cannot extend as far through the depth of the troposphere. Therefore, for a given strength of PV anomaly at the tropopause, the circulation induced by it at the surface is reduced when the static stability is higher. Static stability acts as an effective insulator to the baroclinic instability process. The Eady model can also be used to make predictions about the structure and evolution of cyclones. Applying typical mid-latitude scales to the terms in Equation 1.8 gives the cyclone wavelength as  $2\pi/k \approx 4000$  km and the e-folding time as  $1/\sigma \approx 1$  day, both of which are reasonable values for observed mid-latitude cyclogenesis.

### 1.2.3 NONLINEAR STUDIES

Whilst the Eady model demonstrates the key variables that influence cyclone growth rates, since it is a linear theory it strictly only applies for small perturbations. The atmosphere is a nonlinear system, and therefore cyclones quickly reach a stage in their development when nonlinear processes become important. To simulate the development of cyclones into these nonlinear regimes requires the use of computational models, numerically solving the equations of fluid motion into regimes where analytic solutions do not exist. A series of papers by Simmons and Hoskins (1976, 1977, 1978) investigated the development of cyclones from normal-mode perturbations to the mid-latitude jet (similar to Eqn. 1.5 used in the Eady model), using the Reading Intermediate General Circulation Model (IGCM, Hoskins and Simmons, 1975). These simulations were able to show how cyclones passed beyond the linear growth stage, described by the Eady model, into a nonlinear regime where the growth rate was accelerated. A realistic alternating series of high and low pressure systems is formed, with the low pressure centres migrating polewards and the high pressure centres moving equatorwards. The model is also capable of simulating frontogenesis, with warm and cold fronts forming in the region of the low pressure system. The simulations reach occlusion and are able to represent the transition of the cyclone into a barotropic decay phase.

Thorncroft *et al.* (1993) discussed how two paradigms of nonlinear life-cycle behaviour can be identified. The first type, life-cycle one, denoted LC1, is the nonlinear counterpart of the work of Charney (1947) and Eady (1949) in a spherical geometry. A normal mode perturbation is added to the basic state westerly jet, resulting in the life-cycle discussed above. The poleward motion of the low pressure systems results in the life-cycle being dominated by a strong cold front, with only a small, weak warm front forming. At upper levels, the tropopause PV wave “breaks” anticyclonically at occlusion, causing the system to enter the barotropic decay phase. The second type, denoted LC2, forms on addition of a cyclonic barotropic shear to the basic state jet. This introduces asymmetric development to the wave, with very strong low pressure systems and only weak ridges of high pressure forming. The low pressure is now dominated by a strong warm front, with only a weak cold front. At upper levels, the tropopause PV wave now breaks cyclonically at occlusion, resulting in cut-off cyclones which do not decay. Shapiro *et al.* (1999) discuss how these paradigms represent two extremes of the spectrum of observed life-cycles, with

most cyclogenesis events sitting somewhere between LC1 and LC2.

## **1.3 CONCEPTUAL MODELS OF MID-LATITUDE CYCLONES**

### **1.3.1 CYCLONE STRUCTURE**

Simplified conceptual cyclone models have long been used to illustrate and communicate the complex airflows observed within nature. One of the first conceptual models was the Norwegian cyclone model (Bjerknes and Solberg, 1922), which describes the amplification of a frontal wave to occlusion. Although it was constructed from relatively sparse, surface based observations, the model became the accepted description of cyclone formation for almost 70 years. However, Shapiro and Keyser (1990) were able to use modern remote sensing techniques and many airborne and spaceborne observations to produce a new conceptual model for frontal structure and evolution. Shapiro and Keyser (1990) argue that continuous frontal deformation, as described by Bjerknes and Solberg (1922), rarely occurs. Rather, the front “fractures” near the cyclone centre, with the cold front becoming disjoint from the warm front, as shown in Figure 1.2. The cold front is now oriented perpendicular to the warm front, in what is referred to as a frontal “T-bone”. There is then a “bent-back” extension to the warm front, wrapping around the low centre. Often, as the cyclone continues to develop, warm air becomes trapped near the low centre, encircled by the warm front in what is termed a “warm seclusion”.

There are typically three main airflows, or “conveyor-belts” within mid-latitude cyclones. The first of these is the warm-conveyor belt (WCB, Harold, 1973), which is the main poleward moving airflow. This band of warm, moist air runs ahead of the cold front near the surface, ascending over the warm front and often splitting into two branches. As shown in Figure 1.2, one branch turns cyclonically around the north of the low centre, whilst the other branch turns anticyclonically away from the low. The WCB ascends from near the surface up to  $\sim 7$  km, moving large amounts of moisture which contribute to its associated clouds and precipitation (Browning, 1985). As the cyclone intensifies, the cold front can under-cut the WCB, resulting in heavy precipitation in the frontal region due to the combination of large-scale ascent on the WCB and upright convection in the frontal region.

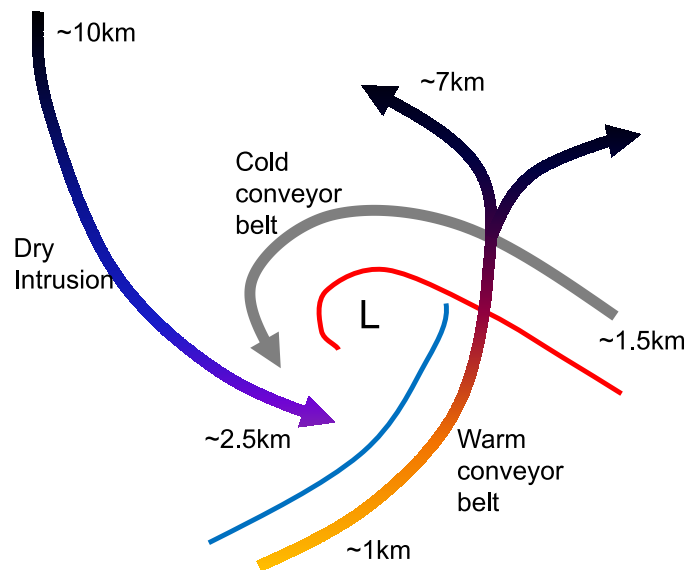


**Figure 1.2** Schematic showing the frontal structure and system-relative airflows within a mid-latitude cyclone. The cold (blue) and warm (red) fronts are shown along with the direction and approximate height of the three main airflows. The arrow colour denotes schematically the height of the airflow, with lighter colours near the surface.

While the WCB originates in the warm air, the cold-conveyor belt (CCB, Carlson, 1980) originates ahead of the warm front in the cold air. As shown in Figure 1.2, the CCB flows westwards relative to the cyclone centre, flowing underneath the WCB and typically staying at low levels. The CCB can ascend and turn anticyclonically (not shown), becoming buoyant as it receives moisture precipitated into it from the WCB. If the CCB stays close to the surface, it typically turns cyclonically, following the bent-back warm front around the low centre. Since it stays close to the surface, it is often termed a low-level jet (LLJ), and can even contribute to the strong winds associated with sting-jets (Clark *et al.*, 2005).

The final airflow shown in Figure 1.2 is the dry intrusion (Reed and Danielsen, 1959), a descending branch of air which originates in the upper troposphere or lower stratosphere. Due to its origin, this airflow contains very little moisture, and can often be seen in satellite images as a region of cloud-free air immediately behind the cold front. Further behind the cold front, especially for marine cyclogenesis, low-level stratocumulus and cumulus clouds can be formed in the cold-air outbreak, as cold air flows quickly from the north over a warmer sea-surface.

These clouds are typically shallow, with tops at  $\sim 3$  km (Neiman and Shapiro, 1993), and this convection can be kept shallow by the much drier air contained within the dry intrusion, which is over-running these low clouds (Browning, 1985).

### **1.3.2 TYPE-A AND TYPE-B CYCLOGENESIS**

Not all cyclogenesis events occur due to small perturbations growing via the baroclinic instability mechanism described in Section 1.2.1. Petterssen and Smebye (1971) describe how large, pre-existing upper-level features can also trigger cyclogenesis. They therefore classify cyclogenesis into two types – A and B.

Type-A is the traditional baroclinic instability mechanism. The upper-level flow is initially zonal, with no significant upper-level PV anomaly. The baroclinicity (meridional temperature gradient) in the lower troposphere is large. As the wave grows, the upper-level PV anomaly develops and intensifies. The tilt between the upper- and lower-level features (shown in Figure 1.1) remains constant in time. The cyclone acts to reduce the baroclinicity in the lower troposphere, resulting in a classical occlusion described in Section 1.3.1.

In Type-B cyclogenesis, the upper-level PV anomaly is initially large, and the baroclinicity in the lower troposphere can be much smaller than for Type-A. Whilst the mutual re-intensification of upper- and lower-level anomalies still occurs, it tends to happen much faster, due to the size of the initial PV anomaly. The tilt between the features decreases with time, ultimately resulting in the two anomalies being vertically aligned. Work by Farrell (1984) and Rotunno and Fantini (1989) has shown how Type-B cyclogenesis can be explained in terms of non-normal modes of the Eady model, demonstrating analytically how an upper-level feature can pass over the surface low pressure, intensifying the system as the trough approaches and weakening once it has passed. A similar cyclone structure and occlusion process to Type-A occurs, but Type-B cyclones often have shorter, more intense life cycles. The frequency of occurrence of Type-A and B cyclones tends to be approximately similar, although the location of their formation tends to be different. Type-A cyclones often form in regions of strong sea-surface temperature (SST) gradients, such as the Gulf Stream or Kuroshio. Type-B cyclones often form in regions with weaker SST gradients, such as the eastern North-Atlantic, or over land, such as in the lee of the Rocky mountains (Gray

and Dacre, 2006).

## **1.4 FRICTIONAL EFFECTS ON CYCLOGENESIS**

Sections 1.2 and 1.3 have discussed the process of cyclogenesis from a dynamical perspective. Sections 1.4 and 1.5 will now discuss how this dynamical process is modified in the presence of atmospheric physics.

### **1.4.1 EKMAN PUMPING**

Traditionally, the effects of surface friction on mid-latitude cyclone development have been explained via the process of Ekman pumping. In frictionless flow, geostrophic balance ensures that air flows parallel to the isobars and cyclonically around a low pressure. However, Ekman (1905) demonstrated that if frictional effects were included, there would be a cross-isobaric flow towards low pressure centres (and away from high pressure centres). The effect of this wind-turning on a vortex is demonstrated schematically in Figure 1.3.

Within the atmospheric boundary layer, wind-turning towards the low pressure centre causes a convergence of low-level winds. By continuity, this converging air must ascend (since it cannot descend), and so a component of vertical velocity is created at the boundary-layer top, often called the “Ekman pumping velocity”. If the cyclonic vortex (shown with solid outline in Fig. 1.3) extends throughout the depth of the troposphere, the Ekman pumping velocity beneath it “squashes” the vortex tube against the rigid-lid created by the tropopause. This results in the dashed cylinder shown in Figure 1.3. By conservation of vorticity, the resulting vortex has a lower relative vorticity, and hence the action of Ekman pumping has spun-down the cyclonic vortex.

This argument is developed for barotropic vortices. However, it is often assumed, at least implicitly, that it is the dominant mechanism for spin-down in baroclinic cyclones. An Ekman pumping boundary-layer parameterisation has been applied to the Eady and Charney models by several authors (e.g. Williams and Robinson, 1974; Card and Barcilon, 1982), demonstrating that within these analytic models, the inclusion of an Ekman pumping velocity as the lower boundary

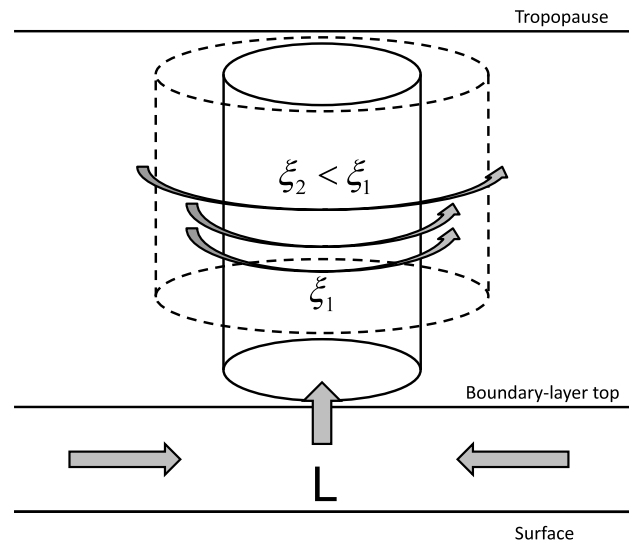


**Figure 1.3** Schematic showing the Ekman pumping mechanism. The arrows denote the direction of the airflow, with the solid cylinder illustrating the initial vortex tube with relative vorticity  $\xi_1$ , and the dashed cylinder illustrating the final vortex tube with relative vorticity  $\xi_2 < \xi_1$

condition reduces the growth rate and phase speed of the baroclinic waves. Valdes and Hoskins (1988) included an Ekman pumping boundary-layer parameterisation into the idealised numerical simulations discussed by Simmons and Hoskins (1976). This simple boundary-layer parameterisation assumed that some vertical velocity through the lower boundary was present in cyclonic regions, and that the magnitude of this velocity was proportional to the vorticity in the interior. Their nonlinear study found similar results to the linear studies with the Eady and Charney models, with a growth rate reduction of  $\approx 40\%$  shown compared to the inviscid simulations. Recently, Beare (2007) investigated the role of the boundary layer in a Type-B cyclone simulation with a state-of-the-art boundary-layer parameterisation. He demonstrated that the cyclone was most sensitive to the boundary layer presence in a location coincident with the greatest Ekman pumping.

However, the question of how and why a barotropic framework can simply be applied to a baroclinic system has not been addressed in any of these studies. The schematic presented in Figure 1.3 does not address important features of the conceptual model of a mid-latitude weather system shown in Figure 1.2. The warm-conveyor belt ascends ahead of the low pressure centre from within the boundary layer, and so it is anticipated that boundary-layer processes will inter-

act with and modify this airflow. Figure 1.2 also shows strong horizontal temperature gradients in frontal regions, which are often associated with horizontal convergence, a large-scale process which is not represented in Figure 1.3. This raises the question of how this large-scale convergence, part of the cyclogenesis process, interacts with the Ekman-convergence thought to cause spin-down. Finally, the Ekman pumping mechanism describes the interaction of the cyclone with the surface via momentum transfer only. However, the atmospheric boundary layer also contains large fluxes of heat, which significantly modify the structure of the boundary layer (Sinclair *et al.*, 2010b). These heat fluxes may also modify the structure of the cyclone, as discussed by Kuo *et al.* (1991) and Reed *et al.* (1993). But these authors do not describe why the surface heat-fluxes produce the observed changes, and the Ekman pumping description has no mechanism to describe how this may occur.

### 1.4.2 POTENTIAL VORTICITY

Adamson *et al.* (2006) addressed the shortcomings of the Ekman pumping mechanism by adopting a potential vorticity framework. Potential vorticity appears to be the natural variable for baroclinic systems, since it contains information on both relative vorticity and temperature gradients. Since Ertel's theorem only applies for frictionless, adiabatic motion, PV can be both created and destroyed within the boundary layer, governed by the following equation:

$$\frac{D(PV)}{Dt} = \frac{1}{\rho} \left( (\nabla \times \mathbf{S}^u) \cdot \nabla \theta + \zeta \cdot \nabla \frac{D\theta}{Dt} \right), \quad (1.9)$$

where  $\mathbf{S}^u$  is the frictional force per unit mass. Adamson *et al.* (2006) utilised the work of Cooper *et al.* (1992) to investigate the mechanisms for generation of PV within the boundary layer, and found three main processes by which PV could be created or destroyed.

The first is the PV interpretation of Ekman pumping. Convergence and ascent near the low centre (Fig. 1.3) leads to a direct reduction of the relative vorticity in this region. The ascent also lifts isentropes away from the surface, reducing the static stability. The combination of these processes appears as the creation of a negative PV anomaly in the boundary layer. The second, baroclinic process, introduces PV generation due to the presence of frontal regions. Within the boundary layer, the horizontal wind must reduce from its geostrophic value at the boundary-layer top, to zero at the surface. This creates a large component of horizontal relative vorticity, which

when coincident with large horizontal temperature gradients in frontal regions, can lead to the generation of a positive PV anomaly. The third mechanism is due to the inclusion of surface heat fluxes, and was discussed by Plant and Belcher (2007). In regions of positive absolute vorticity, negative surface heat fluxes reduce the temperature of near-surface air. This increases the static stability of near surface air (since more isentropes must be packed between the surface and free troposphere), leading to the creation of a positive PV anomaly. Alternatively, positive surface heat fluxes can act to reduce the static stability, creating a negative PV anomaly within the boundary layer.

If PV created within the boundary layer remains within it, the direct effect of vorticity associated with the PV can influence cyclone development. For example, negative PV anomalies created by Ekman processes act in this way, directly reducing the near-surface vorticity of the cyclone. Similarly, positive or negative PV anomalies created by surface heat fluxes could act to deepen or spin-down the cyclone. However, Adamson *et al.* (2006) discuss how the PV can also be advected out of the boundary layer, and its effects on cyclone development can then be markedly different depending on where it is advected to. This is particularly relevant to the baroclinically-generated positive PV anomaly (the second process). This PV generation occurs in the region of the warm-conveyor belt. Once generated, the PV is therefore ventilated from the boundary layer on the WCB and transported vertically and cyclonically by the WCB. The PV then accumulates as a positive PV anomaly above the cyclone centre, with large horizontal extent but trapped between isentropes in the vertical. Hoskins *et al.* (1985) discuss how “flat” PV anomalies like this are mainly associated with increased static stability, and Adamson *et al.* (2006) demonstrate that this positive PV anomaly leads to a 25% increase in the tropospheric static stability. Section 1.2.2 discussed how the cyclone growth rate was inversely proportional to the static stability, and so an increase in static stability, as caused by this positive PV anomaly, leads to a reduced cyclone growth rate. This indirect mechanism, the baroclinic PV mechanism, can therefore lead to a reduction in cyclone intensity by reducing the growth rate.

Whilst the results produced by Adamson *et al.* (2006) and Plant and Belcher (2007) provided an appealing new mechanism that properly accounted for the baroclinic nature of the atmosphere, there remained several unanswered questions. Their studies focussed on LC1 and LC2 cyclones, both of which are realisations of Type-A cyclogenesis. It was not established whether the mecha-

nisms would be applicable to Type-B cyclogenesis, since the timescales involved with generation, transport and accumulation of PV would have to be much faster in a rapidly developing, Type-B system. Plant and Belcher (2007) found that the inclusion of surface heat fluxes did not effect the cyclone development, but they did not investigate how this may change depending on the sea-surface temperature (SST). Their SST had a strong meridional gradient, similar to the Gulf stream region (and hence reasonable for a Type-A cyclone). However, towards the mid and east Atlantic, the meridional SST gradient is much weaker, and this could greatly influence the surface fluxes. Finally, as discussed in Section 1.4.1, previous studies appeared to obtain broadly similar results to those of Adamson *et al.* (2006) by applying an Ekman pumping velocity as the lower boundary condition to an inviscid model. If the dominant spin-down mechanism is via baroclinic PV generation, then why do these studies also see strong spin-down?

## 1.5 MOIST CYCLOGENESIS

The effects of moisture on mid-latitude cyclone development can be understood conceptually in terms of the effect of moisture on the cyclone's PV distribution (Martin, 2006, Chapter 9). As discussed in Section 1.3.1, the warm-conveyor belt ascends ahead of the low pressure centre and typically contains moist air. The temperature cools as the air ascends, leading to the moisture contained within it becoming supersaturated. It condenses out forming clouds and eventually precipitation. As the moisture changes phase from gas to liquid, it releases latent heat, which heats the atmosphere at the location of condensation. The action of heating causes isentropes to be bent downwards in the region of the WCB, leading to increased static stability below the region of heating, and decreased static stability above the region of heating. This results in a positive PV anomaly being created below the heating and a negative PV anomaly being created above. The positive PV anomaly below the heating enhances the circulation of the lower boundary wave (Fig. 1.1(b)), whilst the negative anomaly erodes the PV ahead of the upper-level trough (Fig. 1.1(a)). Both of these effects would appear to suggest that moisture should intensify cyclogenesis.

Emanuel *et al.* (1987) and Whitaker and Davis (1994) extended the Eady model to account for the presence of a moist atmosphere. They demonstrated that the effect of moisture could be

modelled as a reduction in the static stability, which leads to an enhanced growth rate and shorter wavelength of cyclones (Eqn. 1.8). Explicitly, their models assumed that all ascending air was saturated, having near zero static stability, and all descending air was unsaturated, having the background (dry) static stability values. Emanuel *et al.* (1987) considered the semi-geostrophic equation set, demonstrating that with the inclusion of moisture, a more realistic frontal collapse was formed at the surface. Whitaker and Davis (1994) investigated the nonlinear primitive equation set, demonstrating that across this hierarchy of models, the effect of moisture was a consistent intensification when compared to dry simulations.

Further studies by Gutowski *et al.* (1992), Gutowski and Jiang (1998) and Pavan *et al.* (1999) used increasingly realistic parameterisations of precipitation formation and latent heat release to explore in detail how the inclusion of a moist atmosphere modified the energetics and large-scale properties of baroclinic waves in a moist atmosphere. Gutowski and Jiang (1998) included a realistic boundary-layer scheme to enable a discussion of how surface fluxes coupled to cumulus convection within the wave. They described the affect of this cumulus convection on the moisture cycle within a cyclone wave, discussing the potential for shallow cumulus to ventilate moisture from the boundary layer. However, they did not focus on the boundary-layer structure or air-flows in any detail, and did not consider the warm-conveyor belt as an alternative mechanism of boundary-layer ventilation. Pavan *et al.* (1999) investigated the sensitivity of cyclone development to the initial condition humidity profile, showing that changes in this profile can either increase or decrease the cyclone growth rate. They showed that increased moisture at low latitudes led to increased growth rates, but that increased moisture at high latitudes led to decreased growth rates. Explanations for this were given in terms of modifications to the cyclone's energetics, but the transport processes between moisture source and latent-heat release were not investigated and remain obscure.

Ahmadi-Givi *et al.* (2004) investigated the role of latent heat release on a cyclone case study, using PV inversion techniques to ascertain the role of each PV anomaly on the cyclone development. They demonstrated how intense latent heating within the cyclone WCB can force rapid intensification of some cyclones, with the moisture acting as the dominant mechanism for intensification. This led Plant *et al.* (2003) to propose a further classification of cyclones – Type-C. In their Type-C cyclone, a pre-existing upper-level PV anomaly is present, and early stages are

similar to Type-B cyclogenesis. However, the interaction of this upper-level PV anomaly with the surface is small, and the surface wave is relatively unimportant to the cyclogenesis process. Instead, the upper-level PV anomaly interacts with a mid-level, diabatically generated PV anomaly, formed by latent heat release on the WCB. The interaction of these two anomalies can lead to rapid intensification of the cyclone.

It is clear from the above studies that the structure of the warm-conveyor belt is key to accurate forecasting of cyclone evolution. This implies that the moisture content of the WCB must be correctly represented within forecast models. However, none of the above studies have investigated the origin of WCB moisture. Field and Wood (2007) demonstrate through a composite of real cyclone events that WCB precipitation can be linked to boundary-layer moisture convergence. However, a detailed study of boundary-layer structure and moisture flows is needed to reveal the full moisture cycle of baroclinic waves.

## **1.6 THESIS OUTLINE**

As stated in Section 1.1, the overall goal of this thesis is to understand in a systematic way the affect of boundary-layer physics on mid-latitude cyclone evolution. This aim will be broken down into three key questions, one of which will be addressed in each chapter of work. These questions are:

1. What is the mechanism by which the boundary layer spins down a mid-latitude cyclone?
2. How does the cyclone boundary layer link surface moisture fluxes to ventilation into the free troposphere?
3. What factors control the moisture transport within mid-latitude cyclones?

The strategy taken to approach these questions will be one of idealised modelling. This is particularly well suited to the questions given, since an idealised model will allow control to be exerted over the simulations. The model setup can be quickly and easily changed, allowing modification of key parameters to ascertain their importance to the process being studied. For example, the

surface characteristics could be varied to deduce the control they exert on the spin-down, or the atmospheric moisture content could be varied to examine the effect it has on moisture transport.

Idealised modelling has been used in many of the studies discussed in Sections 1.2, 1.4 and 1.5, greatly improving our knowledge about mid-latitude cyclones. Idealised simulations allow “real-world” problems to be simplified: for example, allowing a single cyclone-anticyclone system to be investigated, rather than the complex interaction of several systems and other atmospheric processes, as often occurs in reality. Idealised modelling is not the only method that could have been used, and real cyclone events could have been investigated via case-studies (e.g. Ahmadi-Givi *et al.*, 2004) or compositing techniques (e.g. Field and Wood, 2007). However, results of case studies can be difficult to interpret as there can be significant case-to-case variability. Results can become contaminated due to the influence of neighbouring systems and it is difficult to establish whether the conclusions are generic and applicable to all systems, or are confined to the particular case. Compositing techniques use many different case-studies, averaging the results to obtain a composite, representative cyclone. The assumption is that the averaging process removes the case-to-case variability and any influence that neighbouring systems may have had on an individual case. However, the averaging process also “smoothes” out cyclone features, such as fronts and rainbands, since the composite will contain many cyclones of different shapes and sizes, at different stages of their life-cycle.

Chapter 2 documents the creation of a new numerical model of idealised cyclone development that will be used to generate the cases studied in this thesis. The idealised model will simulate a single cyclone-anticyclone system evolving in a typical mid-latitude background. This allows the isolation of cyclone processes and their interaction with atmospheric physics. The model used to simulate the cyclone will contain a full range of state-of-the-art physical parameterisations that will represent, to the best level currently possible, atmospheric moisture and boundary-layer processes. The simulation will be compared to conceptual models, as discussed in Section 1.3, demonstrating that the structure and evolution of cyclone fronts and airflows is representative of what is observed in reality.

Chapter 3 will address the first question posed above, expanding on the questions raised in Section 1.4. It remains to be established whether the baroclinic PV mechanism would work for a Type-B cyclogenesis event, and so this will be addressed initially, comparing idealised simulations

of Type-A and Type-B cyclogenesis. The role of surface sensible heat-fluxes in the spin-down process remains unclear, and so this will be addressed by using differing sea-surface temperature distributions to generate different heat-flux patterns. Finally, the question of whether the Ekman and baroclinic PV mechanisms really are distinct or whether there are any linkages between them will be addressed.

Chapter 4 will investigate the boundary-layer structure and evolution in moist life cycles, answering the second main question of this thesis. This will expand on the questions raised in Section 1.5, determining how the cyclone and boundary layer interact to redistribute and ventilate moisture from the boundary layer. This will provide quantification of the water cycle of a mid-latitude cyclone, demonstrating how the boundary layer provides the coupling between the surface and free troposphere. The source for WCB moisture and precipitation will be established, and the importance of the WCB will be compared to ventilation from shallow cumulus. A conceptual model of moisture transport within the cyclone boundary layer will be created, and it will be demonstrated that boundary layer and shallow convective processes are important components in the poleward transport of water vapour.

Chapter 5 will answer the third main question posed above, considering how robust the results presented in Chapter 4 are to changes in large-scale and boundary-layer parameters. Atmospheric temperature and humidity profiles, cyclone structure and intensity, and surface sensible and latent heat fluxes will all be considered, and their effects on moisture transport established. Scaling arguments will be presented, demonstrating how moisture transport is influenced by these changes. This quantification will provide guidance on how mid-latitude cyclones might react to a changing climate, helping to reduce some of the uncertainty in climate projections described in Section 1.1.

Finally, some general conclusions and recommendations for further research will be given in Chapter 6.

## CHAPTER 2:

# IDEALISED CYCLONE-WAVE LIFE CYCLES

### 2.1 INTRODUCTION

Idealised simulations of mid-latitude cyclone waves will be used throughout this thesis to investigate the interaction of near-surface physical processes with the large-scale dynamics. This chapter details the construction of a new tool to simulate idealised life cycles, utilising the Met Office Unified Model (MetUM, version 6.1, Cullen, 1993). The MetUM is currently used by the UK Meteorological Office for operational weather and climate prediction. It is one of the most advanced meteorological models currently available, both in terms of the numerics it uses and the physical parameterisation schemes it employs. It is also a commonly used model with good support facilities, which will allow others easy access to the tool created. The use of the MetUM is important, since the parameterisation schemes can provide a complete description of the physical processes occurring within the atmosphere and ocean. Not all physical parameterisation schemes will be used in this thesis, but the choice of the MetUM means that further studies using this model can increase the level of complexity to suit their needs. An overview of the MetUM will be given in Section 2.2, with a more detailed description of boundary-layer processes and their representation within the MetUM given in Section 2.3. Dry Type-A life cycles discussed and compared to previous studies in Section 2.4, with moist Type-A life cycles being discussed in Section 2.5. Finally, Type-B life cycles will be discussed in Section 2.6.

## 2.2 OVERVIEW OF THE METUM

### 2.2.1 LARGE-SCALE DYNAMICS

The MetUM numerically solves the full, deep-atmosphere, compressible Navier-Stokes equations (Staniforth *et al.*, 2005):

$$\frac{D\mathbf{u}}{Dt} = -2\boldsymbol{\Omega} \times \mathbf{u} - \frac{\nabla p}{\rho} + \mathbf{g} + \mathbf{S}^u, \quad (2.1a)$$

$$\frac{\partial \rho}{\partial t} + \nabla \cdot (\rho \mathbf{u}) = 0, \quad (2.1b)$$

where  $\mathbf{u}$  is the full velocity vector  $(u, v, w)$ ,  $\boldsymbol{\Omega}$  is the rotation rate of the Earth and  $p$  is the atmospheric pressure. These are solved together with the first law of thermodynamics

$$\frac{D\theta}{Dt} = S^\theta, \quad (2.2)$$

and equation of state

$$p = \rho RT, \quad (2.3)$$

to obtain the evolution of the dependent variables  $\mathbf{u}, \theta, p, \rho$ . Here,  $S^\theta$  represents any source or sink of heat,  $R$  is the ideal gas constant and  $T$  is the temperature. In practice,  $p$  is replaced by the Exner function

$$\Pi = \left( \frac{p}{p_0} \right)^{R/c_p} \quad (2.4)$$

within the model, where  $p_0 = 1000$  hPa is the reference pressure and  $c_p$  is the specific heat capacity of air at constant pressure. Further details can be found in Staniforth *et al.* (2005).

The equations are discretised onto an Arakawa ‘‘C-grid’’ (Arakawa and Lamb, 1977) in the horizontal with Charney-Phillips (Charney and Phillips, 1953) vertical spacing. The ‘‘C-grid’’ is used as it does not allow decoupling of solutions and allows better geostrophic adjustment, whilst the Charney-Phillips grid gives better thermal wind balance and has no computational mode. The horizontal grid keeps the variables  $\rho, \Pi, \theta$  and  $w$  on a centre point, whilst offsetting  $u$  and  $v$ . The vertical staggering also separates points, keeping  $u, v, \Pi$  and  $\rho$  on rho- (or full-) levels, with  $\theta$  and  $w$  on theta- (or half-) levels.

The time integration of Equations 2.1a-2.3 is achieved using a semi-implicit, semi-lagrangian timestep for stability and accuracy of solutions (Davies *et al.*, 2005). The semi-lagrangian advection integrates solutions along trajectories, allowing the material derivative on the left-hand side

of Equations 2.1a and 2.2 to be evaluated. The semi-implicit nature uses a predictor-corrector sequence to “guess” the quantity at the next timestep, and then iterate to find a better approximation. No additional numerical diffusion is required for the stability of solutions.

For the simulations performed in this thesis, the model is configured at a resolution similar to the current global operational forecast setup, with a horizontal resolution of  $0.4^\circ$  (approximately 44.5 km), 38 vertical levels between the surface and model top (which sits at  $\approx 40$  km) and a 10 minute timestep. The vertical levels have a quadratic spacing, giving more levels near the surface, with 10 levels below 2 km allowing adequate representation of the boundary-layer, discussed in Section 2.3. As formulated, the model would be capable of simulating the evolution of a dry ideal gas in the absence of any physical processes. However, the atmosphere contains water in all three phases, and its inclusion is discussed below. Physical processes such as heating ( $S^{\theta}$ ) and frictional forces ( $S^u$ ) also need to be represented, and shall be discussed in Sections 2.2.2 and 2.3.

Moisture is represented in terms of mixing ratios, but these are easily converted to specific humidities for each phase of water – vapour ( $q_v$ ), liquid ( $q_l$ ) and frozen ( $q_f$ ). The basic requirement of the model is a conservation equation of the form

$$\frac{Dq}{Dt} = S^q. \quad (2.5)$$

$S^q$  now represents another physical process requiring consideration, namely the creation and destruction of moisture, and its conversion between phases.

### **2.2.2 PHYSICAL PARAMETERISATIONS**

Processes such as cloud formation, surface interactions through boundary-layer turbulence and particle interaction with radiation all occur on a much smaller scale than the  $0.4^\circ$  resolution of the model. These processes can therefore not be resolved by the model’s dynamics and so their effects need to be parameterised.

Large-scale cloud is treated by the parameterisation scheme of Smith (1990), which assumes that within each model grid box there is some variability around  $\bar{q}$ , the grid box mean value of  $q$ . This variability is represented by a simple triangular function with a peak at  $\bar{q}$ . Clouds form when

the specific humidity at a location is greater than the saturation specific humidity ( $q_{\text{sat}}$ ). Therefore the cloud amount and cloud water content are determined from the fraction of the distribution where  $q > q_{\text{sat}}$ . The width of this triangular distribution is determined from a critical relative humidity parameter, which decreases from 91% near the surface to 80% above the boundary layer. Therefore, when the relative humidity in a grid box exceeds this critical value, some cloud will start to form.

Microphysical processes are treated by the scheme of Wilson and Ballard (1999), determining the transfer of water between its different phases. The scheme starts at the highest model level and calculates any transfer between water phases, based on physical process equations. This then gives information on the increments,  $S^q$ , for each water phase, and any latent heat released ( $S^{\theta}$ ). Any precipitating water or ice is released from this level to the next level down and the calculations are then repeated for that level. This continues until the surface is reached, at which point any precipitating water or ice is removed from the atmosphere, representing the surface precipitation rate.

Clouds and precipitation can also form due to the atmosphere being conditionally unstable to moist convection. Based on an adiabatic parcel ascent, the convection parameterisation works upwards in a single atmospheric column, testing each level until one is found with an excess in buoyancy. If, after taking entrainment and detraining of environmental air into account, the parcel remains buoyant at the level above, the convection process is said to have started and the parcel continues to rise, exchanging air with the surrounding atmosphere until it reaches its level of neutral buoyancy.

Convection is based on the scheme of Gregory and Rowntree (1990), using a mass-flux approach to represent an ensemble of convective clouds as a bulk entraining/detraining plume. Convection is diagnosed as “shallow” if the buoyancy of the parcel reaches a maximum below 2.5 km, or the level of neutral buoyancy is below the freezing level. The shallow convection is then parameterised using the scheme of Grant (2001), which relates the cloud-base mass-flux to the sub-cloud turbulent kinetic energy (TKE) budget. The cumulus convection is assumed to be associated with TKE transport into the cloud layer. Entrainment and detraining rates for shallow convection are parameterised as in Grant and Brown (1999), which relates the entrainment rate to the generation of TKE within the cloud ensemble. If the conditions of shallow convection are

not met, then deep convection is diagnosed. Deep convection is parameterised using a convective available potential energy (CAPE) closure scheme, as introduced by Fritsch and Chappell (1980). The scheme prescribes a time period over which the convection should remove all of the buoyant energy available to a parcel, and thus regulates the amount of convection occurring.

Radiation is parameterised using the Edwards and Slingo (1996) radiation code. This parameterises radiative transfer by calculating upward and downward vertical fluxes within a grid box. It uses a two stream approach with equations in the long-wave and short-wave, and includes the interaction of radiation with ice crystals and liquid water, as well as gaseous and continuum absorption.

## 2.3 THE ATMOSPHERIC BOUNDARY LAYER

The main focus of this project is the interaction of the atmospheric boundary layer with mid-latitude cyclones, and so a detailed overview of near-surface turbulence and its representation within the MetUM shall now be given.

### 2.3.1 REYNOLDS DECOMPOSITION

The boundary layer requires parameterisation because the scales of turbulence near the surface are much smaller than the grid resolution, and so processes this small cannot be represented. To represent them would require a grid resolution of  $\sim 1$  mm, since this is the scale of viscous dissipation. This is unfeasible given current computational resources, and so Reynolds averaging is used to write the prognostic variables  $\mathbf{u}$ ,  $\theta$  and  $q$  as a sum of their “mean” state and fluctuations from this, i.e.

$$\chi = \bar{\chi} + \chi' \quad , \quad \bar{\chi}' = 0, \quad (2.6)$$

for an arbitrary variable  $\chi$ . The mean could be any suitable temporal or spatial average, i.e. over a long enough length- or time-scale that the fluctuations ( $\chi'$ ) average to zero. In practice, the mean represents the model grid-box averaged state, with the grid-box assumed large enough that the fluctuations do average to zero. The model equations (2.1a, 2.1b, 2.2, 2.3 and 2.5) are then averaged in a similar manner. In terms that only contain one of these variables, the fluctuations

average to zero and the equation retains the same form, only with a quantity replaced by its grid-box mean. However, Equations 2.1a, 2.2 and 2.5 contain the advective term  $\nabla \cdot (\chi \mathbf{u})$ , in which the product of two fluctuations does not average to zero, i.e.

$$\nabla \cdot (\chi \mathbf{u}) = \nabla \cdot (\overline{\chi \mathbf{u}}) + \nabla \cdot (\overline{\chi' \mathbf{u}'}). \quad (2.7)$$

The covariance term,  $\nabla \cdot (\overline{\chi' \mathbf{u}'})$ , therefore appears as a turbulent flux, which is included within the source terms ( $S^X$ ). In practice, the vertical gradients of the covariance terms are much greater than the horizontal gradients, and therefore only the terms involving vertical gradients are retained within the model, giving

$$S^u = -\frac{\partial \overline{u'w'}}{\partial z} = \frac{1}{\rho} \frac{\partial \tau_x}{\partial z}, \quad S^v = -\frac{\partial \overline{v'w'}}{\partial z} = \frac{1}{\rho} \frac{\partial \tau_y}{\partial z}, \quad S^w = 0, \quad (2.8a)$$

$$S^\theta = -\frac{\partial \overline{\theta'w'}}{\partial z} = -\frac{1}{\rho c_p} \frac{\partial H}{\partial z}, \quad (2.8b)$$

$$S^q = -\frac{\partial \overline{q'w'}}{\partial z} = -\frac{1}{\rho} \frac{\partial E}{\partial z}, \quad (2.8c)$$

where  $\tau$  is the turbulent stress,  $H$  is the turbulent heat flux and  $E$  is the turbulent moisture flux. Calculation of the covariance terms requires knowledge of processes happening on a smaller scale than the grid-box, and the role of the boundary-layer scheme is to parameterise these fluxes in terms of quantities which are resolved ( $\overline{\chi}$ ). The boundary-layer scheme therefore calculates turbulent fluxes of momentum ( $\tau$ ), heat ( $H$ ) and moisture ( $E$ ) in terms of known quantities, based on semi-empirical relations derived from experimentation.

### 2.3.2 SURFACE FLUXES

Within the lowest few metres of the atmosphere, i.e. between the lowest model level and the surface, the windspeed must reduce to zero and the temperature and humidity must approach their surface values. Therefore, there are typically large exchanges of momentum and heat fluxes within this layer, which must be represented. For simplicity, simulations will only be considered here over a sea-surface. There is therefore no orography present since the sea-surface can be considered flat. However, as the wind blows over a sea-surface, waves develop and can appear as roughness elements to the boundary layer above. The effect of these waves on the atmosphere can be parameterised using the Charnock relation (Charnock, 1955), which relates the roughness

length to the friction velocity. Within the model, a generalised version (Smith, 1988) is used to include the behaviour of the roughness length in low-wind conditions:

$$z_{0m} = \frac{1.54 \times 10^{-6}}{u_*} + \alpha_c \frac{u_*^2}{g}, \quad (2.9)$$

with the Charnock parameter  $\alpha_c = 0.011$  and the friction velocity  $u_* \equiv |\tau_s/\rho|^{1/2}$ , where  $\tau_s$  is defined in Equation 2.10a. For each timestep within the model,  $u_*$  is not yet known when  $z_{0m}$  is calculated, and therefore it is taken from the previous timestep to avoid the need for iteration.

The lowest model level, being at 10 m for rho-levels and 20 m for theta-levels, is assumed to lie within the surface layer allowing bulk aerodynamic formula to be used for calculating the surface fluxes of momentum, heat and moisture:

$$\tau_s = \rho C_D |\mathbf{v}_1| \mathbf{v}_1, \quad (2.10a)$$

$$H_s = \rho c_p C_H |\mathbf{v}_1| (\theta_s - \theta_1), \quad (2.10b)$$

$$\lambda E_s = \rho \lambda C_H |\mathbf{v}_1| (q_{\text{sat}}(\theta_s) - q_1), \quad (2.10c)$$

where  $C_D$  is the drag coefficient,  $C_H$  is the Stanton number,  $\lambda$  is the latent heat of condensation of water,  $\mathbf{v}$  is the 2D velocity vector  $(u, v)$ , the subscript “s” denotes the surface value of a quantity and the subscript “1” denotes the value of a quantity at the first model level. Here, the sea-surface temperature ( $\theta_s$ ) is held constant throughout the simulations and the transfer coefficients ( $C_D$  and  $C_H$ ) are adjusted for the surface-layer stability according to Monin-Obukhov similarity theory (Monin and Obukhov, 1954).

Under neutral conditions, Prandtl’s mixing length hypothesis should hold true. Parcels of air mix with the environment over a lengthscale  $l_m$ , which near the surface is related only to the distance from the surface, i.e.  $l_m = \kappa z$  where  $\kappa = 0.4$  is the von Karman constant. This suggests that the near-surface wind shear should be inversely related to the distance from the surface, giving

$$\frac{\partial u}{\partial z} = \frac{u_*}{\kappa z}. \quad (2.11)$$

The integral of this gives the familiar log-wind profile, which by comparison to Equation 2.10a gives the neutral value of  $C_D$  as

$$C_D = \frac{\kappa^2}{\ln^2(z/z_{0m})}. \quad (2.12)$$

Monin and Obukhov (1954) proposed that under non-neutral conditions, the surface heat-flux ( $H_s$ ) and a buoyancy variable ( $g/\theta_1$ ) would be important as well as the distance from the surface and the friction velocity. The only non-dimensional combination of these four variables is  $z/L$ , where  $L$  is the Obukhov length, defined as

$$L = -\frac{u_*^3}{\kappa \frac{g}{\theta_1} \frac{H_s}{\rho c_p}}. \quad (2.13)$$

They further suggested that the non-dimensional wind shear should therefore be given by a universal function of  $z/L$ , i.e. Equation 2.11 should be modified thus

$$\frac{\kappa z}{u_*} \frac{\partial u}{\partial z} = \phi_m(z/L), \quad (2.14)$$

where  $\phi_m$  is the Monin-Obukhov stability function for momentum. By comparison with Equation 2.12, the stability-corrected value of  $C_D$  is given by

$$C_D = \frac{\kappa^2}{\Phi_m(z, z_{0m}, L)^2}, \quad (2.15)$$

where

$$\Phi_m(z, z_{0m}, L) = \int_{z_{0m}/L}^{z/L} \frac{\phi_m(z/L)}{z/L} d(z/L). \quad (2.16)$$

A similar argument can be followed to obtain the value of  $C_H$  as

$$C_H = \frac{\kappa^2}{\Phi_m(z, z_{0m}, L)\Phi_h(z, z_{0h}, L)}, \quad (2.17)$$

where  $\Phi_h(z, z_{0h}, L)$  is the integrated stability function for scalars and  $z_{0h} = 4 \times 10^{-5}$  m is the roughness length for scalars.

$\Phi_m$  and  $\Phi_h$  are determined empirically from comparison to observations, and so their functional form differs for stable and unstable boundary layers. The form used in the model is taken from Beljaars and Holtslag (1991), which for stable layers ( $L > 0$ ) is given by

$$\begin{aligned} \Phi_m = \ln(z/z_{0m}) + \frac{z - z_{0m}}{L} + \frac{2}{3} \left( \frac{z}{L} - \frac{5}{0.35} \right) \exp(-0.35z/L) \\ - \frac{2}{3} \left( \frac{z_{0m}}{L} - \frac{5}{0.35} \right) \exp(-0.35z_{0m}/L), \end{aligned} \quad (2.18a)$$

$$\begin{aligned} \Phi_h = \ln(z/z_{0h}) + \left( 1 + \frac{2z}{3L} \right)^{3/2} + \frac{2}{3} \left( \frac{z}{L} - \frac{5}{0.35} \right) \exp(-0.35z/L) \\ - \left( 1 + \frac{2z_{0h}}{3L} \right)^{3/2} - \frac{2}{3} \left( \frac{z_{0h}}{L} - \frac{5}{0.35} \right) \exp(-0.35z_{0h}/L), \end{aligned} \quad (2.18b)$$

whilst for unstable layers ( $L < 0$ ) they are given by

$$\Phi_m = \ln(z/z_{0m}) - 2 \ln \left( \frac{1+X_1}{1+X_0} \right) - \ln \left( \frac{1+X_1^2}{1+X_0^2} \right) + 2(\arctan X_1 - \arctan X_0), \quad (2.19a)$$

$$\Phi_h = \ln(z/z_{0h}) - 2 \ln \left( \frac{1+Y_1}{1+Y_0} \right), \quad (2.19b)$$

where

$$X_1 = (1 - 16z/L)^{1/4}, \quad X_0 = (1 - 16z_{0m}/L)^{1/4}, \quad (2.20a)$$

$$Y_1 = (1 - 16z/L)^{1/2}, \quad Y_0 = (1 - 16z_{0h}/L)^{1/2}. \quad (2.20b)$$

It is worth noting that as  $H_s \rightarrow 0$  and a neutral boundary layer is approached,  $L \rightarrow \pm\infty$  and  $\Phi_{m,h}$  approach their neutral values.

The MetUM contains the following improvements on the standard Monin-Obukhov theory presented above, detailed in Lock (2007). The friction velocity is replaced wherever it appears with a scaling velocity,  $v_*$ , defined as

$$v_*^2 = u_*^2 + \gamma_t^2 w_*^2, \quad w_* = \left( z_h \frac{F_B}{\rho} \right)^{1/3}. \quad (2.21)$$

This allows for the effect of turbulent scale gusts on the surface fluxes. Here  $\gamma_t$  is a dimensionless empirical parameter,  $z_h$  is the depth of the boundary-layer scheme operation and  $F_B$  is the surface buoyancy flux, defined as

$$F_B = \frac{g}{\theta_1} \frac{H_s}{c_p} + \frac{0.61g}{1+0.61q} E_s, \quad (2.22)$$

which includes the effects of the surface latent heat-flux on buoyancy. This then leads to the re-definition of the Obukhov length as

$$L = -\frac{v_*^3}{\kappa F_B/\rho}. \quad (2.23)$$

This procedure was started in an effort to calculate the surface fluxes ( $\tau_s, H_s, \lambda E_s$ ), but the solution requires knowledge of  $L$ , which is itself a function of  $\tau_s, H_s$  and  $\lambda E_s$ . Therefore the MetUM uses an iterative procedure to obtain the final values of surface fluxes, starting with a ‘‘guess’’ for  $L$ , calculating the surface fluxes and obtaining a better value of  $L$ . It is found that repeating the procedure five times is sufficient to obtain convergence and the final values of the Obukhov length and surface fluxes.

### 2.3.3 FLUXES IN THE BOUNDARY LAYER INTERIOR

Above the lowest model level, the boundary layer is divided into six categories depending on the stability and capping cloud, as shown in Figure 2.1 (Lock *et al.*, 2000). The first step is the

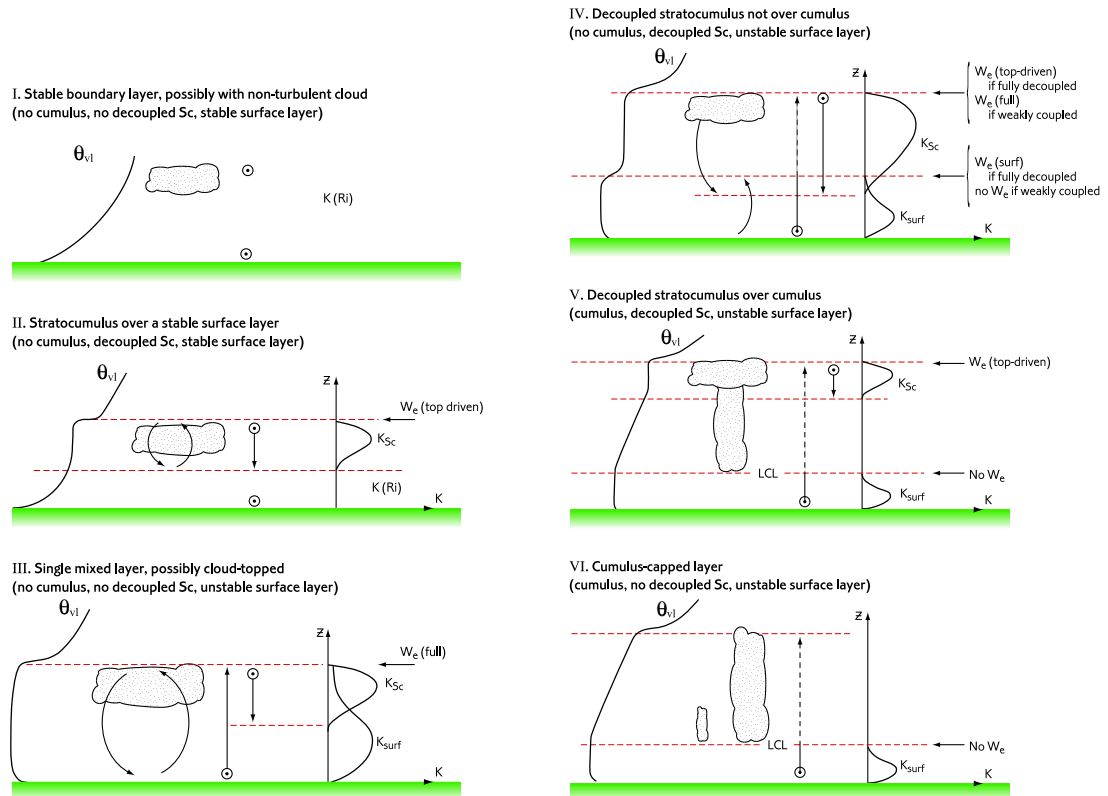


**Figure 2.1** Schematic representing boundary-layer types I to VI, from Lock *et al.* (2000). Arrow tops denote the extent of the surface parcel ascent ( $z_{par}$ ), whilst their solid line portion indicates the diagnosed boundary-layer top ( $z_h$ ). Downward arrows indicate the extent of cloud-top driven turbulence ( $z_{ml}$ ).  $w_e$  shows where the explicit entrainment parameterisation is applied and  $K(Ri)$ ,  $K^{surf}$  and  $K^{sc}$  show where each eddy diffusivity parameterisation is used. See text for further details.

separation of stable and unstable layers, based on the surface buoyancy flux ( $F_B$ ). Where unstable layers are found ( $F_B > 0$ ), a moist parcel ascent is used to calculate the level of neutral buoyancy for surface based thermals ( $z_{par}$ ). If the layer is well-mixed (i.e. clear or stratocumulus capped), the boundary-layer top is defined as  $z_h = z_{par}$ . However, if cumulus convection is present, the boundary-layer scheme is capped at the cumulus cloud base ( $z_h = \text{lifting condensation level}$ ). In

stable layers ( $F_B < 0$ ),  $z_h$  is defined where the Richardson number (Eqn 2.27) exceeds one.

In stable layers (types I and II) a first-order closure is used, parameterising the turbulent fluxes in terms of local gradients and eddy diffusivities:

$$\overline{\chi'w'} = -K_\chi \frac{\partial \chi}{\partial z}, \quad (2.24)$$

where the eddy diffusivities for momentum ( $K_m$ ) and scalars ( $K_h$ ) are given in terms of mixing lengths:

$$K_m = \mathcal{L}_m^2 \left| \frac{\partial \mathbf{v}}{\partial z} \right| f_m(Ri) \quad , \quad K_h = \mathcal{L}_m \mathcal{L}_h \left| \frac{\partial \mathbf{v}}{\partial z} \right| f_h(Ri), \quad (2.25)$$

where  $\mathcal{L}_{m,h}$  are the neutral mixing lengths, given over a sea-surface by

$$\mathcal{L}_{m,h} = \frac{\kappa z}{1 + \kappa z / \max[40, 0.15z_h]}, \quad (2.26)$$

and  $f_{m,h}(Ri)$  are the stability functions, dependent on the local Richardson number. In stable conditions ( $Ri > 0$ ), the ‘long-tailed’ functions are used:

$$f_{m,h} = \frac{1}{1 + 10Ri} \quad , \quad Ri = \frac{\frac{g}{\theta_v} \frac{\partial \theta_v}{\partial z}}{\left| \frac{\partial \mathbf{v}}{\partial z} \right|^2}, \quad (2.27)$$

where  $\theta_v = \theta(1 + 0.61q)$  is the virtual potential temperature.

Where unstable layers (types III – VI) are found, this procedure does not always produce enough mixing, although it is retained as the “minimum possible mixing” in unstable conditions. In reality, surface based thermals which are positively buoyant rise throughout the depth of the boundary layer, and so the turbulent fluxes are dependent more on the surface characteristics and depth of these large eddies, than the local Richardson number. Therefore, the eddy diffusivities are calculated thus:

$$K_m^{\text{surf}} = \kappa (u_*^3 + w_s^3)^{1/3} z \left( 1 - \mathcal{E} \frac{z}{z_h} \right)^2 \quad , \quad K_h^{\text{surf}} = K_m^{\text{surf}} / Pr, \quad (2.28)$$

where the superscript “surf” indicates that these eddy diffusivities are parameterising surface based turbulent mixing.  $\mathcal{E}$  is a factor to ensure that the diffusivities tend to the entrainment eddy diffusivities (Eqn. 2.34) as  $z$  tends to  $z_h$ , and  $Pr$  is the Prandtl number, defined in Lock (2007).  $w_s$  is a vertical velocity scaling, defined as

$$w_s^3 = \begin{cases} 2.5 \frac{z}{z_h} w_*^3 & \text{surface layer} \\ 0.25 w_*^3 & \text{mixed layer} \end{cases} \quad , \quad (2.29)$$

where the surface layer is defined as  $z < 0.1z_h$ . The diffusivities ( $K_\chi$ ) in Equation 2.24 are given by  $\max[K_\chi^{\text{surf}}, K_\chi(Ri)]$ , where  $K_\chi(Ri)$  is defined as in Equation 2.25, but with the stability functions for  $Ri < 0$  given by

$$f_{m,h} = 1 - \frac{10Ri}{1 + \mathcal{D}_{m,h}(\mathcal{L}_m/\mathcal{L}_h)|Ri|^{1/2}}, \quad (2.30)$$

where  $\mathcal{D}_m = 2.5$  and  $\mathcal{D}_h = 0.4$ .

For the turbulent heat-flux only, there is an additional term added to Equation 2.24, referred to as the counter-gradient term and described in Holtslag and Boville (1993). This is added because often in convective boundary layers,  $\frac{\partial\theta}{\partial z} \approx 0$ , which would result in the turbulent heat-flux, defined in Equation 2.24, being unrealistically small. Therefore, the following form for the turbulent heat-flux, derived in Holtslag and Moeng (1991), is used

$$\overline{w'\theta'} = -K_h \frac{\partial\theta}{\partial z} + K_h^{\text{surf}} \gamma_h, \quad (2.31a)$$

$$\gamma_h = \min \left[ 3.26 \frac{1.93 \overline{w'\theta'_s}}{z_h (u_*^3 + w_s^3)^{1/3}}, 10^{-3} \right]. \quad (2.31b)$$

Further sub-classifications of the boundary-layer depend on the type of capping cloud that is diagnosed. If cumulus convection is diagnosed (types V and VI), then the boundary-layer scheme is capped at the cumulus cloud base and the cumulus convection is treated entirely by the convection scheme outlined in Section 2.2.2. Stratocumulus capped boundary layers have turbulence driven from the cloud top downwards in a similar manner to surface driven turbulence in unstable boundary layers. Therefore this turbulence is parameterised in much the same way, with the eddy diffusivities defined as

$$K_m^{\text{sc}} = 0.63\kappa V_{\text{sc}} \frac{z'^2}{z_{\text{ml}}} \left( 1 - \mathcal{E} \frac{z'}{z_{\text{ml}}} \right)^{0.8}, \quad K_h^{\text{sc}} = K_m^{\text{sc}}/Pr, \quad (2.32)$$

where the superscript ‘‘sc’’ indicates that these eddy diffusivities are parameterising turbulent mixing driven from the stratocumulus cloud top.  $z'$  is the height above cloud base,  $z_{\text{ml}}$  is the cloud depth and  $V_{\text{sc}}$  is a scaling velocity. In unstable boundary layers,  $K_\chi^{\text{sc}}$  is added to  $K_\chi^{\text{surf}}$  in cloudy regions where  $K_\chi^{\text{surf}}$  is nonzero (type III). Alternatively, if  $K_\chi^{\text{surf}}$  does not extend to the cloud top, then the scheme can model decoupled cloud, creating mixing in regions of nonzero  $K_\chi^{\text{sc}}$  even if there is no surface influence here (type IV and V). Finally, applying  $K_\chi^{\text{sc}}$  over a stable surface layer allows the option of simulating decoupled stratocumulus over a stable surface layer (type II), continuing mixing even where  $K_\chi(Ri) = 0$ .

Finally, the scheme contains an explicit entrainment parameterisation in terms of an entrainment velocity ( $w_e$ ), described in Lock (2001). The boundary-layer top ( $z_h$ ) has been defined as the level of neutral buoyancy for an ascending air parcel, however as the parcel carries momentum towards  $z_h$ , it will not stop exactly at  $z_h$  and will tend to overshoot into the free troposphere. As this overshooting air sinks back into the mixed layer, it will carry some warmer air from the troposphere with it, which appears as a heat-flux at the boundary-layer top. The descending air can also carry moisture and momentum from the troposphere into the boundary layer. For scalar variables, the entrainment fluxes are specified explicitly. It is assumed that the entrainment fluxes reduce from their maximum at  $z = z_h$  to zero at  $z = h$ , a small distance above. The fluxes are then proportional to the change in a quantity between  $z_h$  and  $h$ :

$$H|_{z_h} = -w_e \Delta\theta + F_{\text{net}} \quad , \quad \overline{w'q'}|_{z_h} = -w_e \Delta q, \quad (2.33)$$

where  $F_{\text{net}}$  is the net radiation at  $z_h$ . Entrainment fluxes for momentum are specified through eddy-diffusivities:

$$K_h|_{z_h} = w_e \Delta z \quad , \quad K_m|_{z_h} = Pr K_h|_{z_h}, \quad (2.34)$$

where  $\Delta z$  is the distance between the two model theta-levels either side of  $z_h$ .

### 2.3.4 DEFINITION OF THE BOUNDARY-LAYER TOP

As discussed in Section 2.3.3, the MetUM calculates the boundary-layer top differently depending on which of the six types of boundary layer is diagnosed. This can lead to sharp discontinuities in the value of  $z_h$  between neighbouring grid-boxes which are diagnosed as being different boundary-layer types. Therefore, for the remainder of this thesis, the boundary-layer depth ( $h$ ) shall be defined following the method of Troen and Mahrt (1986). This is essentially the basis of the MetUM diagnosis of  $z_{\text{par}}$ , using a parcel ascent to calculate the level of neutral buoyancy for surface-based thermals. Sinclair *et al.* (2010b) have discussed the calculation of  $h$  via this method in dry cyclone simulations, and their method is extended here to include moist variables. Initially, the bulk Richardson number is calculated at each model level:

$$Rib = \frac{\frac{g}{\theta_{v0}} (\theta_v - \theta_{v0}) z}{u^2 + v^2}, \quad (2.35)$$

where  $\theta_{v0}$  is an estimate of the near-surface air temperature, given in unstable boundary layers by

$$\theta_{v0} = \theta_{v1} + 8.5 \frac{\overline{w'\theta'_{vs}}}{v_*/\phi_m}, \quad (2.36)$$

and in stable boundary layers by  $\theta_{v0} = \theta_{v1}$ .  $\phi_m$  is the dimensionless vertical wind shear in the surface layer, given by

$$\phi_m = \left(1 - 15\frac{z}{L}\right)^{-0.25}. \quad (2.37)$$

The boundary-layer top is then defined as the height at which  $Ri_b = 0.25$ , which is determined by a linear interpolation between model levels.

In most boundary-layer types  $h \approx z_h$ , with the largest differences occurring in cumulus capped boundary layers. This method finds  $h$  somewhere within the cloud layer, more accurately representing the depth of surface-based mixing than  $z_h$  and resulting in a smooth transition at the edge of cumulus regions. Within the MetUM, the mixing is continuous above  $z_h$ , but is done by the convection scheme. This method provides a boundary-layer top which is spatially smooth, ensuring that the spatial derivatives required for the budget calculations presented in Section 4.4 can be evaluated. The definition will also provide consistency with results presented by Sinclair *et al.* (2010b), allowing quantitative comparisons to be made with their mass budget results in dry cyclone simulations.

## 2.4 DRY TYPE-A LIFE CYCLES

Many previous studies have focussed on dry, Type-A life cycles, the most popular of which is denoted LC1 by Thorncroft *et al.* (1993). This idealised life-cycle captures the main features of extratropical cyclogenesis, and the effect of the boundary layer has been discussed previously by Adamson *et al.* (2006) and Sinclair *et al.* (2010b). Therefore this section will discuss the creation of a Type-A life-cycle, similar to LC1, in the MetUM. The resulting simulations will be compared and contrasted to previous studies, in order to demonstrate the representativeness of these simulations to previous literature and real weather systems.

### 2.4.1 INITIALISATION

To simulate idealised cyclones in the MetUM requires a basic state to represent the climatology of the Northern Hemisphere wintertime storm track. To achieve this, a zonally-independent wind-

profile is defined in the same manner as Polvani and Esler (2007):

$$u(\phi, z) = U_0 \sin^3(\pi \sin^2(\phi)) \frac{z}{z_T} \exp\left(-\frac{(z/z_T)^2 - 1}{2}\right), \quad (2.38)$$

where  $\phi$  is the latitude,  $U_0 = 45 \text{ ms}^{-1}$  is the maximum jet speed and  $z_T = 13 \text{ km}$  is the temperature scale height. This gives a basic state westerly jet, with windspeed increasing from zero at the surface to a maximum at the tropopause. The functional form of Equation 2.38 gives a decrease in the jet speed within the stratosphere and the latitudinal dependence confines the peak jet speed to 45N, decreasing towards the equator and pole. The profile is also designed to closely match the jet structure used by Thorncroft *et al.* (1993) to simulate LC1 cyclones in the Reading IGC.

A temperature profile is then calculated in thermal-wind balance with the jet, and a pressure profile in hydrostatic balance with this. The model is run for several timesteps (six was found to be sufficient) to allow the initial profiles to adjust to a non-hydrostatic balance consistent with the equation set of the MetUM. The sea-surface temperature (SST) is fixed equal to the initial temperature of the lowest model theta-level (at 20 m), so that there are no surface fluxes in the basic state. The SST is kept constant throughout the simulation, consistent with the operational MetUM which uses fixed SSTs for forecasts up to two weeks. The initial zonal winds and temperature are shown in Figure 2.2, along with the initial state used by Thorncroft *et al.* (1993) for comparison.

The zonal flow described is well balanced and tests confirm that the model can be run for many days with the jet maintaining its structure. In order to trigger cyclogenesis, some perturbation is required, and again the method of Polvani and Esler (2007) is followed here, perturbing the temperature field at all heights by a small amount, given by

$$T'(\Lambda, \phi) = \hat{T} \cos(m\Lambda) \text{sech}^2(m(\phi - \hat{\phi})), \quad (2.39)$$

where  $\Lambda$  is the longitude,  $\hat{T} = 1 \text{ K}$  is the maximum perturbation,  $m$  is the zonal wavenumber and  $\hat{\phi} = 45\text{N}$  is the latitude of the jet centre. In order to generate cyclones comparable to Thorncroft *et al.* (1993), wavenumber-6 cyclogenesis is simulated by setting  $m = 6$ . The MetUM is then configured on a limited-area domain with  $60^\circ$  of longitude and east-west cyclic boundary conditions. This forces the domain to contain a single cyclone-anticyclone system, with any upstream or downstream development occurring on top of the original system. The north and south boundary conditions are given by the initial conditions, giving a channel-flow, and are located a large distance from the jet so as to not affect the results.

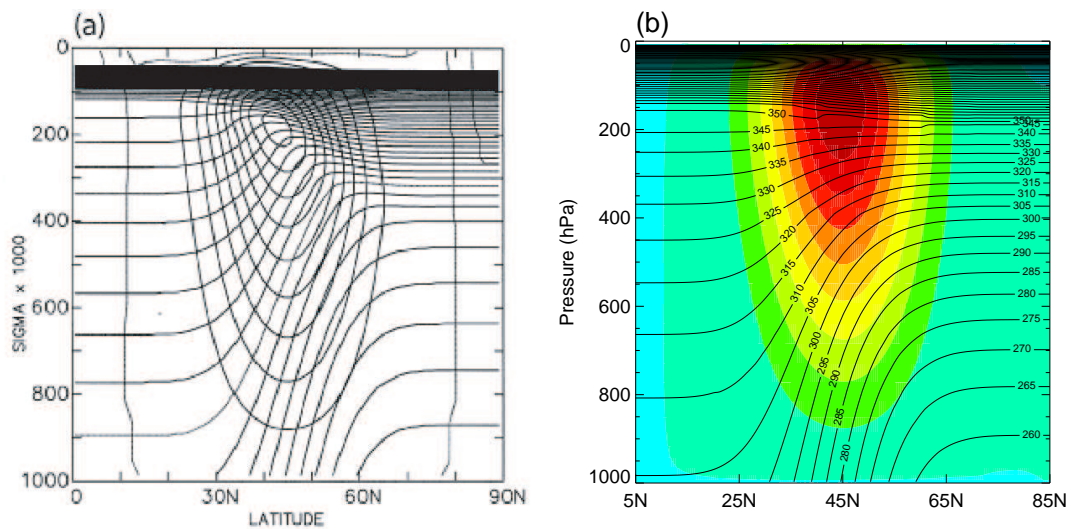


**Figure 2.2** Initial zonal winds (black contours in (a), colour shading in (b), interval  $5 \text{ ms}^{-1}$ ) and potential temperature (black contours, interval 5 K) from (a) Thorncroft *et al.* (1993, Fig. 3a) and (b) this study.

#### 2.4.2 DYNAMICS ONLY LIFE CYCLES

In order to compare this new simulation to the life cycles of Thorncroft *et al.* (1993), it is necessary to conduct a series of experiments with only the model dynamics operating, since this is how the IGCN was configured for their original experiments. In these simulations, there is no boundary layer and the surface has a “free-slip” boundary condition. However, technical difficulties with the spherical domain setup in the MetUM prevented the running of simulations identical to those of Thorncroft *et al.* (1993) until the project was nearing completion. Instead, cyclogenesis was simulated in a domain with Cartesian geometry and an  $f$ -plane ( $f = 2\Omega \sin \hat{\phi}$ ), making the resulting simulations appear very similar to the no-shear case discussed by Wernli *et al.* (1998).

The differences between cyclone life cycles in Cartesian and spherical geometry have been investigated by Balasubramanian and Garner (1997), who compared the same LC1 cyclone simulation in two models – one with Cartesian geometry and one with spherical geometry. They discovered that in Cartesian geometry, there was less poleward movement of low-pressure systems than there was in the spherical equivalent. The poleward motion in spherical geometry caused the flow to return towards its zonal-mean state quicker, meaning the peak eddy kinetic energy

(EKE, Eqn. 2.40) was achieved two days earlier for the spherical case than the Cartesian case. Furthermore, the Cartesian geometry creates a tendency for the waves to break more cyclonically than the typical anticyclonic wavebreaking associated with the LC1 life-cycle. This means that in Cartesian geometry, the cyclones appear more wrapped-up and sit somewhere between LC1 and LC2 in the spectrum of possible cases.

These differences were also found here in the MetUM simulations. Figure 2.3 shows the evolution of minimum mean sea-level pressure (MSLP) and EKE over the life cycles on the Cartesian and spherical domains. The EKE is defined as

$$\frac{1}{2gA} \int_0^{p_0} \int_S (u - \langle u \rangle)^2 + (v - \langle v \rangle)^2 dS dp, \quad (2.40)$$

where  $\langle \rangle$  denote the zonal mean of a quantity and  $S$  is a pressure surface of area  $A$ . It is notice-

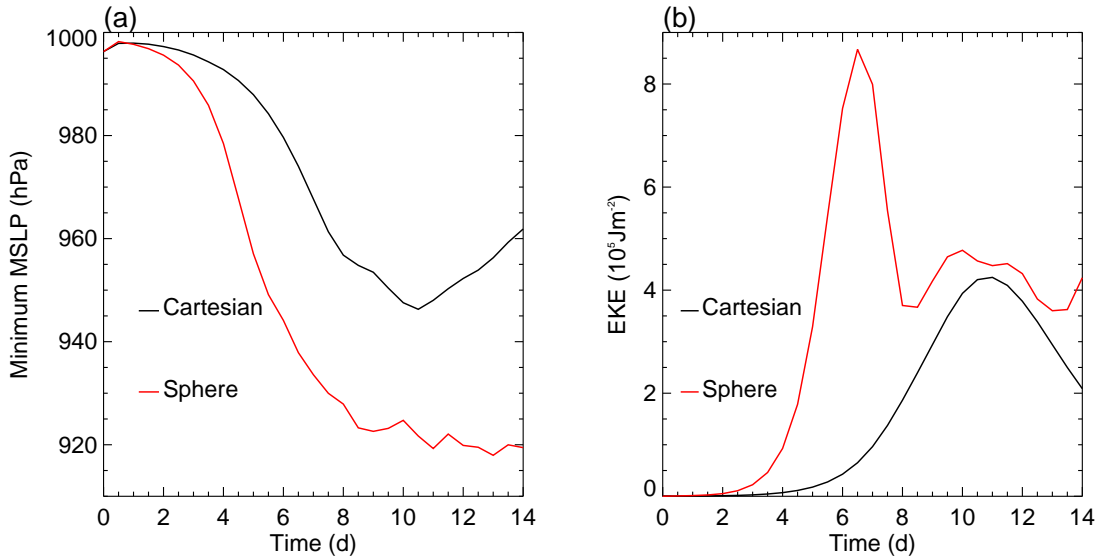


**Figure 2.3** Time series of (a) minimum sea-level pressure and (b) eddy kinetic energy, for the dynamics-only life-cycle on the Cartesian and spherical domains.

able that the peak EKE is at day 10.5 for the Cartesian life-cycle, compared with day 6.5 for the spherical case, a lag of 4 days. The additional two day lag over the results of Balasubramanian and Garner (1997) occurs because of the perturbation method and model differences, and could be removed by adjusting the scaling factor  $\hat{T}$  in Equation 2.39. The amplitude of  $\hat{T}$  was “tuned” by Polvani and Esler (2007) to match their results to the spherical solutions of Thorncroft *et al.* (1993), and the same factor has been applied in these Cartesian simulations. Tests have shown

that doubling  $\hat{T}$  causes cyclogenesis to trigger earlier and the peak EKE is then found at day 8, although the evolution of the wave is identical in all respects apart from timing. There was no reason to tune this parameter so that the Cartesian life-cycle matched the timing of the Balasubramanian and Garner (1997) study, instead the same perturbation for spherical and Cartesian simulations was used.

In general, the system in the spherical domain is stronger, with lower minimum MSLP and higher EKE. The timing of MSLP and EKE evolution is very similar in the Cartesian case, with both measures of cyclone intensity reaching their peak at day 10.5 before decaying. In the spherical case, the flow zonalises around day 8, causing a large drop in the EKE, which then remains almost constant for the rest of the simulation. However, the minimum MSLP is not reached until day 11. Figure 2.4 shows how this is related to the different geometrical setups. The low-pressure

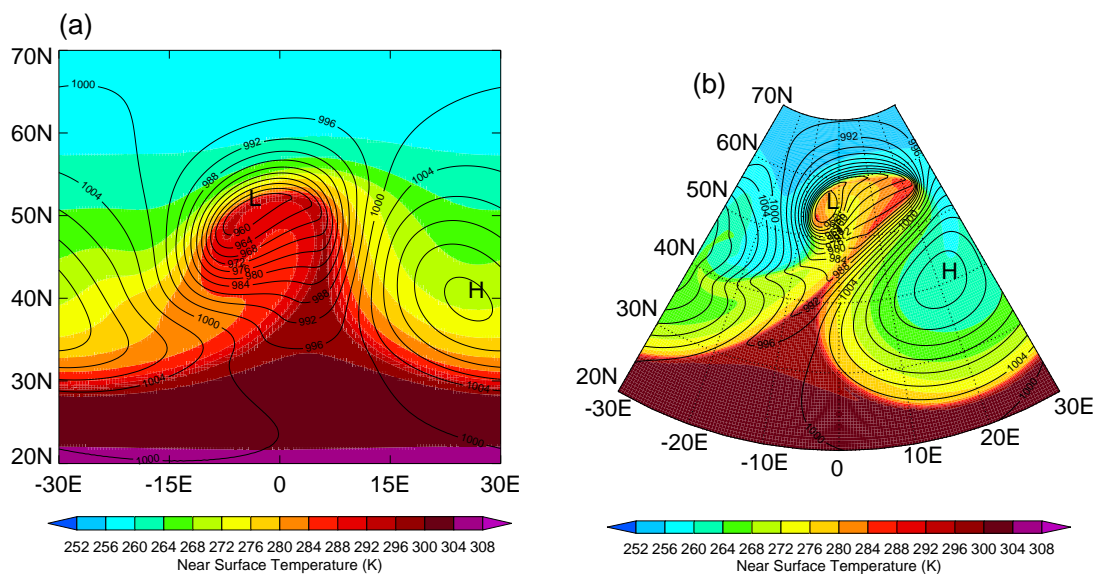


**Figure 2.4** Mean sea-level pressure (black contours, interval 4 hPa) and 20 m temperature (colour contours) for (a) the Cartesian domain at day 8, and (b) the spherical domain at day 6.

centres move further polewards in the spherical domain (Fig. 2.4(b)), leaving the high-pressure system in the south of the domain. Once this has happened, the departure of the winds from their zonal-mean state becomes smaller, giving lower values of EKE even though the MSLP continues to fall. By comparison, in the Cartesian case (Fig. 2.4(a)), the low and high pressure systems remain aligned along the centre of the domain, meaning the departure of the winds from their zonal

mean is high, maintaining high values of EKE up to day 11, when the cyclone starts to decay.

It is noticeable from Figure 2.4 that the Cartesian system appears more “wrapped-up” than the spherical system, again consistent with Balasubramanian and Garner (1997). Both simulations display many features of a typical mid-latitude weather system however. LC1 is thought of as cold-front dominated, and this is clear from Figure 2.4(b), with a very strong trailing cold front apparent between (20E, 55N) and (−15E, 35N). A strong cold front is also apparent in the Cartesian simulation (Fig. 2.4(a)), extending from (5E, 50N) to (−15E, 30N). There is also a hint of a warm-front present in the Cartesian case, with the structure appearing similar to the conceptual model of Shapiro and Keyser (1990). This similarity was also noted by Wernli *et al.* (1998), providing evidence that the Cartesian simulation is a realistic and well understood system. The remainder of this thesis will focus on the Cartesian simulation as the control run, denoted  $AD_0$ . This notation will be used to define the simulations, combining information of the cyclone type (A or B), presence of moisture (D or M) and boundary-layer scheme options. Full details are given in Table 2.1 on Page 53.

### **2.4.3 DRY LIFE-CYCLE WITH BOUNDARY LAYER**

The effect of a parameterised boundary layer (similar to that discussed in Section 2.3) on LC1 life cycles has been discussed by Adamson *et al.* (2006) and Plant and Belcher (2007). Their results suggested that there should be a delay in the peak EKE of  $\approx 1$  day and a reduction in the peak by  $\approx 35\%$ . Figure 2.5 shows the EKE and minimum MSLP for the Cartesian life-cycle with the boundary-layer scheme operating, denoted  $AD_{BL}$ . In these dry life cycles, the boundary-layer scheme only allows surface momentum and heat exchange and near surface mixing. The addition of surface drag acts to delay the peak EKE by a about a day, and reduces the peak by 37%, consistent with Adamson *et al.* (2006).

Figure 2.6 shows the MSLP and potential temperature at 1.5 km, just above the diagnosed boundary-layer top, at day 9 of simulation  $AD_{BL}$ . The addition of surface momentum and heat exchange and near-surface mixing leads to weaker frontal features near the surface. Sharp temperature gradients can be “mixed” away within the lowest  $\sim 1$  km of the atmosphere, but fronts are still apparent in the potential temperature field above this (Fig. 2.6). The temperature field at

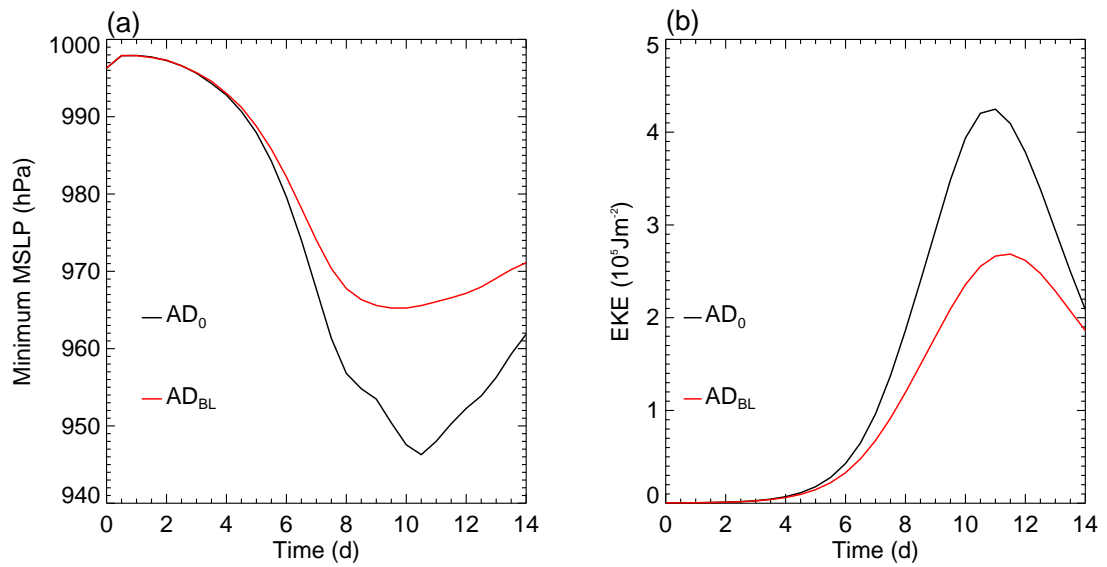


**Figure 2.5** Time series of (a) minimum sea-level pressure and (b) eddy kinetic energy, for the Cartesian life-cycle with and without the boundary-layer scheme operating.

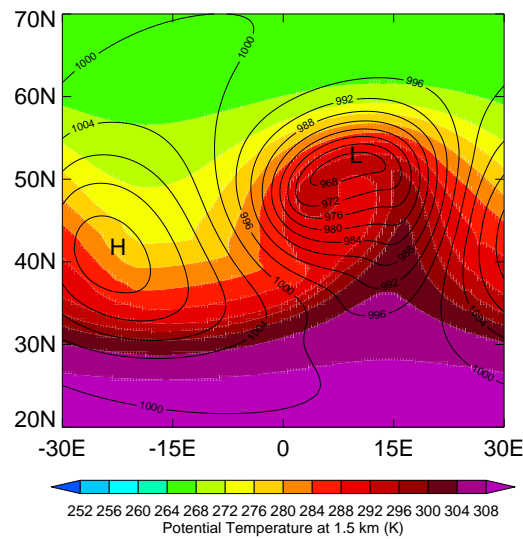


**Figure 2.6** Mean sea-level pressure (black contours, interval 4 hPa) and potential temperature at 1.5 km (colour contours), for the Cartesian simulation with boundary layer at day 9.

this height shows much similarity to the dynamics only simulation (Fig. 2.4(a)), still dominated by a strong cold front.

## 2.5 MOIST TYPE-A LIFE CYCLES

Due to the need for accurate parameterisations of convection, cloud microphysics and precipitation, idealised numerical simulations of moist cyclone-wave life cycles are relatively few in number. Gutowski *et al.* (1992) and Pavan *et al.* (1999) describe large-scale features, energetics and moisture transport in cyclone waves with relatively simple moisture parameterisations. Their parameterisation schemes contained a moisture variable, transported according to Equation 2.5, however the parameterisation of  $S^q$  simply removed any supersaturation (as surface precipitation without re-evaporation back to the atmosphere), converting the latent heat released into  $S^\theta$ . Therefore, the MetUM parameterisation schemes, described in Section 2.2.2, provide a more realistic description of the cloud microphysics and mixed-phase precipitation processes occurring within the cyclone. Their results demonstrate how cyclone waves are important in redistributing moisture within the free troposphere, but they could not quantitatively evaluate moisture transport due to their simple representation of the conversion of moisture between phases. They also could not fully investigate the role of the boundary layer in this process, since their simulations only included a single-layer parameterisation of surface drag and heat/moisture exchange. The detailed parameterisation schemes of the MetUM will enable the investigation of the coupling between the atmospheric moisture, large-scale dynamics and the boundary layer. This section discusses the creation of an idealised moisture initialisation and the resulting simulation, comparing it to conceptual models of cyclone evolution.

### 2.5.1 INITIALISATION AND LIFE CYCLES WITHOUT A BOUNDARY LAYER

Section 2.4.1 discussed the initialisation of dry idealised cyclones, using an analytically defined initial condition profile. It is necessary to also define a consistent initial moisture profile. Here, an analytical form is proposed that will allow control over the large-scale moisture distribution, enabling the moisture content or distribution to be quickly and easily modified. The profile needs

to be representative of the climatological mean wintertime storm track. It is defined in terms of relative humidity (RH) so that the actual moisture content will depend on the temperature profile. The first constraint is that RH must decrease as  $z$  increases, so the  $z$  dependence of RH is defined by

$$RH(y, z) = \begin{cases} RH_0(1 - 0.9R(y)(z/z_q)^{5/4}) & z < z_q \\ RH_0(0.0625) & z > z_q \end{cases}, \quad (2.41)$$

where  $z_q = 12$  km is a moisture scale-height,  $R(y)$  is defined in Equation 2.42 and  $RH_0$  is the maximum value of RH, chosen here to be 80%. Equation 2.41 gives a typical tropospheric moisture profile up to  $z_q$ , using the spacing of the MetUM's vertical levels to give a sharp gradient above this, in the region of the tropopause ( $z_T$ ). The  $z^{5/4}$  dependence is taken from Takemi (2006), who uses this analytic dependence as representative of the mid-latitude troposphere to investigate convection and squall lines. The second constraint is that most moisture is contained near the equator, decreasing across the jet region. For simplicity, a linear decrease of moisture in the  $y$  direction is defined as follows:

$$R(y) = \begin{cases} 1 & y < 25\text{N} \\ 0.5 & y > 65\text{N} \\ 1 - 0.5 \left( \frac{y-25}{40} \right) & 25\text{N} < y < 65\text{N} \end{cases}. \quad (2.42)$$

There is no zonal dependence for consistency with the temperature structure. The profile is shown in Figure 2.7, along with the Northern Hemisphere climatology from the National Centre for Environmental Prediction (NCEP) reanalysis dataset, taken from Pavan *et al.* (1999). Whilst not identical, the two profiles are qualitatively similar. The RH decreases from around 80% near the surface to around 45% at 300 hPa, an effect that is modelled by Equation 2.41. At any pressure level, there is an increase in RH moving from the equator to the pole across the mid-latitude jet region, and this effect is modelled by Equation 2.42. The very low values of RH shown around (20N, 500 hPa) in Figure 2.7(a) are due to deep convection in the tropics, something the analytical profile should not replicate as no cloud fields are specified in the initial condition. This feature will spin-up in time as the simulation evolves, although it is not particularly relevant to the study of mid-latitude cyclogenesis.

When combined with the temperature profile, this produces the specific humidity profile shown in Figure 2.8(b). The profile is chosen so that the specific humidity matches closely the profile used by Gutowski *et al.* (1992) (Figure 2.8(a)), who approximate the climatological Northern

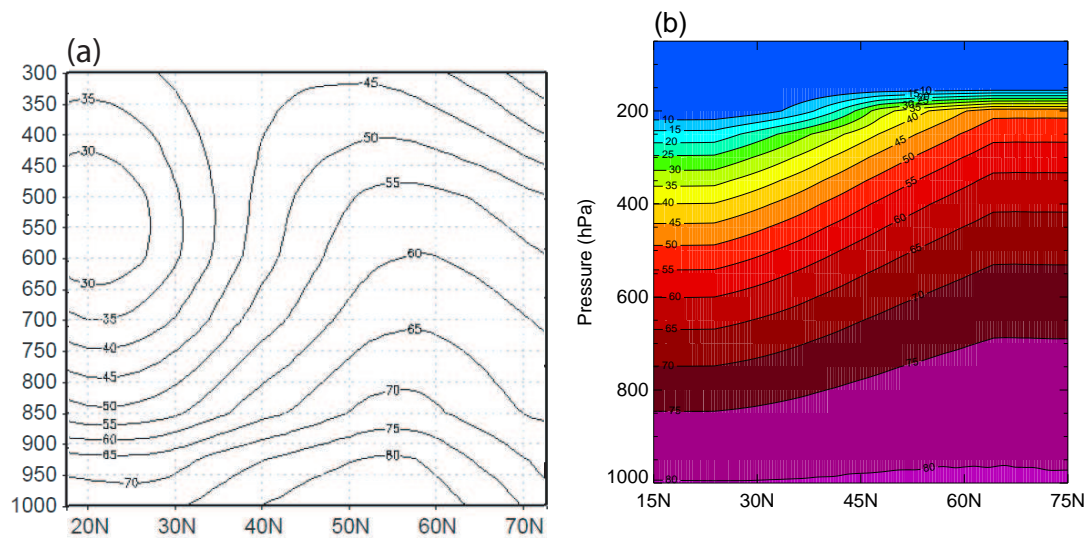


**Figure 2.7** Zonal-mean relative humidity (contoured, interval 5%), (a) Northern Hemisphere climatology from Pavan *et al.* (1999, Fig. 2) and (b) analytic expression defined by Equations 2.42 and 2.41.

Hemisphere winter zonal-mean state. Again, these profiles appear qualitatively similar, demonstrating that the moisture distribution represents a good match to observed atmospheric profiles. The only minor difference is that Gutowski *et al.*'s (1992) profile has slightly less moisture at low latitudes, due to having a colder sea-surface.

The initial state appears well-balanced and in a similar manner to Section 2.4.1, tests performed without adding the perturbation (Eqn. 2.39), but even with surface fluxes present, show that the jet and humidity profiles maintain their structures.

When the perturbation (Equation 2.39) is added to the moist initialisation, in the absence of a boundary-layer scheme (i.e. convection, cloud and microphysics are still present), the simulation denoted  $AM_0$  results, with MSLP and EKE evolution shown in Figure 2.9. Since the convection scheme is partly coupled to the boundary-layer scheme, it cannot operate in regions where it would have been triggered by the boundary-layer scheme (e.g. shallow cumulus), but it can operate where it is triggered by larger-scale flows (e.g. embedded convection in the WCB). It is clear that the presence of a moist atmosphere leads to a more energetic system which develops faster, reaching its minimum MSLP at day 9 before starting to decay. The EKE also peaks slightly before the dry simulation, and peaks 30% higher, similar to the 22% increase in EKE reported by

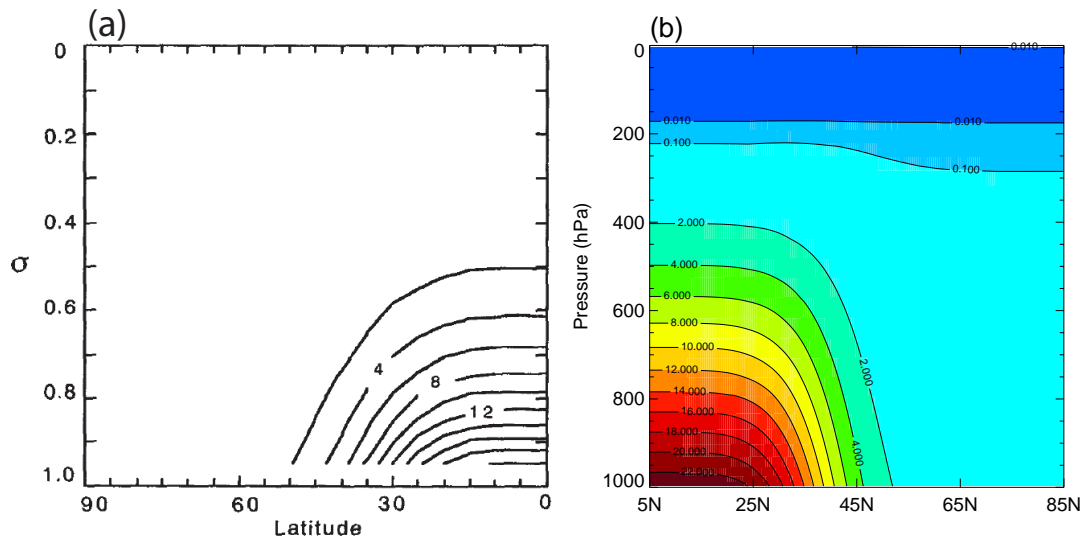


**Figure 2.8** Zonal-mean specific humidity (contoured, interval  $2 \text{ g kg}^{-1}$ ), (a) Northern Hemisphere climatology from Gutowski *et al.* (1992, Fig. 1b) and (b) initial state from this study.

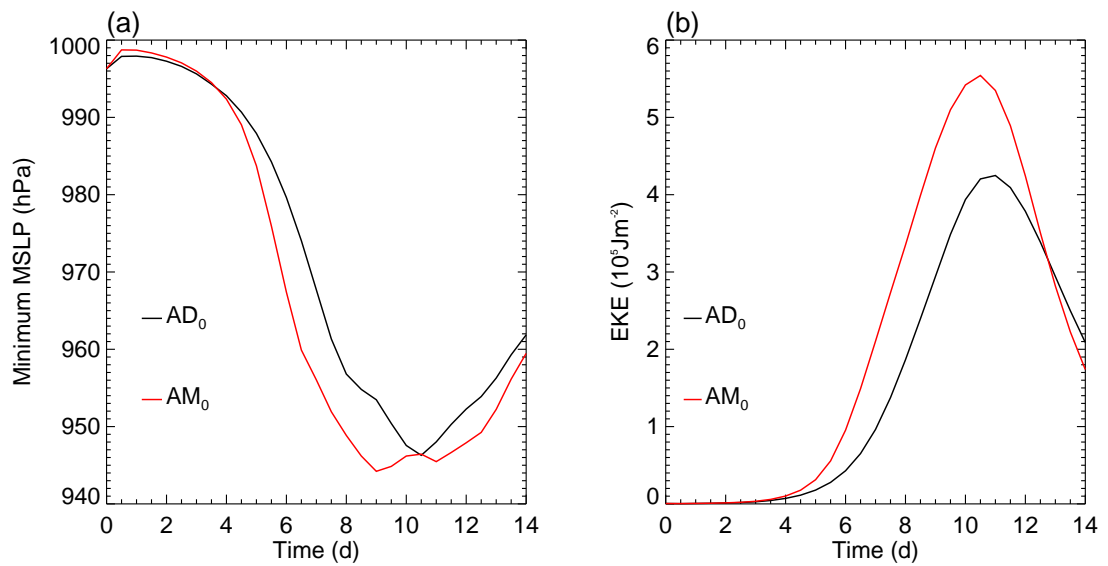


**Figure 2.9** Time series of (a) minimum sea-level pressure and (b) eddy kinetic energy, for the Cartesian life-cycle with and without the moisture initialisation, with no boundary layer.

Gutowski *et al.* (1992) for their wavenumber-7 simulations.

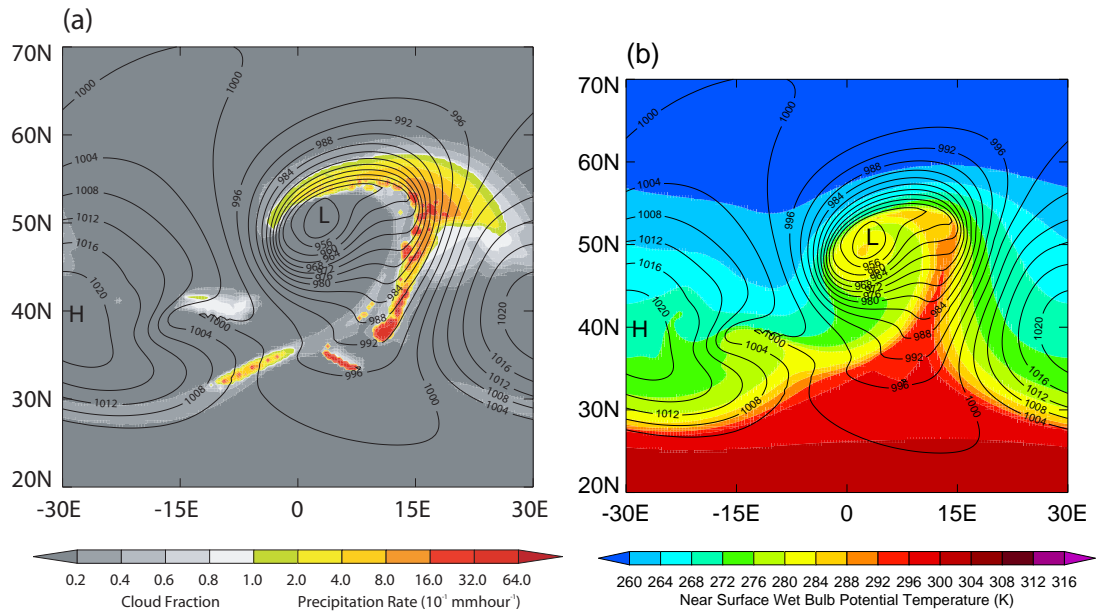


**Figure 2.10** (a) Cloud fraction (shaded) and precipitation rate (coloured) and (b) 20 m wet-bulb potential temperature (coloured), with pressure at mean sea-level (contoured, interval 4 hPa) overplotted on both, for the Cartesian simulation with moisture but no boundary layer at day 8.

Figure 2.10(a) shows a snapshot of simulation  $AM_0$  at day 8, demonstrating that without a boundary-layer scheme present the simulation appears unrealistic. Cloud and precipitation on the warm-conveyor belt (WCB), located around (15E, 50N), are still present, driven by the large-scale ascent. However, there is no other cloud (or precipitation) visible anywhere within the system. As discussed in Section 1.3.1, there are typically low-level stratocumulus and cumulus clouds formed behind the cold front for marine cyclogenesis. Their formation and existence is closely related to the surface fluxes and boundary-layer turbulence, which is not represented here, preventing their formation. Figure 2.10(b) shows how the cold-front is clearly visible in the wet-bulb potential temperature, with a sharp increase from  $\theta_w \approx 280$  K behind the front, to  $\theta_w \approx 290$  K within the WCB. There is also a weak warm-front located near (15E, 55N), which extends backwards around the low-centre. This system also appears to be generating some secondary cyclogenesis occurring near (-10E, 40N), although the reasons for this are not investigated here.

### 2.5.2 MOIST LIFE-CYCLE WITH BOUNDARY LAYER

Switching on the boundary-layer scheme should provide the most realistic simulation of mid-latitude cyclogenesis, since both moist processes and boundary-layer turbulence are being represented. This simulation is denoted  $AM_{BL}$ . The addition of the boundary-layer scheme now

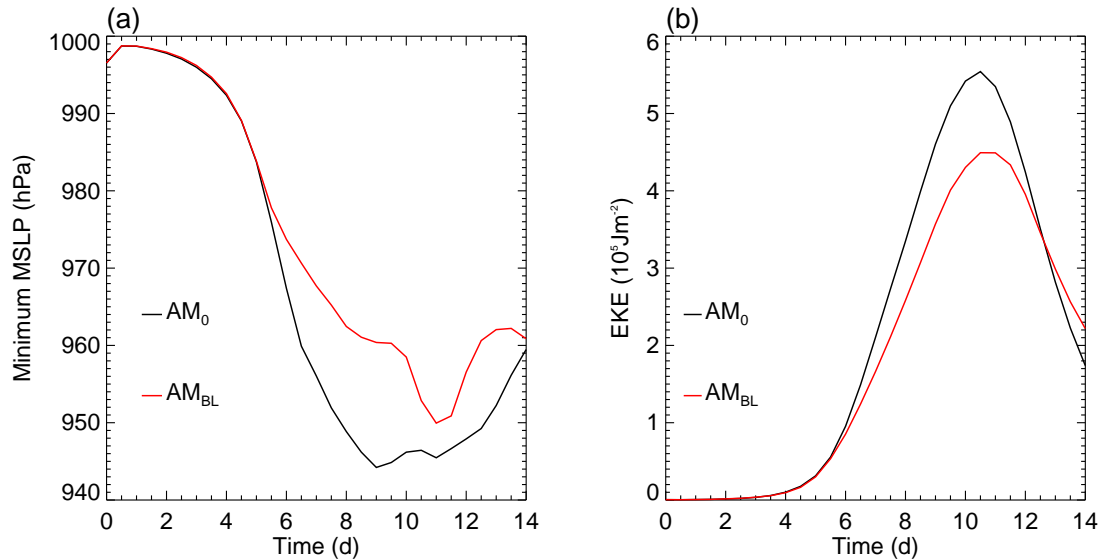


**Figure 2.11** Time series of (a) minimum sea-level pressure and (b) eddy kinetic energy, for the moist Cartesian life-cycle with and without the boundary-layer scheme operating.

allows surface latent-heat exchange and therefore evaporation from the sea-surface. This helps to maintain the moisture content of the atmosphere, since for run  $AM_0$ , moisture was being precipitated from the atmosphere, but not evaporated from the surface. This causes simulation  $AM_{BL}$  to decay more slowly than simulation  $AM_0$ . This is shown by the much quicker drop-off of EKE in simulation  $AM_0$  after day 10. It is also noticeable that the addition of the boundary layer has now caused only a 20% reduction in the peak EKE, much less than the 37% reduction seen in dry simulations. This is possibly due to Ekman pumping, creating vertical velocity near the cyclone centre and exporting large amounts of moisture into the mid-troposphere, which could trigger mid-level latent heat release causing the cyclone to intensify further. The MSLP shows a localised re-intensification between days 10 and 12. This is caused by latent heat release forcing a localised spin-up near the surface, but the feature is not large-scale as it does not appear in the EKE, and so is of little importance when considering the evolution of the whole system.

Figure 2.12 shows the spatial structure of the surface pressure, fronts, cloud fraction and precipitation rate on days 7 and 9 of simulation AM<sub>BL</sub>. It shows many features of a classical mid-

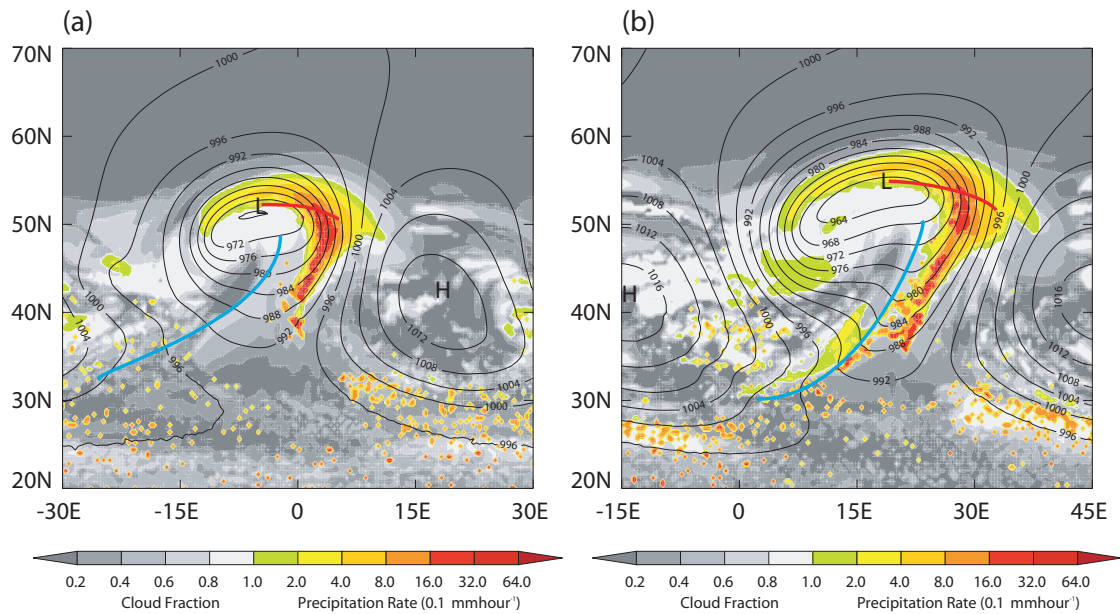


**Figure 2.12** Cloud fraction (shaded) and precipitation rate (coloured), with pressure at mean sea-level (contoured, interval 4 hPa) at (a) day 7 and (b) day 9 of simulation AM<sub>BL</sub>. Red and blue lines denote the warm and cold fronts respectively, diagnosed using the method of Hewson (1998).

latitude weather system, such as the main precipitation band in the warm-conveyor belt (WCB) to the east and south-east of the low centre. There is also some dry, cloud free air noticeable directly south of the low centre, immediately behind the cold front, which is associated with the dry intrusion. Further behind the cold front and to the west of the cyclone centre, low-level cloud (tops at  $\sim 3$  km) is formed within the cold-air outbreak. The shallow cumulus extends towards the centre of the anticyclone, but disappears to leave cloud-free air in the very centre of the high-pressure where there are light winds and little thermal advection. To the very south of the domain there is some scattered convective rainfall. By day 9 most of this lies along the trailing front to the south of the high, where there is some horizontal convergence. To the very north of the domain the air is cold and dry and therefore cloud-free with no precipitation.

The fronts shown in Figure 2.12 are identified using the objective method designed by Hewson (1998). This method looks for gradients in the wet-bulb potential temperature to identify frontal regions, before applying a masking function to remove thermally weak fronts and using the sign

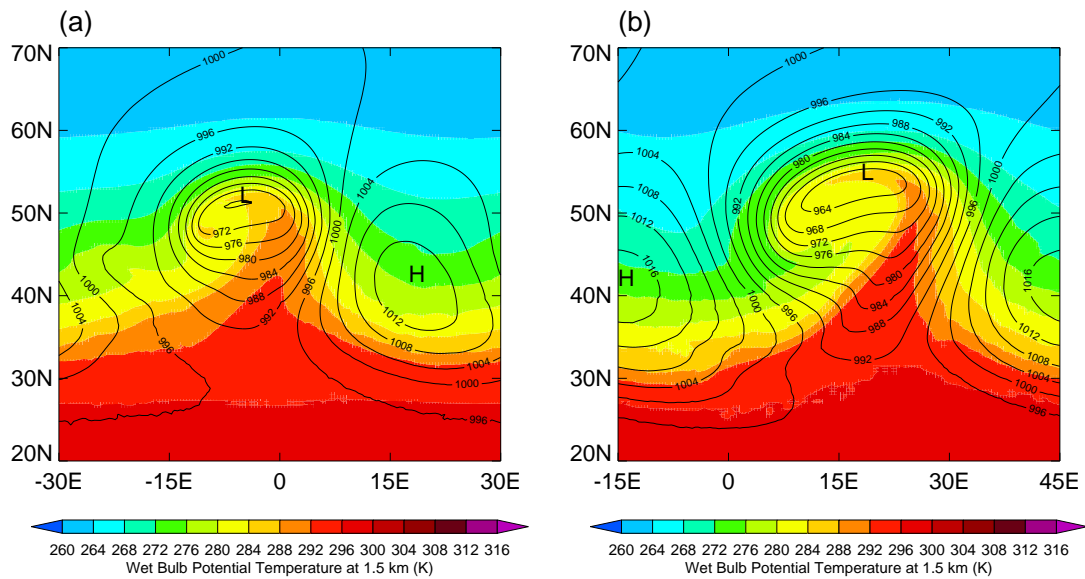


**Figure 2.13** Wet-bulb potential temperature at 1.5 km (coloured) and pressure at mean sea-level (contoured, interval 4 hPa) at (a) day 7 and (b) day 9 of simulation  $AM_{BL}$ .

of thermal advection to differentiate warm and cold fronts. The frontal locations can be seen in the wet-bulb potential temperature plots shown in Figure 2.13, with sharp gradients in  $\theta_w$  coincident with the frontal locations marked on Figure 2.12. This frontal pattern shows a clear T-bone structure, consistent with the Shapiro and Keyser (1990) model, demonstrating that this simulation is representative of real-world cyclogenesis. The WCB is characterised by the tongue of air extending polewards with almost constant wet-bulb potential temperature ( $\theta_w \approx 290$  K). This idealised simulation also shows many similarities to composites of real-world cyclogenesis events, such as those discussed by Field and Wood (2007).

### 2.5.3 INCLUSION OF RADIATION

In order to make the simulations truly “full-physics”, the radiation scheme should be switched on and a diurnal cycle of solar radiation should be included. This will not affect the surface temperatures, since there is very little diurnal cycle in sea-surface temperatures (SSTs) – indeed most forecast centres run with fixed SSTs for forecasts of up to 2 weeks. However, radiation will affect the temperature properties of both the clear sky and clouds. The clear sky will scatter incoming shortwave radiation and absorb/emit upwelling longwave radiation, whilst clouds will

absorb shortwave radiation at their tops, longwave radiation at their bottoms and emit longwave radiation both upwards and downwards.

The limited area domain creates problems for the implementation of radiation. The wavenumber 6 symmetry of the domain means that lower wavenumbers cannot be simulated within the model. However within the atmospheric heat engine, heat is transported north of 60N by wavenumbers 4 and lower (Jones, 1992). Therefore implementation of a radiation scheme in this region would result in unrealistic cooling of the atmosphere as longwave radiation is emitted but nothing replaces it. This has particularly important implications for the near-surface temperature structure. The atmosphere is cooling and the sea-surface temperature is fixed, which leads to an unstable potential temperature profile and a convective boundary layer growing. This effectively de-stabilises the atmosphere over large regions in the north of the domain.

This problem is also noticeable at other latitudes. It is speculated that the lack of a fully realistic tropical atmosphere in the simulation restricts the export of heat to mid-latitudes. The atmosphere cools too much by longwave emission, and the heat is not replaced by the Hadley circulation. This initial state is therefore unbalanced and the atmosphere becomes very unstable. As in Sections 2.4.1 and 2.5.1, if the initial state were balanced, running the simulation without the perturbation (Eqn. 2.39) should lead to no appreciable change in the atmospheric temperature profile. However, when this test is performed with the radiation scheme switched on, the static stability continually reduces across the whole domain, eventually leading to cyclogenesis being triggered by small instabilities within the model.

When the perturbation is added, the simulation appears to develop normally for several days, but by day 9 the atmospheric stability is so low that secondary cyclogenesis is triggered in an instability on the trailing front. The two cyclones merge and deepen rapidly. For this reason, simulations with radiation shall not be pursued any further here. In principle, some carefully chosen net warming could be implemented within the model to simulate the large-scale transports which are not captured. However, investigating simulations without radiation is also useful, as the aim is to understand the interaction between cyclogenesis events and the boundary layer. Running without radiation allows the to isolation of the boundary-layer response to forcing from the synoptic-scale only, rather than trying to disentangle the effects of a diurnal cycle or cloud-radiation interactions.

## 2.6 TYPE-B LIFE CYCLES

The Type-A life cycles discussed in Sections 2.4 and 2.5 represent the slowly developing waves which grow from normal-mode perturbation of the jet. However, as discussed in Section 1.3.2, many cyclogenesis events are triggered by a pre-existing upper-level trough, which can deepen rapidly into a strong cyclone over a period of hours. Therefore, a complimentary Type-B simulation is discussed in this section, which will prove useful for comparison and to test the robustness of results.

### 2.6.1 DRY SIMULATIONS

Beare (2007) developed an idealised model of Type-B cyclogenesis in the MetUM for his investigation on the role of the boundary layer in mid-latitude cyclones, and so this is used with some minor modifications. The model is based on previous work by Rotunno and Bao (1996) and Beare *et al.* (2003), and was shown by Beare (2007) to exhibit the main features of a Type-B cyclogenesis event. This model is again constructed on a Cartesian  $f$ -plane, and similar processes of defining a zonal jet with balanced temperature and pressure profiles are used as in Section 2.4.1. The basic state jet used by Beare (2007) was different from that given in Equation 2.38, but no less representative of what might be observed in the North-Atlantic storm track. To maintain consistency with results presented by Beare (2007), the initial zonal jet is defined in the same manner, as follows:

$$\begin{aligned}
 u(y, z) &= 25 \left( \frac{\sinh(0.7z/\mathcal{H})}{\sinh(0.7)} \right) \left[ 1 - \cos \left( \frac{2\pi y}{L_y} + \pi \right) \right] , \\
 &\quad z \leq \mathcal{H} \quad , \quad \frac{-L_y}{2} \leq y \leq \frac{L_y}{2} , \\
 u(y, z) &= 25 \exp \left( 0.7 \frac{N_s}{N_t} \left( 1 - \frac{z}{\mathcal{H}} \right) \right) \left[ 1 - \cos \left( \frac{2\pi y}{L_y} + \pi \right) \right] , \\
 &\quad z \geq \mathcal{H} \quad , \quad \frac{-L_y}{2} \leq y \leq \frac{L_y}{2} , \\
 u(y, z) &= 0 \quad , \quad \text{otherwise,}
 \end{aligned} \tag{2.43}$$

where  $L_y = 3000$  km is the jet width,  $\mathcal{H} = 9$  km is the tropopause height,  $N_t = 1.16 \times 10^{-2} \text{ s}^{-1}$  is the tropospheric Brunt-Väisällä frequency and  $N_s = 2N_t$  is the stratospheric Brunt-Väisällä

frequency. An upper level vortex is then added to this basic state, defined by

$$\begin{aligned}
 (u, v) &= 20 \exp\left(\frac{2\pi N_t(z - \mathcal{H})}{fL_y}\right) \frac{1}{r} \sin\left(\frac{2\pi r}{L_y}\right) (-y, x) \quad , \quad z \leq \mathcal{H} \quad , \quad r \leq L_y/2, \\
 (u, v) &= 20 \exp\left(\frac{2\pi N_s(\mathcal{H} - z)}{fL_y}\right) \frac{1}{r} \sin\left(\frac{2\pi r}{L_y}\right) (-y, x) \quad , \quad z \geq \mathcal{H} \quad , \quad r \leq L_y/2, \\
 (u, v) &= 0 \quad , \quad \text{otherwise,}
 \end{aligned}
 \tag{2.44}$$

where  $r = \sqrt{x^2 + y^2}$ . Once balanced temperature and pressure profiles are created, this vortex appears as an upper-level PV anomaly, and simulates how an upper-level trough can trigger cyclogenesis. Original simulations performed by Beare (2007) used a constant sea-surface temperature of 290 K. However, for consistency with the simulations presented in Section 2.4, the sea-surface temperature shall be defined in the same way – fixed equal to the lowest model level temperature at the initial time. This new simulation is denoted  $BD_{BL}$ , whilst Beare’s (2007) original simulation is denoted  $BD_{SST}$ , and the implications of this change to the sea-surface temperature will be discussed in Section 3.3.

Figure 2.14 shows plots of MSLP and potential temperature at 1.5 km for simulation  $BD_{BL}$ . It demonstrates that this is a rapidly developing system, which reaches maturity within 3 days.

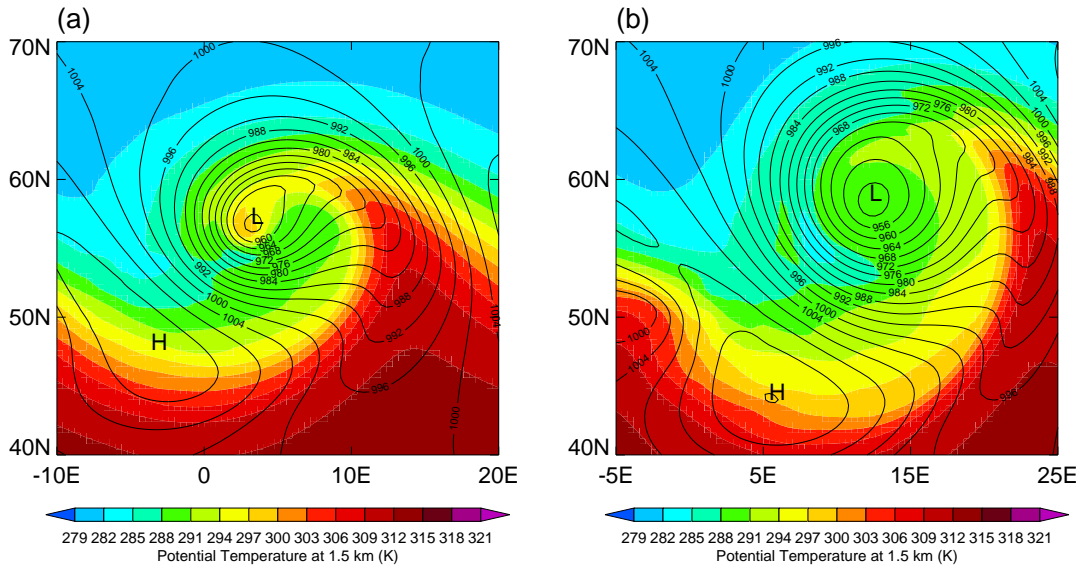


**Figure 2.14** Mean sea-level pressure (black contours, interval 4 hPa) and potential temperature at 1.5 km (colour contours), for the dry Type-B simulation with boundary-layer scheme at (a) 48 hours, and (b) 72 hours.

The pattern of MSLP and potential temperature shows a strong cold front located between (10E, 60N) and (0, 45N) at 48 hours, together with a warm front located from (10E, 60N) to (20E, 55N) and an occlusion wrapping around the low centre. By 72 hours, the occlusion has grown and the cyclone has intensified to its maximum and is now entering a barotropic decay phase.

There is a very strong pressure gradient to the south-west of the low centre, creating a low-level jet wrapping around the cyclone centre. There is also a warm seclusion noticeable around the low centre at 48 hours. The combination of low-level jet, warm seclusion and T-bone frontal structure are all features of the Shapiro and Keyser (1990) conceptual model, showing that this simulation is realistic in its development.

### **2.6.2 MOIST SIMULATIONS**

The benefit of defining Relative Humidity in Equations 2.42 and 2.41 is that the same RH profile can be used with other simulations that have different temperature profiles. Hence the RH profile defined in Equations 2.42 and 2.41 can be applied to the Type-B simulations, denoted  $BM_{BL}$ , although modifying the width of the jet to match the new jet width ( $L_y$ ).

Figure 2.15 shows the clouds and precipitation at 48 hours, along with the wet-bulb potential temperature for simulation  $BM_{BL}$ . The general structure of the cyclone is retained from the dry simulations, although the addition of moisture has, as expected, further intensified the system resulting in an  $\approx 8$  hPa deepening in the minimum MSLP. Figure 2.15(a) shows how the precipitation is aligned along the warm, cold and occluded fronts. There are also showers noticeable in the cold-air outbreak, located to the south-west of the low centre in the strong pressure gradient. Again, there is some drier, cloud free air immediately behind the cold front associated with the dry intrusion. Figure 2.15(b) shows a clear warm sector located ahead of the cold front, with  $\theta_w \approx 300$  K, with very sharp gradients of  $\theta_w$  across the warm and cold fronts.

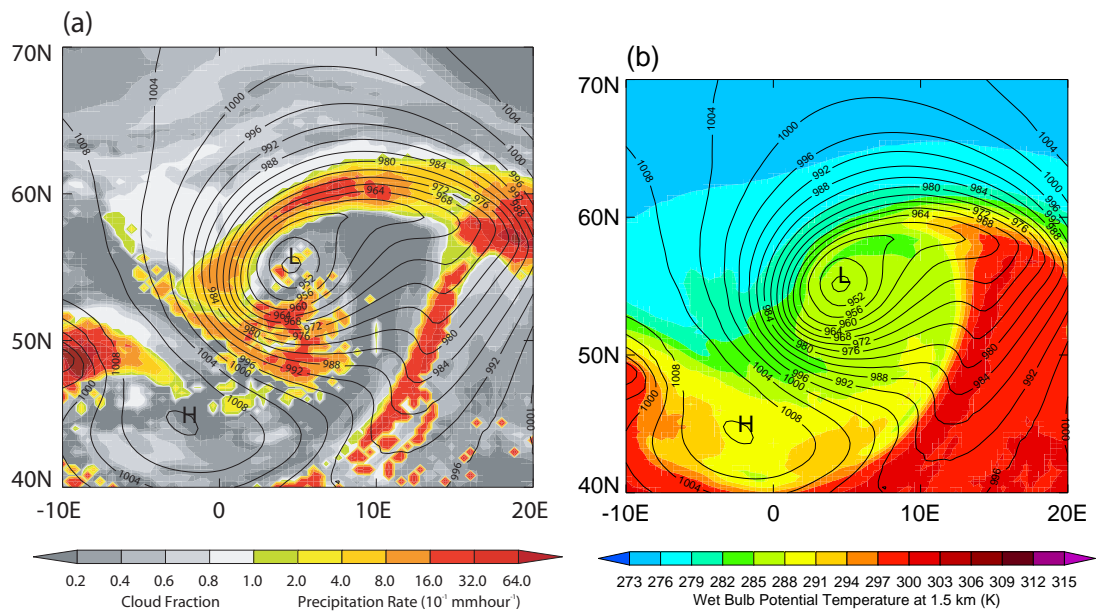


**Figure 2.15** (a) Cloud fraction (shaded) and precipitation rate (coloured) and (b) wet-bulb potential temperature at 1.5 km (coloured), with pressure at mean sea-level (contoured, interval 4 hPa) overplotted on both, for the moist Type-B simulation with boundary-layer scheme at 48 hours.

## 2.7 SUMMARY

This chapter has discussed the numerical model used in this thesis and the simulations of idealised cyclogenesis that are produced. There have been many previous studies of Type-A cyclogenesis of the LC1-type in models with no physical parameterisations (e.g. Thorncroft *et al.*, 1993; Balasubramanian and Garner, 1997; Wernli *et al.*, 1998; Polvani and Esler, 2007), and Section 2.4.2 demonstrated that simulation AD<sub>0</sub> displayed a similar structure and evolution. Simulations with parameterised boundary layers of the sort described in Section 2.3 (e.g. Adamson *et al.*, 2006; Sinclair *et al.*, 2008), are relatively fewer in number. However, simulation AD<sub>BL</sub> displayed many features described by these authors, consistent with similar features described in studies utilising differing boundary-layer parameterisations (e.g. Valdes and Hoskins, 1988; Branscome *et al.*, 1989). Simulations by Gutowski and Jiang (1998) provided the most useful comparison for simulation AM<sub>BL</sub>, since they included detailed moisture and boundary-layer parameterisations. Simulation AM<sub>BL</sub> was also compared to observed mid-latitude cyclogenesis events, demonstrating that common features (such as the warm-conveyor belt, cold and warm fronts and the cold air outbreak, described in Section 1.3), were all present. Table 2.1 lists the main simulations that

shall be discussed in the remaining chapters of this thesis, and the abbreviations used to describe them.

Abbreviation	Cyclone Type	Dry or Moist	Boundary-layer scheme
AD <sub>0</sub>	A	Dry	None
AD <sub>BL</sub>	A	Dry	Momentum and heat exchange
AD <sub>m</sub>	A	Dry	Momentum exchange only
AM <sub>0</sub>	A	Moist	None
AM <sub>BL</sub>	A	Moist	Momentum, heat and moisture exchange
BD <sub>BL</sub>	B	Dry	Momentum and heat exchange
BD <sub>m</sub>	B	Dry	Momentum exchange only
BD <sub>SST</sub>	B	Dry	Momentum and heat, SST=290 K
BD <sub>0</sub>	B	Dry	None
BD <sub>SBL</sub>	B	Dry	Momentum and heat exchange in the SBL only
BD <sub>CBL</sub>	B	Dry	Momentum and heat exchange in the CBL only
BM <sub>BL</sub>	B	Moist	Momentum, heat and moisture exchange

**Table 2.1** Table showing the different simulations discussed within this thesis and the abbreviations used for them.

Whilst this thesis will focus on the interaction of the boundary layer with cyclone waves, the model developed has many other potential uses. The use of the MetUM means that additional physical effects, such as sea-surface coupling, orographic or land-surface effects and atmospheric chemistry could be easily added to the simulations to investigate the large-scale response.

# CHAPTER 3:

# BOUNDARY-LAYER PROCESSES IN DRY

# LIFE CYCLES

## 3.1 INTRODUCTION

It has been long established that surface friction can significantly effect the development of mid-latitude cyclones, for example Anthes and Keyser (1979) present a simulation in which the cyclone is more than 20 hPa deeper when turbulent momentum fluxes are not included. Many other studies (e.g. Valdes and Hoskins, 1988; Jones, 1992; Adamson *et al.*, 2006) have demonstrated similar differences between cyclone simulations with and without boundary-layer parameterisations, and Chapter 2 demonstrated that this effect is replicated in the MetUM. But exactly how does the boundary layer produce these large-scale changes? Several alternative mechanisms have been suggested, but there is currently no conclusive answer to this question.

Traditionally, the barotropic Ekman pumping mechanism has been assumed to be the dominant process. Surface stress causes wind-turning in the atmospheric boundary layer, forcing convergence of near surface winds towards the low centre, which must create upward vertical motion due to continuity. This reduces cyclone growth by vortex squashing in the interior. Many studies (e.g. Card and Barcilon, 1982; Farrell, 1985) have parameterised the effects of the boundary layer in terms of an Ekman pumping velocity through the bottom boundary. These studies therefore implicitly assume that it is the action of Ekman pumping which causes the large-scale spin-down. Valdes and Hoskins (1988) compared an Ekman boundary layer parameterisation with other methods such as Rayleigh friction and an explicit boundary layer with constant value of  $K_m$ , finding a similar effect on the cyclone growth rate from each method. Recently, Beare (2007) has shown that Ekman pumping can still be a good method of interpreting cyclone responses to boundary-layer processes, particularly in cyclone systems with strong low-level jets.

Mid-latitude cyclones are inherently baroclinic in nature, and therefore potential vorticity (PV) is often used as the natural variable to describe their evolution. Cooper *et al.* (1992) discussed mechanisms by which significant amounts of PV could be generated in frontal boundary layers, prior to occlusion (i.e. during the cyclone growth phase). Stoelinga (1996) investigated frictional PV generation (amongst other methods of PV generation) in a case-study of maritime cyclogenesis. It was demonstrated that significant generation of positive PV occurred in the warm-conveyor belt region, due to frictional processes, although the consequences of this for cyclone development were not explained. Adamson *et al.* (2006) attempted to rectify this, describing a new mechanism for the frictional spin-down of an extratropical cyclone, based on baroclinic potential vorticity generation. PV generated in the boundary layer (due to a component of stress anti-parallel to the tropospheric thermal wind) is advected along the warm-conveyor belt and vented from the boundary layer. It turns cyclonically and accumulates above the low centre as a positive PV anomaly of large horizontal extent, but trapped between isentropes in the vertical. This shape is associated mainly with increased static stability (Hoskins *et al.*, 1985), inhibiting communication between the upper- and lower-level features of the developing wave, and so reducing growth. Plant and Belcher (2007) extended the work of Adamson *et al.* (2006) to include surface sensible heat fluxes, demonstrating that the baroclinic PV mechanism was robust in the presence of surface heat fluxes, and that their inclusion did little to modify the large-scale development.

This chapter aims to investigate how surface fluxes are communicated to the free troposphere by boundary-layer dynamics in dry simulations. Expanding on the work of Adamson *et al.* (2006) and Beare (2007), Section 3.2 will investigate the Ekman pumping and baroclinic PV mechanisms in a range of idealised cyclone models with momentum-only boundary-layer parameterisations, demonstrating that their results were not influenced by their choice of idealised model, but rather that the concepts are general and should be applicable to real-world cyclones. The role of surface heat fluxes will be investigated in Section 3.3, demonstrating how the choice of sea-surface temperature becomes important when these effects are included. A PV inversion is conducted in Section 3.4 and the link between the Ekman and baroclinic PV mechanisms will be investigated in Section 3.5, demonstrating that they are not competing effects. Simulations are presented in which features of both mechanisms can be observed and can both play a role in determining and communicating surface effects to the cyclone interior.

## 3.2 FRICTION ONLY SIMULATIONS

### 3.2.1 BAROTROPIC VORTEX

Many studies have considered the problem of Ekman spin-down of a barotropic vortex: for example, Greenspan (1969) provided a detailed analysis based on laboratory experiments and theoretical calculations. The aims of this subsection are to show that the Met Office Unified Model (MetUM) can simulate a barotropic vortex and reproduce the expected Ekman circulation as the mechanism by which the boundary layer spins down the vortex.

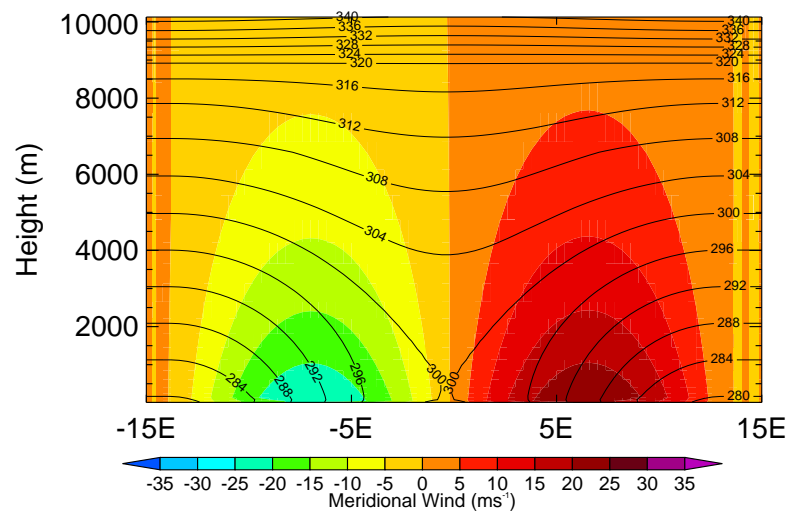
To make the problem more relevant to mid-latitude cyclones, a “warm core” vortex is chosen, which appears qualitatively similar to the final barotropic decay stages of a mid-latitude cyclone (Shutts and Thorpe, 1978). The model is constructed on a Cartesian  $f$ -plane, with the initial wind field prescribed as follows:

$$\begin{aligned} (u, v) &= 20 \exp\left(\frac{-2\pi N_t z}{f L_y}\right) \frac{1}{r} \sin\left(\frac{2\pi r}{L_y}\right) (-y, x) \quad , \quad r \leq L_y/2, \\ (u, v) &= 0 \quad , \quad \text{otherwise,} \end{aligned} \quad (3.1)$$

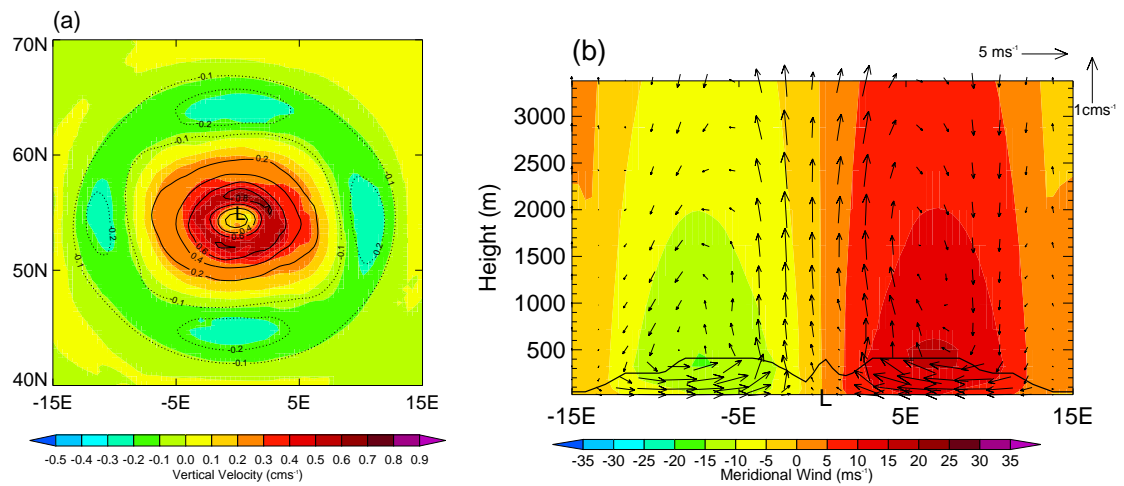
where  $r = \sqrt{x^2 + y^2}$ . This formula gives the strongest vorticity at the surface at the vortex centre, decaying with height and towards the vortex edge. Similar calculations as those described in Section 2.4.1 are used to create balanced temperature and pressure fields. The warmest temperatures are found at the vortex centre, cooling with increasing radius. The initial state winds and potential temperature are shown in Figure 3.1. The model is run without surface sensible heat fluxes, and no additional numerical diffusion or external forcing are applied. Therefore, only boundary-layer momentum fluxes and model dynamics can determine the evolution of the system. If the model is run with no boundary-layer scheme, there is no appreciable reduction in the vortex’s minimum sea-level pressure or vorticity during the experiment period of 5 days, and therefore any spin-down effects must be due to surface friction.

Figure 3.2 shows the wind fields produced by this simulation. Figure 3.2(a) demonstrates that the diagnosed vertical velocity on the boundary-layer top ( $h$ , Section 2.3.4) matches very well the Ekman pumping velocity defined as

$$w_{\text{Ek}} = \frac{1}{\rho f} \mathbf{k} \cdot \nabla \times \boldsymbol{\tau}_s, \quad (3.2)$$



**Figure 3.1** East-west cross section through the vortex centre showing the initial condition  $v$ -wind (coloured) and potential temperature (contoured, interval 4 K).



**Figure 3.2** (a) Model derived vertical velocity at the boundary-layer top (coloured) and Ekman pumping velocity (contoured, negative values dotted) after 24 hours. (b) East-west cross-section through the low centre showing  $(u, w)$  wind vectors and  $v$ -wind (coloured). The solid black line represents the boundary-layer top.

where  $\mathbf{k}$  is a unit vector in the  $z$ -direction. Figure 3.2(b) then demonstrates how the anticipated Ekman circulation is created within this system. Low-level winds converge towards the low centre within the boundary layer, inducing vertical motion at the boundary-layer top. This vertical motion acts to squash vortex tubes within the interior, reducing the vorticity. There is some divergence at upper levels and descending air far from the low centre to complete the circulation pattern.

According to the barotropic vorticity equation, the spin-down of the relative vorticity should follow

$$\xi = \xi_0 \exp(-t/\tau) \quad , \quad \tau = \frac{(\mathcal{H} - h)}{f} \sqrt{\frac{2f}{K_m}}. \quad (3.3)$$

Typical mid-latitude scalings are chosen as

$$\mathcal{H} = 10 \text{ km} \quad , \quad h = 1 \text{ km} \quad , \quad f = 10^{-4} \text{ s}^{-1} \quad , \quad K_m = 10 \text{ m}^2\text{s}^{-1}, \quad (3.4)$$

to calculate  $\tau$  and the theoretical spin-down rate. This is compared to the actual vorticity, as measured in the mid-troposphere in Figure 3.3. As shown, the simple calculation does a very

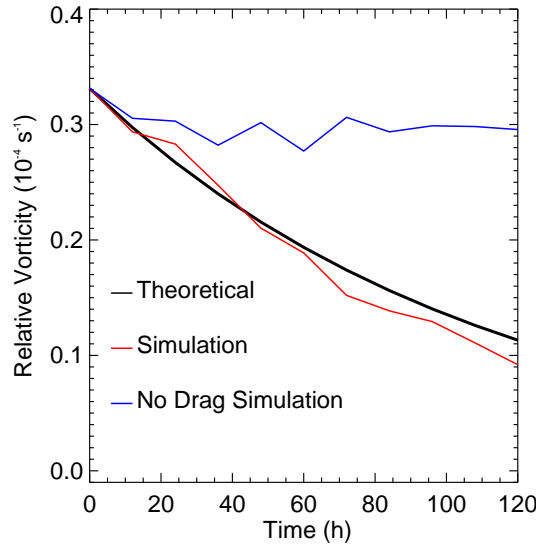


**Figure 3.3** Time series showing the theoretically-calculated decay in relative vorticity (Eqn. 3.3) with the observed mid-tropospheric ( $\mathcal{H}/2$ ) values in the simulation. Also shown are the observed values for the dynamics-only simulation.

good job of capturing the spin-down of this system over the 5 days of the experiment. It also demonstrates that the choice of  $K_m = 10 \text{ m}^2\text{s}^{-1}$  is reasonable, i.e. it is the right order of magnitude.

Also shown is the corresponding diagnostic for the simulation without a boundary layer present, confirming that there is no significant spin-down from numerical diffusion or other factors.

Therefore, the Ekman pumping mechanism appears robust for a barotropic vortex within the MetUM, and it is anticipated that it will prove important as cyclones enter their barotropic decay phase. However, this thesis is concerned with how the boundary-layer modifies cyclogenesis events. Therefore, since the baroclinic PV mechanism is concerned with modifying the cyclone growth-rate, it should be more important during the baroclinic growth phase.

### **3.2.2 EADY MODEL**

Section 1.2.2 discussed how the Eady (1949) model can be used to obtain reasonable estimates for the wavelength and growth rate of a mid-latitude cyclone. Model solutions were established for frictionless flow, under the assumption that  $w = 0$  on the lower and upper boundaries. However, if it is assumed that the bottom boundary represents the boundary-layer top, Section 3.2.1 has demonstrated that there is a component of vertical velocity at the lower boundary, driven by Ekman pumping. Therefore, this effect can be included into the Eady model, including a nonzero value of  $w$  in the lower boundary condition (Eqn. 1.4). Previous studies (e.g. Pedlosky, 1979; Blumen, 2001) have focussed on how the inclusion of an Ekman pumping velocity at one or both boundaries can modify the Eady growth rate, and even bring stability to the system when large amounts of friction are added. Here, it is investigated how the inclusion of “realistic” Ekman pumping at only the lower boundary affects the magnitude of the cyclone growth rate, and how this compares to changes in the static stability that could be caused by the baroclinic PV mechanism. This will allow the reduction in growth rates to be compared to the observed reduction in growth rates, discussed in Section 2.4.3 for idealised numerical simulations including a boundary-layer parameterisation. Pedlosky (1979) discusses how the Ekman pumping velocity can be related to the streamfunction by combining Equation 3.2 with a parameterisation such as Equation 2.24. Assuming  $K_m$  is constant yields

$$w_h = \sqrt{\frac{K_m}{2f}} \nabla_2^2 \Psi_g. \quad (3.5)$$

Here, this form of  $w_h$  is included into the surface boundary condition of the Eady model, modifying Equation 1.6a as follows:

$$(-\omega Nk)B + \left( \frac{g}{\theta_0} \frac{\partial \theta}{\partial y} k + N^2 \sqrt{\frac{K_m}{2f}} ik^2 \right) A = 0. \quad (3.6)$$

The eigenvalue problem is now a complex one, meaning the inclusion of friction changes both the growth rate and phase speed of the wave. Whilst it is possible to write down an analytic expression for  $\omega$  in the same manner as Equation 1.8, it is a very complicated expression, so instead the growth rate ( $\sigma$ ) is illustrated graphically in Figure 3.4. Again, typical mid-latitude

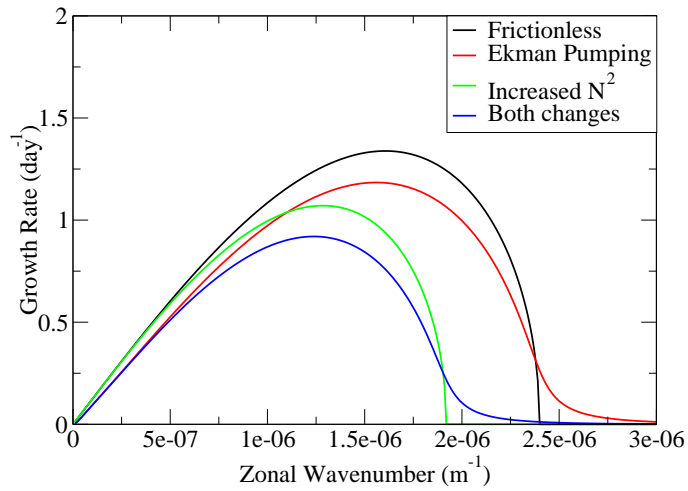


**Figure 3.4** Growth rate ( $\sigma$ ) curves for the basic Eady model (black curve), Eady model with Ekman pumping (red), Eady model with 25% increased Static Stability ( $N = 0.0125 \text{ s}^{-1}$ ) (green) and Eady model with both changes (blue).

values similar to Equation 3.4 are chosen:

$$\begin{aligned} \mathcal{H} = 10 \text{ km} \quad , \quad f = 10^{-4} \text{ s}^{-1} \quad , \quad K_m = 10 \text{ m}^2 \text{ s}^{-1} \quad , \\ \frac{g}{\theta_0} \frac{\partial \theta}{\partial y} = -\frac{fU}{\mathcal{H}} \quad , \quad U = 50 \text{ ms}^{-1} \quad , \quad N = 10^{-2} \text{ s}^{-1}. \end{aligned} \quad (3.7)$$

The inclusion of Ekman pumping acts to reduce the peak growth rate. It also introduces an instability at shorter wavelengths (high wavenumber), removing the so-called “short-wave cutoff” and allowing waves to grow with wavenumbers up to  $3 \times 10^{-6} \text{ m}^{-1}$ . However, the overall effect of the Ekman pumping is only a modest reduction of 12% in the peak growth rate, nowhere near the observed reduction of  $\approx 35\%$  reported by Adamson *et al.* (2006) and shown in Section 2.4.3.

Trying to incorporate the baroclinic PV mechanism into this QG framework is not easy. The QG analysis performed in Section 1.2.2 assumes that  $N$  is a constant in time, and this is an assumption that is not easy to relax. However, the effect of the PV anomaly on the average tropospheric static stability can be incorporated, simply by increasing the value of  $N$  used in Equation 1.8. Adamson *et al.* (2006) showed that the baroclinic PV mechanism lead to a 25% increase in the interior static stability, and therefore a simple estimate of the baroclinic PV mechanism's effect on the growth rate can be obtained by setting  $N = 0.0125 \text{ s}^{-1}$ . These results are shown on Figure 3.4, and demonstrate that increased static stability reduces the peak growth rate, but also shifts the growth rate curve towards longer wavelengths (lower wavenumbers). The reduction in the peak growth rate is only 20% for this scenario, still somewhat short of the observed 35%. Adamson *et al.* (2006) discuss how some of this difference comes from the curve shifting towards lower wavenumbers. Since their simulations had a fixed zonal wavenumber, the cyclone could not develop at its optimal size. Supposing the wavenumber was an optimal perturbation for the frictionless case, the wavenumber is fixed at  $k = 1.61 \times 10^{-6} \text{ m}^{-1}$  and the case with increased static stability now shows a 30% reduction.

When both the Ekman and PV mechanisms are accounted for (i.e. Ekman pumping is included at the surface and the static stability is increased by 25%, also shown on Figure 3.4), features of both are incorporated into the growth rate curve. The peak is reduced and shifted towards lower wavenumbers, but the short-wave cutoff also disappears at high wavenumbers. The reduction in the peak growth rate is now 31%, whilst the reduction in the growth rate at fixed wavenumber is 43%. These values are more representative of the observed 35% reduction, and demonstrate that both mechanisms may be important during the baroclinic growth phase of a mid-latitude cyclone.

The Eady model also demonstrates how cyclone growth rate is very sensitive to changes in the static stability. To achieve a 35% reduction in the growth rate from Ekman pumping alone, the eddy diffusivity would need to be  $\sim 100 \text{ m}^2\text{s}^{-1}$ , however, Section 3.2.1 demonstrated that a typical value of  $K_m = 10 \text{ m}^2\text{s}^{-1}$  was reasonable for an Ekman boundary layer. Direct model output of  $K_m$  for the simulations AD<sub>m</sub> and BD<sub>m</sub> demonstrates that  $K_m$  increases from zero at the surface to a maximum at  $\approx h/3$  before decaying back to zero at  $h$ . The maximum value rarely exceeds  $50 \text{ m}^2\text{s}^{-1}$ , with the boundary-layer averaged value typically not greater than  $20 \text{ m}^2\text{s}^{-1}$ . By contrast, the 25% increase in static stability required to achieve this growth rate reduction has

been shown to occur in the presence of the baroclinically-generated PV anomaly by Adamson *et al.* (2006) and Plant and Belcher (2007). It is also interesting to note that the most efficient spin-down occurs in the presence of both mechanisms, and their interaction shall be discussed in Section 3.5.

### 3.2.3 TYPE-A CYCLOGENESIS

The baroclinic PV mechanism discussed in Adamson *et al.* (2006) was discovered in simulations of a Type-A cyclone, and so it is anticipated that their results should be easily reproducible with a Type-A cyclone simulation in the MetUM. This simulation has no surface heat-flux parameterisation and is denoted AD<sub>m</sub>.

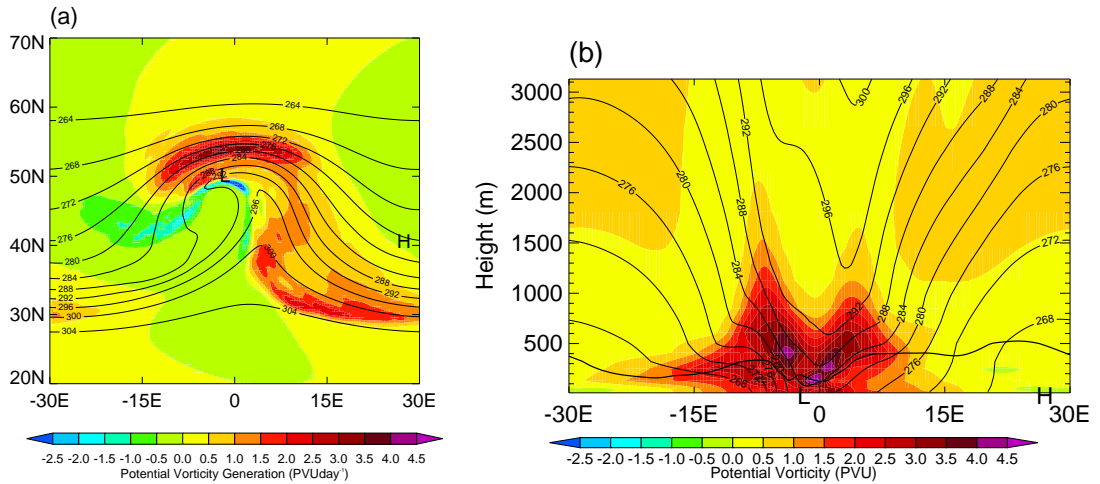


**Figure 3.5** (a) Boundary-layer depth-averaged potential vorticity generation by the baroclinic mechanism (coloured) and potential temperature at 1 km (contoured, interval 4 K) at day 8 of simulation AD<sub>m</sub>. (b) East-west cross-section through the low centre showing potential vorticity (coloured) and potential temperature (contoured, interval 4 K). The solid black line represents the boundary-layer top.

The depth-averaged baroclinic generation of PV within the boundary layer is given by

$$[G_B] = \frac{1}{\rho^2 h^2} \mathbf{k} \times \boldsymbol{\tau}_s \cdot (\nabla_2 \theta)_h, \quad (3.8)$$

where the subscript  $h$  denotes a quantity evaluated at the boundary-layer top. Figure 3.5(a) shows this baroclinic PV generation at day 8 of simulation AD<sub>m</sub>, with Figure 3.5(b) showing a cross-

section through the low centre at the same time. It is clear that baroclinically-generated PV is being ventilated from the boundary layer and accumulating as a PV anomaly above the cyclone centre. The location of generation is split into two areas. One area, shown between 0 and 30E, 30 and 45N would be ventilated along the warm-conveyor belt consistent with Adamson *et al.* (2006). The other area, shown between  $-10$  and 10E, 50 and 55N, shows similarity to the LC2 simulations discussed by Plant and Belcher (2007), suggesting that ventilation is partly by the cold-conveyor belt.

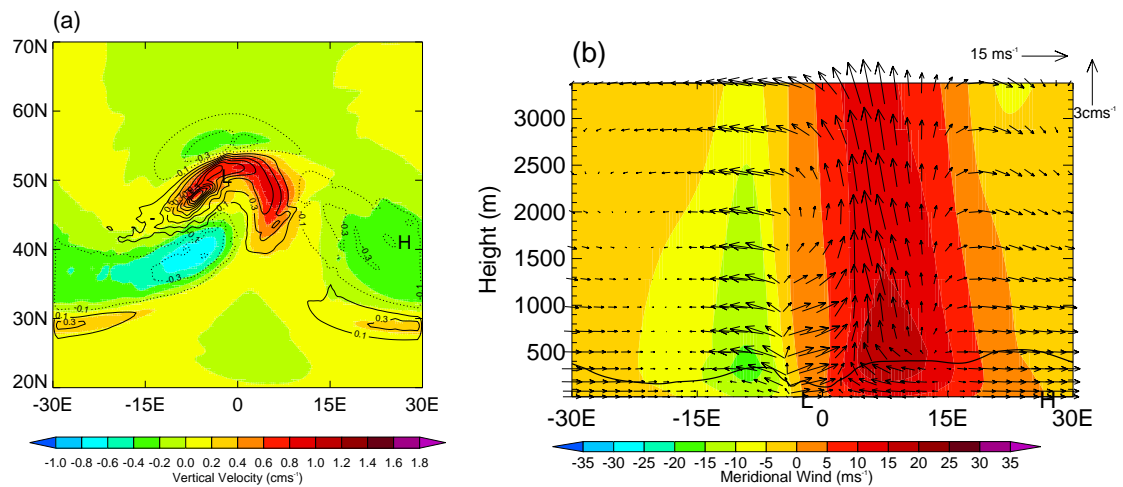


**Figure 3.6** (a) Model derived vertical velocity at the boundary-layer top (coloured) and Ekman pumping velocity (contoured, interval  $0.2 \text{ cm s}^{-1}$ , negative values dotted) after 8 days of simulation  $\text{AD}_m$ . (b) East-west cross-section through the low centre showing  $(u, w)$  wind vectors and  $v$ -wind (coloured). The solid black line represents the boundary-layer top.

Figure 3.6(a) shows the vertical velocity at the boundary-layer top and Ekman pumping velocity, as defined in Equation 3.2. It can be seen that the Ekman pumping velocity is under-estimating the boundary-layer top vertical velocity in the warm-conveyor belt region, but over-estimating it around the low centre. Adamson *et al.* (2006) did not focus in any detail on the relationship between Ekman pumping and vertical velocity, but Figure 3.6(a) suggests that Ekman pumping is playing a role in the low-level ascent of the warm-conveyor belt. This suggests some interaction between the two mechanisms. Without Ekman pumping, baroclinically-generated PV would not be ventilated on the WCB as efficiently, and therefore would not provide such a good spin-down mechanism. This will be discussed further in Section 3.5.

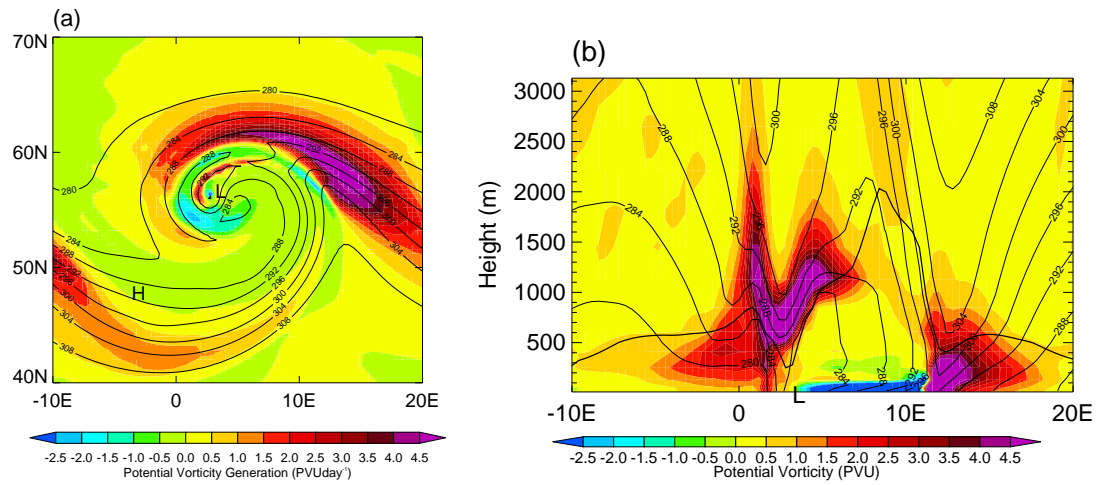
Figure 3.6(b) shows a cross-section through the low centre, showing some key differences to Figure 3.2. The strongest ascent is no longer located over the low centre, but is now displaced to the east, coincident with the warm-conveyor belt ascent. This ascent is forced by convergence, caused by large-scale ageostrophic motions rather than boundary-layer frictional convergence. This explains why the WCB ascent shown in Figure 3.6(a) is greater than the Ekman pumping velocity, since Equation 3.2 does not account for the large-scale convergence that may be happening above the surface. However, it is also clear that there is some convergence in the boundary layer below the WCB, which is, in part, caused by frictional convergence. It is also not obvious from Figure 3.6(b) whether an Ekman-type circulation pattern with low-level convergence and upper-level divergence has been created, and therefore not clear how vortex tubes would be squashed in the cyclone interior. The circulation appears to be one of large-scale origin, with ascent ahead of the low centre in the WCB region and large-scale subsidence in the region of the high pressure.

#### 3.2.4 TYPE-B CYCLOGENESIS

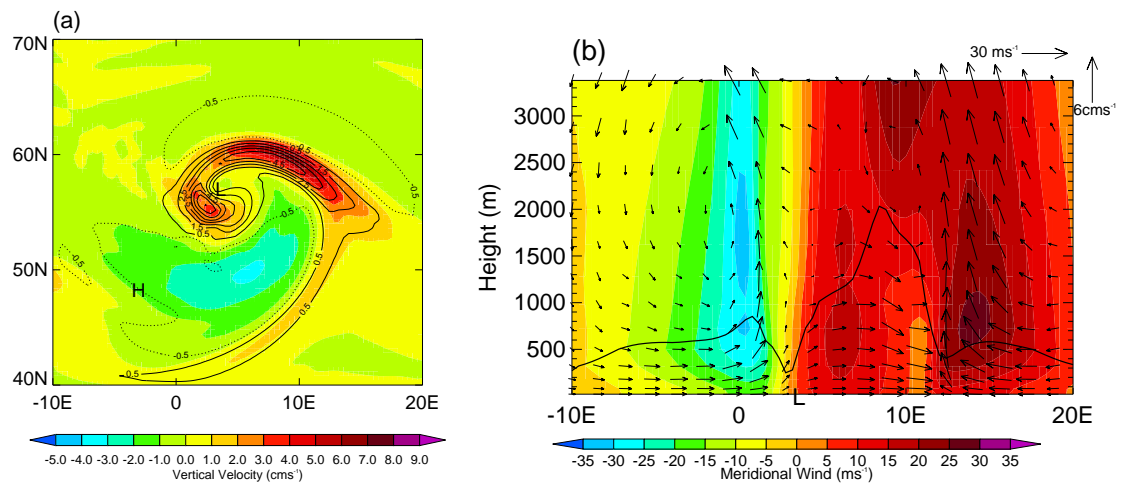
The timescales involved with Type-B cyclogenesis are much shorter than with Type-A, and therefore it is not immediately clear that the baroclinic PV mechanism will have time to operate. The generation, transport and accumulation of PV is not instantaneous, and how the timescale of the baroclinic frictional mechanism is related to the cyclone development timescale was not established in Adamson *et al.* (2006).

Figure 3.7(a) shows the baroclinic PV generation at 48 hours of simulation  $BD_m$ , with Figure 3.7(b) showing a cross-section through the low centre at the same time. It is clear that the PV generation is much stronger than in simulation  $AD_m$  (Figure 3.5(a)), due to the larger wind-speeds and temperature gradients. The boundary-layer top ascent is stronger (Figure 3.8(a)) and so this PV can be generated and ventilated much quicker. All processes are closely linked to the timescale of cyclone development, and therefore the PV mechanism appears to be operating within this Type-B simulation.

Figure 3.8 shows similarities to Figure 3.6. Although the magnitude of the vertical velocity is much greater in simulation  $BD_m$ , the pattern and relation between Ekman pumping and vertical velocity is similar. The Ekman pumping velocity provides a good estimate of the vertical velocity



**Figure 3.7** (a) Boundary-layer depth-averaged potential vorticity generation by the baroclinic mechanism (coloured) and potential temperature at 1 km (contoured, interval 4 K) after 48 hours of simulation  $BD_m$ . (b) East-west cross-section through the low centre showing potential vorticity (coloured) and potential temperature (contoured, interval 4 K). The solid black line represents the boundary-layer top.



**Figure 3.8** (a) Model derived vertical velocity at the boundary-layer top (coloured) and Ekman pumping velocity (contoured, interval 1 cms<sup>-1</sup>, negative values dotted) after 48 hours of simulation  $BD_m$ . (b) East-west cross-section through the low centre showing  $(u, w)$  wind vectors and  $v$ -wind (coloured). The solid black line represents the boundary-layer top.

in the WCB region, but over-predicts the vertical velocity around the low centre. A cross-section of wind vectors through the low centre, shown in Figure 3.8(b), demonstrates that the Ekman circulation is not as clear as it was in Figure 3.2. The circulation appears robust to the west of the cyclone centre, but to the east of the cyclone centre, the warm-conveyor belt and frontogenesis are having a large effect on the wind field. The cold front located near 12E in the cross-section can be seen in the potential temperature field (Fig. 3.7(a)), with a shallow boundary layer ahead and a deep boundary layer behind, consistent with Sinclair *et al.* (2010b). The PV and PV generation is located ahead of the front, in the warm air, suggesting that ventilation is by the warm-conveyor belt.

The meridional windspeeds are much stronger on the western side of the low centre, forced by a low-level jet wrapping around the cyclone centre. This forces the PV anomaly to be more vertical in structure, a shape that suggests there could be some significant vorticity associated with the anomaly (Hoskins *et al.*, 1985), in addition to the increased static stability.

### 3.3 SURFACE HEAT-FLUX EFFECTS

The simulations discussed in Section 3.2 contain a momentum-flux only boundary-layer parameterisation. More realistic simulations should account for the effects of heat exchange with the surface, and this was considered by Plant and Belcher (2007) in their Type-A cyclone simulations. The choice of sea-surface temperature (SST) was only indirectly important for the momentum-flux only simulations, since  $C_D$  (Eqn. 2.15) and  $K_m$  (Eqn. 2.25) depend on the stability. However, tests have shown that using different SSTs in the momentum-flux only simulations produces only very minor changes. When the surface sensible heat-flux is included, the choice of SST becomes more important as it directly influences  $H_s$  (Eqn. 2.10b), and Plant and Belcher (2007) chose to fix a meridional gradient in the SST, equal to the initial temperature of the lowest model level. This made the simulations qualitatively similar to simulation AD<sub>BL</sub>, and their results suggested that the inclusion of surface heat fluxes had little effect on the baroclinic PV mechanism.

Beare (2007) also discussed the effect of the boundary layer on Type-B cyclones in a simulation that included surface heat-flux effects. However, he chose the SST to have no meridional variation, instead fixing it at a constant value of 290 K across the domain (simulation BD<sub>SST</sub>).

His results showed a dramatically different boundary-layer PV distribution than those of Plant and Belcher (2007), and he found little evidence for the baroclinic PV mechanism described by Adamson *et al.* (2006). Therefore, it appears as though surface heat fluxes and the sea-surface temperature can play an important role in the boundary-layer PV budget.

The choice of SST in simulation  $BD_{SST}$  has considerable effect on the evolution of the boundary layer. The low SST relative to the overlying air in the warm sector gives rise to a shallow (as little as 50 m in places, but on average about 400 m) and highly stable boundary layer. The large negative surface heat fluxes in this region lead to the boundary-layer PV budget being dominated by surface heat-flux generated PV, given by

$$[G_H] = -\frac{(\zeta_z)_h H_s}{\rho^2 c_p h^2}. \quad (3.9)$$

It is this PV which is seen in Figure 3.9(a), rather than PV generated by baroclinic processes (Eqn. 3.8).

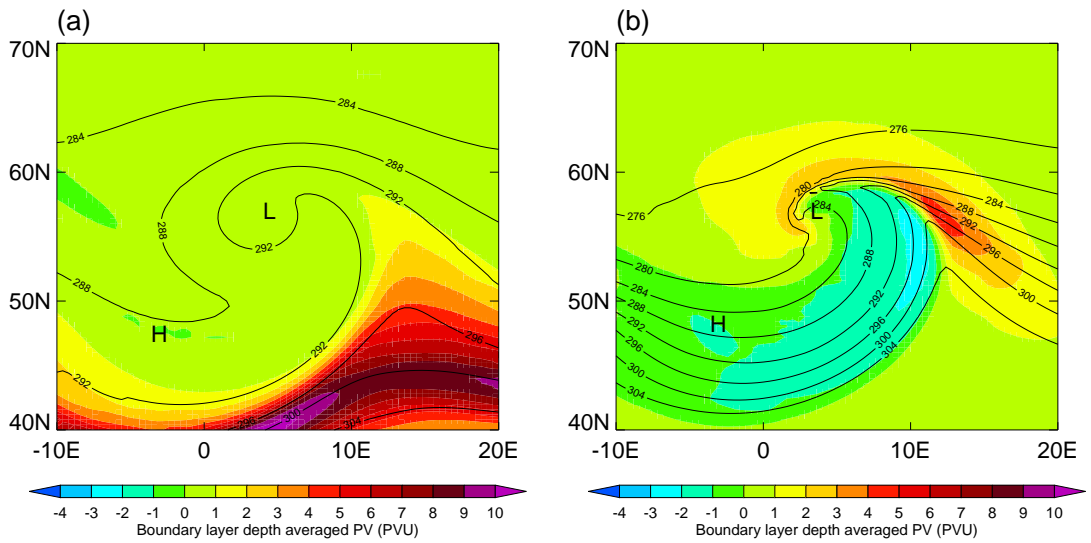


**Figure 3.9** Boundary-layer depth-averaged potential vorticity (coloured) and 20 m potential temperature (contoured, interval 4 K) at 48 hours for (a) simulation  $BD_{SST}$  and (b) simulation  $BD_m$

The importance of the surface heat-flux pattern under conditions of a horizontally uniform SST field is demonstrated by Figure 3.9(b), which shows results from simulation  $BD_m$ . Comparing Figure 3.9(b) to Figure 3.9(a) shows that the PV is now located to the north and east of the cyclone (between 5-15E, 50-60N), confirming that the boundary-layer PV in simulation  $BD_{SST}$  is

predominantly generated by turbulent heat fluxes. The PV generated by heat fluxes remains close to the surface and ahead of the cyclone centre (shown between 10-20E, 40-50N in Fig. 3.9(a)) in simulation  $BD_{SST}$ ; i.e., it is not vented from the boundary layer. It therefore never reaches a position above the low centre and cannot prevent communication between upper- and lower-level anomalies.

Beare's (2007) conclusion that the heat-flux generated PV is not dominant in the spin-down process is therefore justified. But the results are not contradictory to those of Adamson *et al.* (2006). Indeed, simulation  $BD_m$  shows a slight filling of 2 hPa after 48 hours compared to  $BD_{SST}$ , which is consistent with the results of the PV inversion in Beare (2007) that the PV generated by the heat fluxes acts to deepen the cyclone slightly.

The low-level jet seen in the simulations of Beare (2007) is now considered. Formed by a reversal of the north-south temperature gradient generating an easterly wind shear, this cold air wraps around the cyclone centre, producing a cold conveyor belt. This provides ideal conditions for generation of large surface stress, and Becker *et al.* (1996) discussed how an enhanced low-level jet can increase the amount of boundary-layer Ekman pumping. The location of maximum surface stress is then found to have a large affect on cyclone development, consistent with the Ekman pumping mechanism. Such a low-level jet was not apparent in the LC1 life-cycle simulations of Adamson *et al.* (2006). Figure 3.10 shows the low-level winds at an early stage of development in simulations  $AD_m$  on the spherical domain (the Adamson *et al.* (2006) experiment) and  $BD_{SST}$  (the Beare (2007) experiment). If these low-level winds are assumed to lie within the surface layer, the surface stress is given by the bulk aerodynamic formula (Eqn. 2.10a). The surface stress exerted on the cyclone is therefore proportional to the square of the low-level wind. It is noticeable that the strongest wind-speeds in Fig. 3.10(b) are to the southwest of the low centre, between  $-15$  and  $-5E$ ,  $50-55N$ , whereas in Fig. 3.10(a) they are to the southeast, within the warm sector (between  $-35$  and  $-25E$ ,  $45-50N$ ). Therefore, in the Adamson *et al.* (2006) experiment, the strongest winds, and therefore surface stress, are in a region of horizontal temperature gradients and hence significant baroclinic PV generation. However, in Beare (2007) the low-level jet wrapping around the cyclone centre enhances wind-speeds to the southwest of the low, making the largest surface stress in a region of small horizontal temperature gradients and hence little PV generation.

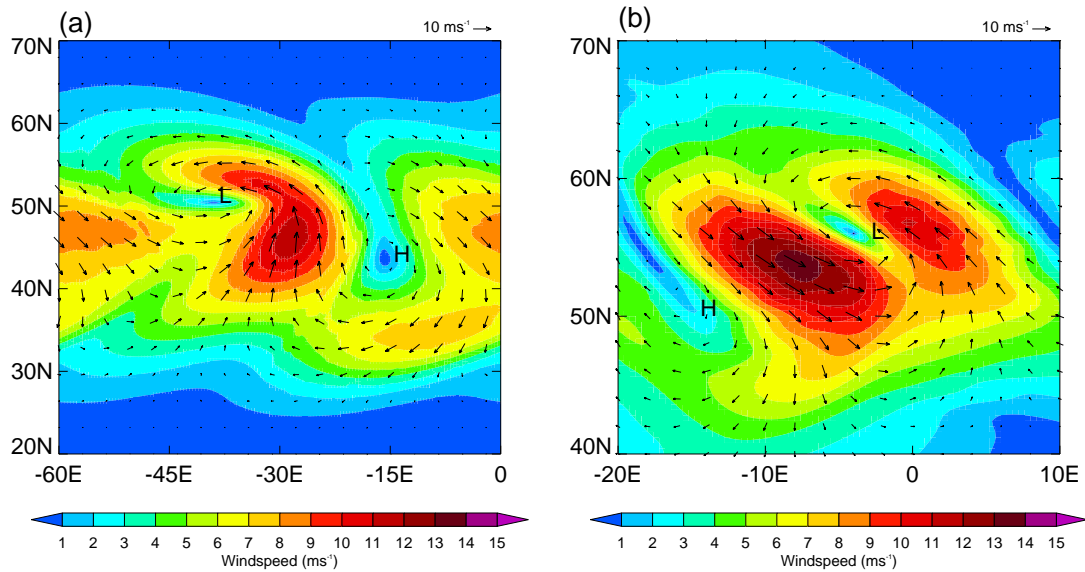


**Figure 3.10** 10 m wind vectors and windspeed (coloured) for (a) simulation  $AD_m$  on the spherical domain after 4 days and (b) simulation  $BD_{SST}$  after 24 hours, when the minimum surface pressure is approximately equal.

Simulation  $BD_{BL}$  displays features of both the Adamson *et al.* (2006) and Beare (2007) mechanisms, as shown in Figure 3.11. Figure 3.11(a) shows that simulation  $BD_{BL}$  has significant baroclinic PV generation, consistent with the mechanism of Adamson *et al.* (2006) and the results of simulations  $AD_m$  (Fig. 3.5(a)) and  $BD_m$  (Fig. 3.7(a)). Figure 3.11(b) shows the simulation also has high windspeeds, and therefore high values of surface stress, wrapping around the cyclone centre, consistent with the mechanism of Beare (2007) (Fig. 3.10(b)). The location and magnitude of the windspeed is consistent with a low-level jet generating maximum surface stress in the well-mixed boundary layer. As discussed by Plant and Belcher (2007), PV generation through the baroclinic mechanism has some reinforcement from Ekman and turbulent heat-flux generation terms (not shown). The generation shown in Figure 3.11(a) occurs between 5 and 20E, 55-65N, in a region well placed to allow ventilation from the boundary layer. Plant and Belcher (2007) discuss how this ventilation occurs by the cold-conveyor belt at early stages of the life-cycle, transitioning to ventilation by the warm-conveyor belt at later stages, as the cyclone wraps up (similar to  $AD_m$ ). Once advected out of the boundary layer, the PV appears as a static stability anomaly above the cyclone centre.

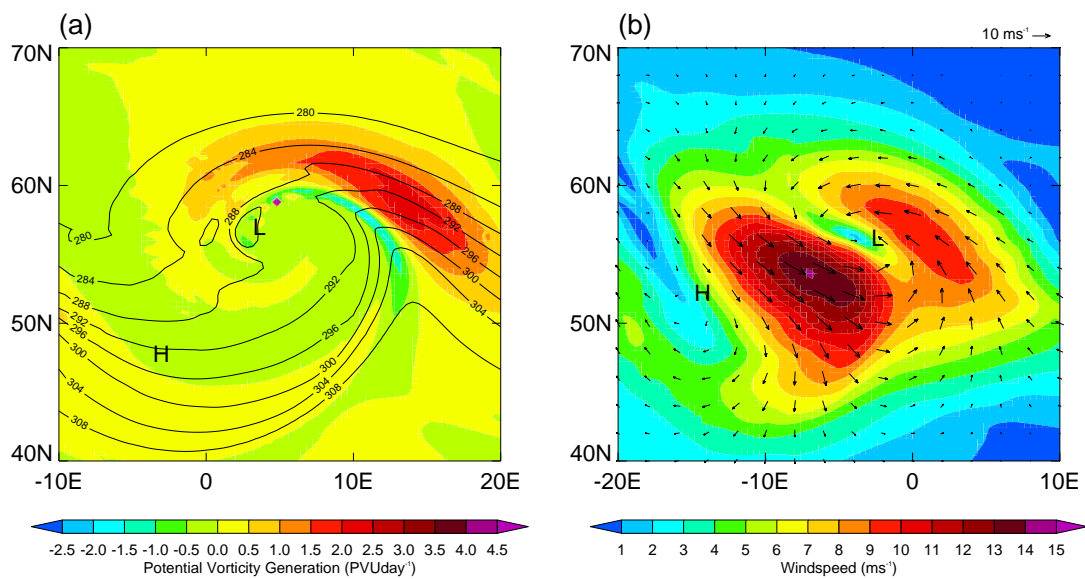


**Figure 3.11** (a) Boundary-layer depth-averaged potential vorticity generation by the baroclinic mechanism (coloured) and potential temperature at 1 km (contoured, interval 4 K) after 48 hours of simulation  $BD_{BL}$ . (b) 10 m wind vectors and windspeed (coloured) after 24 hours of simulation  $BD_{BL}$ .

Therefore, when a meridionally varying SST, such as that chosen in Chapter 2 is used, surface heat fluxes are of little importance to the development, and the spin-down is still dominated by a combination of the Ekman and baroclinic PV mechanisms. Only when a different SST, not in balance with the initial conditions, is chosen, do surface heat fluxes play an important role. For example, in simulation  $BD_{SST}$ , the surface heat fluxes act to reduce the frontal gradients, leading to less PV generation by the baroclinic mechanism and causing spin-down to occur primarily by the Ekman mechanism. Moreover, the boundary-layer PV budget is dominated by surface heat-flux generated PV, which is not well placed to be ventilated from the boundary layer, and hence is of little dynamical importance. Previous studies, such as Kuo *et al.* (1991) and Reed *et al.* (1993) have shown that surface heat fluxes can either increase or decrease a cyclone's intensity, but the general conclusion is that their effect is much smaller than that of momentum fluxes. Their results are therefore consistent with spin-down cause by the baroclinic PV mechanism, since surface heat fluxes can create both positive and negative boundary-layer PV. Depending on the precise location and sign of this heat-flux generated PV, the effect on spin-down could be positive or negative, either increasing or decreasing the effectiveness of the baroclinic PV mechanism.

### 3.4 PV INVERSION

Section 1.2.1 discussed how, given an appropriate balance condition and boundary conditions, any PV distribution can be inverted to obtain the full wind and temperature fields. Many previous studies have used PV inversion techniques to attribute aspects of the atmospheric flow to particular features in the PV field. For example, Davis and Emanuel (1991), Stoelinga (1996) and Ahmadi-Givi *et al.* (2004) (amongst many others) have used the technique of “piecewise potential vorticity inversion”. This technique defines various PV anomalies of interest within the domain and calculates their individual effect on the circulation, with the complete flow being reconstructed from a sum of the effects from all PV anomalies. Piecewise PV inversions are of particular use in mid-latitude cyclogenesis, since the evolution of the cyclone is often the result of interactions between several PV anomalies. Davis and Emanuel (1991) discuss the interaction of upper- and lower-level PV anomalies, whilst Ahmadi-Givi *et al.* (2004) investigate how a mid-level PV anomaly, formed by strong latent-heat release, can significantly effect cyclone development. Here, piecewise PV inversions of the baroclinically-generated PV anomaly will be used in an attempt to demonstrate its effect on the larger-scale flow, particularly its ability to reduce the growth rate. Sections 3.2 and 3.3 have demonstrated that the baroclinic PV mechanism can be observed in Type-A and Type-B simulations, and that the addition of surface heat fluxes has little effect if a meridional SST gradient is chosen. Therefore, for the remaining sections of this chapter, cyclone simulation  $BD_{BL}$  will be focussed on.

#### 3.4.1 INVERSION TECHNIQUE

To ascertain the effect of the baroclinically generated PV anomaly, the piecewise inversion technique of Davis and Emanuel (1991) is used. This technique is based on an approximation to the full PV field, using hydrostatic balance and given by

$$PV = \frac{gR\Pi}{pc_p} \left( (f + \nabla^2\psi) \frac{\partial^2\Phi}{\partial\Pi^2} - \frac{1}{a^2 \cos^2\phi} \frac{\partial^2\psi}{\partial\Lambda\partial\Pi} \frac{\partial^2\Phi}{\partial\Lambda\partial\Pi} - \frac{1}{a^2} \frac{\partial^2\psi}{\partial\phi\partial\Pi} \frac{\partial^2\Phi}{\partial\phi\partial\Pi} \right), \quad (3.10)$$

where  $\Phi$  is the geopotential height and  $a$  is the radius of the Earth. The inversion technique then relates the streamfunction ( $\psi$ ) and geopotential height ( $\Phi$ ) using the nonlinear balance condition

of Charney (1955), given by

$$\nabla^2\psi = \frac{1}{f} \left( \nabla^2\Phi - \nabla f \cdot \nabla\psi - \frac{2}{a^4 \cos^2\phi} \left( \frac{\partial^2\psi}{\partial\Lambda^2} \frac{\partial^2\psi}{\partial\phi^2} - \left( \frac{\partial^2\psi}{\partial\phi\partial\Lambda} \right)^2 \right) \right). \quad (3.11)$$

This balance condition assumes that the flow has no divergent component, which already raises caution about its applicability in near-surface and near-frontal regions of the cyclone, since the divergence is often strong here. The balance condition is also only applicable to frictionless flow, and hence the PV inversion must be conducted on an anomaly outside the boundary layer. These issues will be discussed further in Section 3.4.3.

The inversion technique and code was initially implemented by Ziemianski (1994), with improvements by Ahmadi-Givi *et al.* (2004) and Bracegirdle and Gray (2009), and works by completing two PV inversions. A sub-domain is defined, which contains the PV anomaly of interest, and in the first inversion, the complete PV field within this sub-domain is inverted according to Equation 3.11 to obtain the streamfunction and geopotential height fields. The code uses an iterative procedure to obtain successively better approximations to the flow, recalculating the PV from the inverted fields by Equation 3.10 and comparing this to the initial PV distribution. The inverted streamfunction and geopotential height are then modified until the final PV distribution is within a pre-defined tolerance of the initial PV distribution. The boundary conditions are chosen as “Neumann” boundary conditions, i.e. the potential temperature on the boundaries is fixed. The other common method of defining boundary conditions is the “Dirichlet” method, in which the wind (or geopotential) on the boundary is fixed. Ahmadi-Givi *et al.* (2004) discuss how in practice, the choice of boundary condition has almost no effect on the results. For the second inversion, the anomaly is defined and removed, by setting the PV to a background value within the anomaly region. Then the resultant PV field is inverted again. The flow induced by the PV anomaly is then given by the difference between the two inversion results.

### 3.4.2 INVERSION RESULTS

Figure 3.12 shows a PV cross-section through the low pressure centre at the time when the inversion was conducted. As discussed in Section 3.4.1, the balance condition is only applicable to frictionless flow, and therefore the boundary-layer must be removed from the inversion domain. Since the inversion code works on pressure levels, the boundary-layer top was defined as the

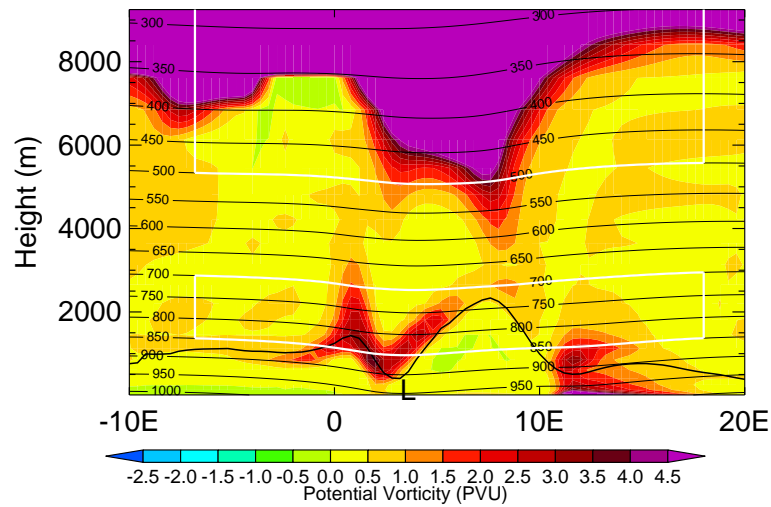


**Figure 3.12** East-west cross-section through the low centre after 48 hours of simulation  $BD_{BL}$ , showing potential vorticity (coloured) and pressure (contoured, interval 50 hPa). The solid black line represents the boundary-layer top and the white boxes outline the regions in which PV was defined as being anomalous.

900 hPa surface and represents the bottom boundary of the inversion sub-domain. Figure 3.12 shows that the boundary-layer top is very close to the 900 hPa surface across much of the domain. Only behind the cold front (between the low centre and 10E) does the boundary-layer top deviate greatly from the 900 hPa surface, extending up to 750 hPa. However, if 750 hPa was used at the boundary-layer top definition, then most of the baroclinically generated PV anomaly would also be excluded from the inversion domain.

The first inversion conducted involved defining the PV anomaly of interest as the PV sitting above the boundary-layer top above the cyclone centre. The PV anomaly was defined to exist between 850 and 700 hPa, and the lower white box shown in Figure 3.12 illustrates the region in which the PV was defined as being anomalous. As shown, this definition captures the bulk of the baroclinically-generated PV anomaly, whilst excluding any other PV. The inversion technique outlined in Section 3.4.1 was used, with the background PV obtained from a simulation of cyclone BD with no boundary-layer scheme operating ( $BD_0$ ). The results are shown in Figure 3.13. Figure 3.13(a) shows that the PV anomaly has a cyclonic circulation and a positive static stability anomaly associated with it (increased potential temperature above the anomaly implies a greater

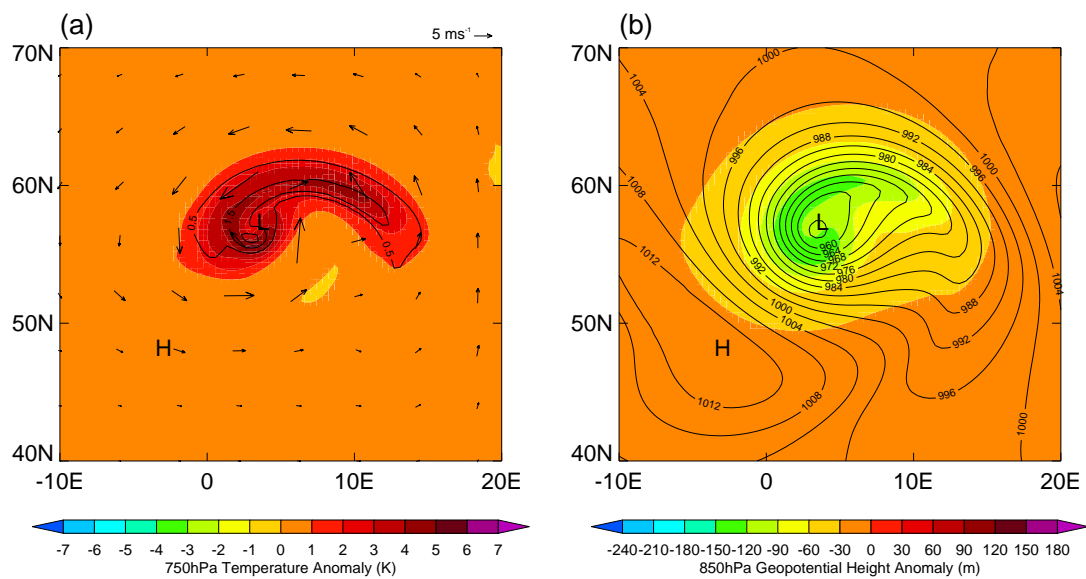


**Figure 3.13** PV inversion results for simulation  $BD_{BL}$  at 48 hours showing (a) the low-level PV anomaly at 850 hPa (black contours, interval 1 PVU), wind-field induced by the anomaly at 850 hPa (vectors) and potential temperature anomaly at 750 hPa (coloured). (b) 850 hPa geopotential height anomaly (coloured) and minimum sea-level pressure (contoured, interval 4 hPa).

vertical temperature gradient and therefore increased static stability), which are, by definition, the two effects that should combine to create a positive PV anomaly. The positive vorticity anomaly is small, with an increase in vorticity of  $\approx 30\%$  caused by the PV anomaly. Consistent with Adamson *et al.* (2006), a greater amount of the PV is partitioned into static stability, with a doubling (i.e. a 100% increase) in static stability caused by the PV anomaly. Therefore, the greater effect of the PV anomaly is the increase in static stability, which should act to reduce the cyclone growth rate. Figure 3.13(b) shows that the geopotential height anomaly associated with it is negative, i.e. that the instantaneous affect of the anomaly is to deepen the cyclone, albeit by a small amount ( $\approx 10\%$  reduction in the geopotential height field).

The inversion results are not in contradiction to the baroclinic PV mechanism however. The mechanism is concerned with the dynamical affect of the PV anomaly on the interaction between tropopause and surface anomalies, reducing their coupling. Therefore the instantaneous effect of the positive PV anomaly is expected to be a deepening, but the time-integrated effect should cause spin down. Therefore, two further PV inversions were carried out in an attempt to ascertain

the shielding influence of this low-level PV anomaly. As discussed in Section 1.2.1, the cyclone grows due to the interaction of the upper-level (tropopause) PV anomaly with the surface potential temperature distribution. The positive vorticity associated with the upper-level anomaly enhances the surface temperature wave, causing the cyclone to intensify. Therefore, by performing a PV inversion on this upper-level anomaly, its effects at the surface can be found. If the baroclinic PV mechanism is acting as expected, the influence of this upper-level anomaly at the surface should be greater if the lower-level anomaly is not present, i.e. if there is no shielding effect.

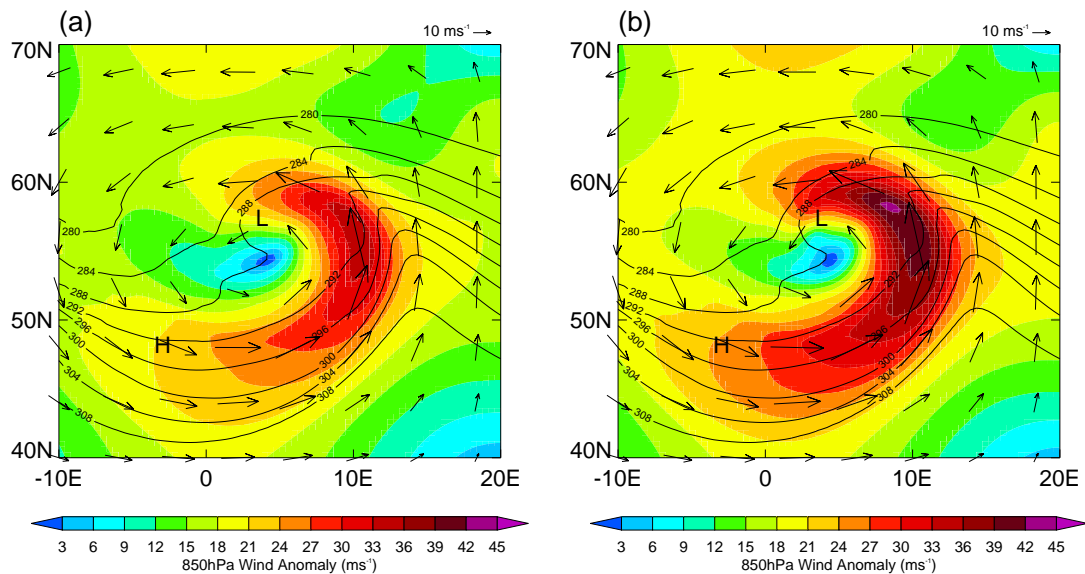


**Figure 3.14** PV inversion results for simulation  $BD_{BL}$  at 48 hours showing the flow induced by the upper-level (tropopause) PV anomaly at 850 hPa (colours and vectors) and the 900 hPa potential temperature (a) with the low-level PV anomaly present and (b) without the low-level PV anomaly present.

An upper-level anomaly was defined as the difference between the full PV field and the time-mean PV field over the cyclone life-cycle. The PV was defined as being anomalous between 500 and 200 hPa in the vertical, with the upper white box in Figure 3.12 demonstrating that the trough is located mainly within this area. Figure 3.14(a) shows the 850 hPa winds induced by the upper-level PV anomaly with the low-level anomaly present. It is clear that the winds are acting to enhance the wavelike pattern shown in the 900 hPa potential temperature. Figure 3.14(b) shows the same diagnostics when the low-level baroclinically-generated PV anomaly (lower white box in Fig. 3.12) is removed. With the low-level anomaly removed, the influence of the upper-

level feature is enhanced. This shows that without the low-level anomaly present, the upper-level feature would have a greater influence on the surface potential temperature field, eventually leading to a stronger cyclone forming.

### 3.4.3 PROBLEMS WITH PV INVERSION

Whilst suggestive of the dynamical response to the baroclinically-generated PV anomaly, the results presented above must be treated with caution. The PV inversions are being carried out very close to the boundary layer, and very close to frontal regions, both of which are typically associated with strong divergence. This means that the assumption of non-divergent flow is not a particularly good one. To demonstrate this, Figure 3.15(a) shows the difference between the

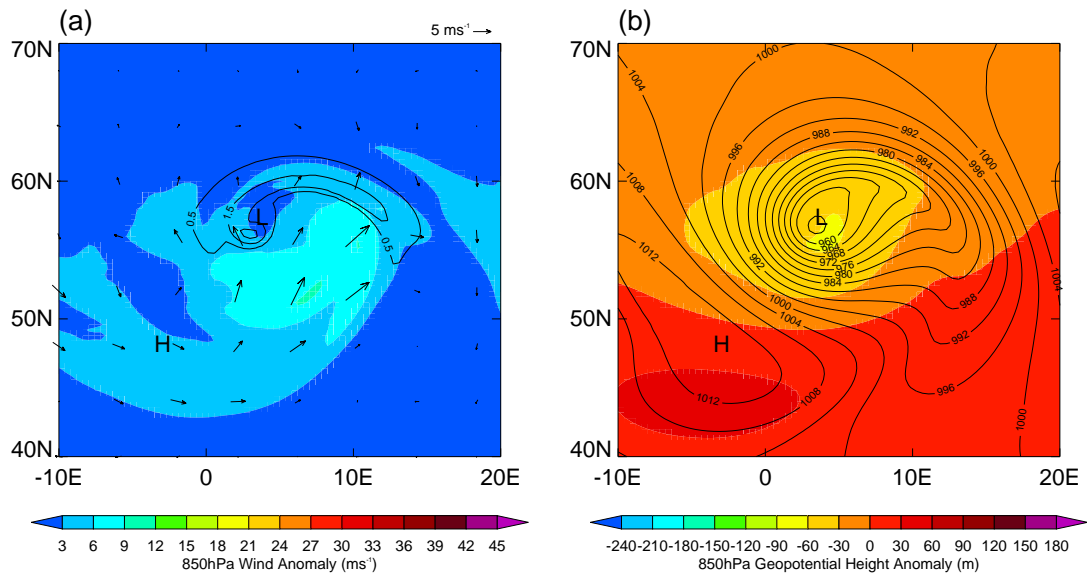


**Figure 3.15** Error in the PV inversion technique for simulation BDBL at 48 hours showing (a) the low-level PV anomaly at 850 hPa (black contours, interval 1 PVU) and divergent part of the flow at 850 hPa (colours and vectors). (b) Geopotential height anomaly associated with the divergent part of the flow (coloured) and minimum sea-level pressure (contoured, interval 4 hPa).

full wind field and the non-divergent wind field used for the PV inversion (i.e. the full wind field minus the wind field obtained from inverting the full PV field). Comparing to Figure 3.13(a) demonstrates that the signal from the PV inversion is of the same order of magnitude as the error in the inversion technique. Figure 3.15(b) shows the full geopotential height field minus

the geopotential height field obtained from inverting the full PV field, and shows that there is a difference of  $\approx 75$  m. The signal of the PV inversion shown in Figure 3.13(b) is only  $\approx 125$  m, showing that the errors associated with the PV inversion are of a similar order of magnitude to the results being obtained. There is no obvious way to rectify this, as there is presently no better way of performing a PV inversion. Nevertheless, the qualitative aspects of the PV inversions should be robust and are certainly indicative of the effect of the baroclinically-generated PV anomaly on the cyclone evolution.

## **3.5 INTERACTION BETWEEN MECHANISMS**

Sections 3.2 and 3.3 have presented results which suggest that, rather than being two competing mechanisms for cyclone spin-down, there is some interaction between Ekman pumping and the baroclinic PV mechanism. This section will therefore focus on the interaction between the two mechanisms, showing how Ekman pumping appears to support the baroclinic PV mechanism.

### **3.5.1 BOUNDARY-LAYER MODIFICATION**

Beare (2007) conducted two sensitivity experiments that involved switching off the boundary-layer parameterisation in stable or unstable boundary layers. This was achieved by determining at each timestep whether the boundary layer was stable or unstable, given by the sign of the surface buoyancy flux (Eqn. 2.22). The effect of the boundary layer was then removed by setting  $C_D$  (Eqn. 2.15),  $C_H$  (Eqn. 2.17),  $K_m$  and  $K_h$  (Eqn. 2.25) to zero. Whilst it was observed that the case with only a stable boundary layer had a greater affect on cyclone intensity, the reasons for this were not fully investigated. In simulation  $BD_{BL}$ , the differences between the case with only a stable boundary layer ( $BD_{SBL}$ ) and the case with only a convective boundary layer ( $BD_{CBL}$ ) are much smaller, indeed both changes have similar sized effects on the cyclone intensity (Figure 3.16(a)). Figure 3.16(b) shows the Ekman pumping velocity and boundary-layer depth averaged PV, along with the line separating stable and unstable boundary layers. It is noticeable that most of the boundary-layer PV (and PV generation by comparison to Figure 3.11(a)) is located within the stable boundary layer. Therefore, simulation  $BD_{CBL}$  represents effectively a no-PV mechanism

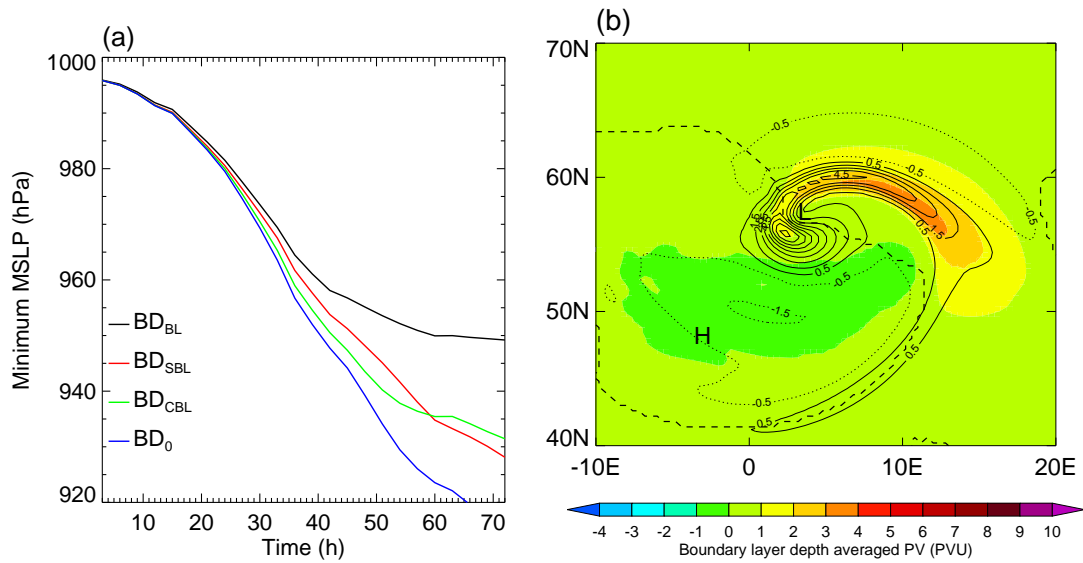


**Figure 3.16** (a) Time evolution of minimum sea-level pressure for simulation  $BD_{BL}$  (Black),  $BD_{SBL}$  (red),  $BD_{CBL}$  (green) and  $BD_0$  (blue). (b) Snapshot of simulation  $BD_{BL}$  at 48 hours showing boundary-layer depth averaged PV (coloured), Ekman pumping (black contours, interval  $1 \text{ cm s}^{-1}$ , negative values dotted) and the demarcation between stable and unstable boundary layers (dashed line).

simulation. The Ekman pumping is more complicated as it is spread across the stable and unstable boundary layers. However, the strongest Ekman pumping, located coincident with the cyclone centre, is in the convective boundary layer. This is the Ekman pumping that should be leading to vortex squashing in the interior (since this is the location of highest vorticity), and so simulation  $BD_{SBL}$  should remove this effect, leaving only weak Ekman pumping in the WCB region.

Figure 3.17 shows cross-sections through the low centre for simulations  $BD_{CBL}$  and  $BD_{SBL}$ . As expected, simulation  $BD_{CBL}$  (Fig. 3.17(a)) has no PV anomaly present above the low centre. With no friction in the stable boundary layer area, the surface stress is zero meaning that no PV generation by the baroclinic mechanism can occur there (Eqn. 3.8). There is no PV available to be ventilated on the warm-conveyor belt and a PV anomaly does not appear above the low centre. Hence for this simulation any spin-down effects must come from the Ekman pumping mechanism. There is still a peak of surface stress to the south and west of the low centre (not shown; similar to Figure 3.11(b)) and therefore an Ekman pumping velocity at the boundary-layer top above the low centre.

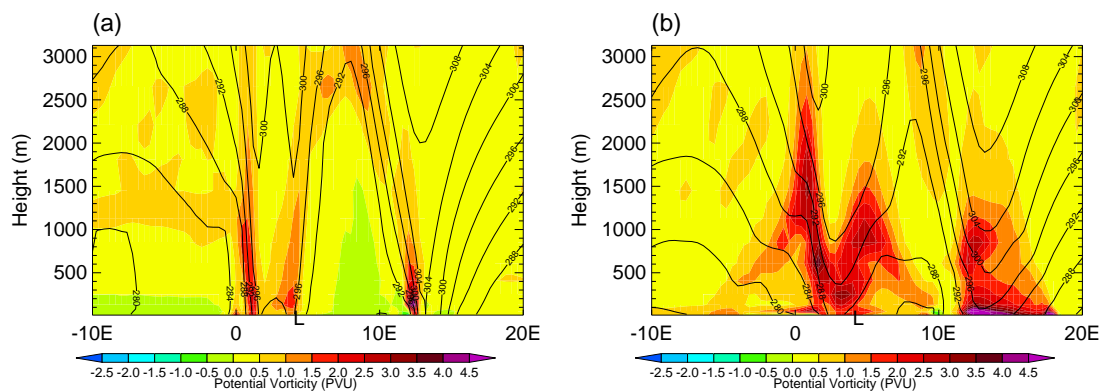


**Figure 3.17** East-west cross-section through the low centre at 48 hours showing potential vorticity (coloured) and potential temperature (contoured, interval 4 K) for (a) simulation  $BD_{CBL}$ , and (b) simulation  $BD_{SBL}$ .

By comparison, simulation  $BD_{SBL}$  (Fig 3.17(b)) does still show PV generation occurring near the cold front ( $\approx 15E$ ) and a PV anomaly located above the low centre. However, the generation does not appear as strong, nor the PV anomaly as well defined as Figure 3.7(b). Adamson *et al.* (2006) suggested that Ekman pumping in the region of the low centre helped to shape the PV anomaly in such a way that it was most associated with static stability, whilst enhancing the increased static stability by isentropic lifting within the boundary layer. This simulation, which lacks any Ekman pumping in the region of the low centre seems to support this view. The isentropes pass closer to the ground in the region of the low centre, demonstrating that they have not been lifted by the Ekman pumping. This leads to a PV anomaly which is weaker and less well-defined, with a lower static stability. Nevertheless, Figure 3.16(a) demonstrates that it is still capable of spinning down the cyclone, although not by as much as when the two mechanisms are combined.

Figure 3.16(a) also shows that the effects appear to add linearly, i.e. the sum of the spin-down created in simulations  $BD_{CBL}$  and  $BD_{SBL}$  appears to give the spin-down in simulation  $BD_{BL}$ . However, the timing of the spin-down appears different between simulations  $BD_{CBL}$  and  $BD_{SBL}$ . Simulation  $BD_{SBL}$  appears to follow the development of simulation  $BD_0$ , although with a reduced growth rate throughout the life-cycle. This is consistent with the baroclinic PV mechanism's effect on the tropospheric static stability. However, simulation  $BD_{CBL}$  appears to deepen rapidly (similar to  $BD_0$ ), and then have a sharp reduction in growth rate after 50 hours. This is consistent with

Ekman pumping becoming an important spin-down mechanism as the cyclone reaches occlusion and enters a barotropic decay phase. Simulation  $BD_{BL}$  then shows features of both, with a reduced growth rate throughout the simulation and a sharp reduction at  $\approx 45$  hours.

### 3.5.2 SURFACE ROUGHNESS EFFECTS

It was suggested in Sections 3.2.3 and 3.5.1 that there may be some interaction between the Ekman and baroclinic PV mechanisms. Section 3.2.3 showed that Ekman pumping is not just located near the cyclone centre, but also extends into the warm-conveyor belt region, assisting with the low level ascent of the WCB. Similarly, Section 3.5.1 demonstrated how Ekman pumping near the low centre assists with the shaping of the PV anomaly and maximisation of the increased static stability. Hence it seems probable that, rather than being competing mechanisms, both effects are inherent parts of the boundary-layer structure and must be thought of together.

Ekman pumping (Eqn. 3.2) is a function of surface stress only, whereas baroclinic PV generation (Eqn. 3.8) is a more complicated function of surface stress, temperature gradient and the angle between them. As discussed in Section 2.3, the surface stress is, amongst other things, a function of the roughness length ( $z_0$ ). This is the most reasonable quantity to change if we want to modify the surface stress in a realistic way, since it depends largely on the surface type rather than cyclone or boundary-layer parameters (although over a sea-surface, the Charnock relation does in fact make  $z_0$  a function of  $u_*$ ). Therefore, by systematically reducing the roughness length from its typical sea-surface value of  $\sim 10^{-4}$  m, the Ekman pumping can be reduced. However, baroclinic PV generation still remains strong, since although the surface stress decreases, the temperature gradient and angle between them remains large, allowing  $[G_B]$  (Eqn. 3.8) to remain large.

Figure 3.18 shows the results of two such experiments, reducing the roughness length of simulation  $BD_{BL}$  to a fixed value of  $10^{-8}$  m (Fig. 3.18(a)) or  $10^{-15}$  m (Fig. 3.18(b)). Both of these values are unrealistically small for any surface that is likely to be found, but serve as useful demonstrations of how removing Ekman pumping also modifies the PV structure. Comparison to Figure 3.7(b) shows that the PV anomaly is still present above the low centre, with PV generation still occurring ahead of the cold front. However, as the surface roughness is reduced, the PV anomaly gets closer to the surface. The lack of Ekman pumping means that the low level ascent

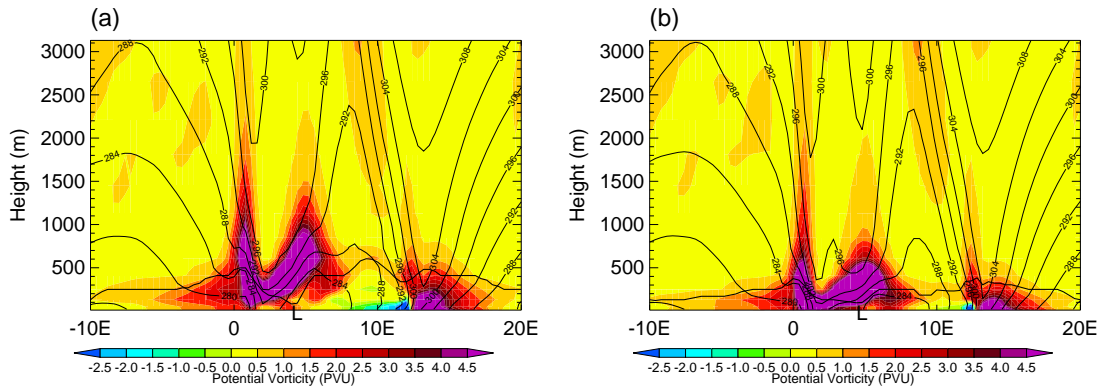


**Figure 3.18** East-west cross-section through the low centre at 48 hours of simulation  $BD_{BL}$  showing potential vorticity (coloured) and potential temperature (contoured, interval 4 K) for (a)  $z_0 = 1 \times 10^{-8}$  m and (b)  $z_0 = 1 \times 10^{-15}$  m. The thick black line denotes the boundary-layer top.

in the warm conveyor belt is reduced, leaving the baroclinically-generated PV near the surface. This is consistent with results presented by Sinclair *et al.* (2010a), who demonstrated that the ventilation of a passive tracer from the boundary layer is reduced in very low-drag simulations. The PV still accumulates in the vicinity of the low centre, but since there is no Ekman pumping to lift the PV from the surface and support it above the boundary layer, it sits as a positive PV anomaly on the surface, within the boundary layer.

This demonstrates how the mechanisms are linked. Attempting to remove the Ekman pumping mechanism has distorted the baroclinic PV mechanism. As the roughness length is reduced, the cyclone becomes stronger, tending towards the evolution without the boundary layer present. It would appear that this is partly due to the lack of Ekman pumping, but also due to the distortion of the PV anomaly and removal of the enhanced static stability above the boundary layer.

### 3.6 CONCLUSIONS

This chapter has discussed two potential mechanisms by which the boundary layer can act to reduce the intensity of mid-latitude weather systems. Through a hierarchy of theoretical and computational models, it has been shown that the traditional Ekman pumping mechanism does not

fully account for the internal dynamics of the boundary layer. Simulations of a barotropic vortex demonstrated that it would not be unrealistic to consider the affect of the boundary layer simply as an imposed “Ekman pumping” velocity beneath the vortex. It has often been assumed (e.g. Card and Barcilon, 1982; Farrell, 1985) that this approach can be used for baroclinic cyclones. However, the Eady model and more complicated numerical simulations have demonstrated that in a baroclinic cyclone, the three-dimensional structure and evolution of the boundary layer needs to be considered. This highlights the importance of representing boundary-layer processes in the most realistic manner possible. The long-tailed stability functions (Eqn. 2.27) have been shown to be unrealistic when compared to observations and large-eddy simulations (Beare *et al.*, 2006), but Beljaars and Viterbo (1998) discuss how they are required within numerical weather prediction (NWP) models to give the correct Ekman pumping within cyclones and improve skill scores. The improvements they cause are likely to be a case of compensating errors, and recently Brown *et al.* (2008) have shown improved skill scores from the use of more realistic stability functions, combined with other improvements to the boundary-layer parameterisation. It is possible that these improvements are due to a better representation of the baroclinic PV mechanism compensating for the reduced Ekman pumping.

Section 3.3 demonstrated that the surface sensible heat flux can have a large effect on the structure and evolution of the boundary layer. However, the effect on the large-scale cyclone evolution is more modest, which is in broad agreement with previous studies (e.g. Kuo *et al.*, 1991; Reed *et al.*, 1993). It was demonstrated that both the Ekman and baroclinic PV mechanisms can be seen operating within the same cyclone simulation, a fact not previously stressed by Adamson *et al.* (2006) or Beare (2007). Use of a PV inversion demonstrated qualitatively that the shielding effect is happening, but errors inherent in the inversion technique prevent these results from being anything other than indicative.

The interaction between the mechanisms was established and investigated by modifying the boundary-layer characteristics. Selectively switching off the boundary-layer parameterisation depending on stability attempted to separate the mechanisms, but instead demonstrated how the baroclinic PV mechanism is partly reliant on Ekman pumping. This was further investigated by reducing the roughness length, showing how, in the absence of Ekman pumping, baroclinically generated PV cannot be ventilated as efficiently from the boundary layer. It also does not form a

suitably shaped static-stability anomaly above the boundary-layer top, and therefore the average tropospheric static stability is not increased by any significant amount. Since there is no longer any shielding effect produced by the increased static stability, a stronger cyclone is formed.

# CHAPTER 4:

# BOUNDARY-LAYER PROCESSES IN

# MOIST LIFE CYCLES

## 4.1 INTRODUCTION

The atmospheric boundary layer is typically thought of under two broad categories: (i) a single-column boundary layer forced by the diurnal cycle over a land surface, where the growth and characteristics are determined by the surface energy balance; and, (ii) a two-dimensional internal boundary layer, growing downwind of a change in surface characteristics (e.g. a rural to urban boundary). However, synoptic-scale atmospheric phenomena also control the structure of the boundary layer in complex, three-dimensional ways. This has been highlighted recently by Sinclair *et al.* (2010b) through idealised, dry, simulations of mid-latitude cyclone waves. Strong surface heat fluxes can result from the large-scale thermal advection of heat within such synoptic systems, driving the boundary-layer structure. This produces large areas that are consistent with classical stable and unstable boundary-layer regimes, but which undergo transitions as the system evolves. Sinclair *et al.*'s (2010b) results provide a simple conceptual model of dry boundary-layer structure on synoptic scales, but raise the question how their results can be extended in the presence of a moist atmosphere.

Previous studies of boundary layers under synoptic systems have tended to be observationally based. The Joint Air-Sea Interaction Project (JASIN) was designed to observe the physical processes causing mixing in oceanic and marine boundary layers, and quantify aspects of the heat and momentum budgets in mid-latitude regions. Businger and Charnock (1983) discussed the large-scale boundary-layer structure, commenting how the observed cloud layer, typically containing cumulus and stratocumulus, was “apparently maintained by processes occurring on scales greater than 50 km” (Businger and Charnock, 1983, p. 446). They also noted that subtle differ-

ences in the boundary-layer structure can lead to large differences in the formation and dissipation of clouds, demonstrating how processes acting over a wide range of spatial and temporal scales are responsible for the observed boundary-layer structure and evolution.

Other observational studies have tended to focus in detail on one aspect of the interaction between the boundary layer and synoptic scale. Taylor and Guymer (1983) provided a detailed description of the interaction of a warm front with the boundary layer, whilst a similar perspective on the boundary-layer structure near a cold front is provided by Berger and Friehe (1995). The latter study formed part of the Experiment on Rapidly Intensifying Cyclones over the Atlantic (ERICA), for which Neiman *et al.* (1990) also provide a detailed description of surface sensible and latent heat fluxes under a rapidly-intensifying cyclone, along with the effect of these fluxes on the cyclone's evolution.

The problem with observational studies is that most cyclogenesis events occur over the open ocean, where even during intensive observational campaigns, the coverage and the horizontal and vertical resolution of data can be low, meaning that the larger-scale structures are not well observed. Therefore a computational modelling approach has been used (e.g. Kuo *et al.*, 1991; Levy, 1989) to ascertain the detailed cyclone–boundary-layer interaction. However, initial condition and model uncertainty can lead to differing results from modelling studies, even when simulating the same cyclone. Therefore, an idealised modelling approach such as that taken by Nuss (1989) and Becker *et al.* (1996) is chosen. This allows the boundary-layer response to a generic and well-defined large-scale perturbation to be investigated, as well as any feedback processes involved, without more complex atmospheric flows distorting the synoptic-scale evolution.

Idealised cyclone-wave life cycles (e.g. Thorncroft *et al.*, 1993) have been used to study the structure, evolution and energetics of cyclone-anticyclone systems and their role in the poleward transport of heat and momentum. However, due to the need for accurate parameterisations of convection, cloud microphysics and precipitation, studies of moist cyclone-wave life cycles are relatively few in number. Gutowski *et al.* (1992) and Pavan *et al.* (1999) describe large-scale features, energetics and moisture transport in cyclone waves with relatively simple moisture parameterisations. Furthermore, since they focus on the large-scale development, they only include a single-layer parameterisation of surface drag and heat/moisture exchange, and this is done for completeness rather than to study the boundary layer. Gutowski and Jiang (1998) use improved

parameterisations to study the effects of surface fluxes on the interaction between shallow cumulus and cyclone waves. Their results demonstrate how cyclone waves are important in redistributing moisture within the free troposphere, but do not fully investigate how crucial the boundary layer is in this process. Field and Wood (2007) used a composite of satellite-observed cyclones to demonstrate a strong correlation between moisture convergence in the boundary layer and cyclone rainfall rate, but what are the physical processes occurring in the boundary layer that form and maintain this moisture source?

This chapter investigates the synoptic-scale boundary layer in idealised cyclone-wave simulations with almost full physics (simulation  $AM_{BL}$ ). The aim of the work is to determine the structure of the boundary layer under a developing cyclone wave and how the boundary layer evolves to this state during a cyclogenesis event. How the presence of moisture modifies conceptual models of dry boundary-layer structure is investigated, and a conceptual model of boundary-layer moisture regimes is developed. A quantitative assessment of the role of the synoptic boundary layer in redistributing moisture in the horizontal and venting it into the free troposphere is made. In Section 4.2 the structure and evolution of the boundary layer is discussed in a qualitative manner, considering how moisture regimes can be classified in Section 4.3. Finally, a quantitative description is added with budgeting techniques in Section 4.4 and the moisture cycle in a cyclone-wave is discussed in Section 4.5.

## 4.2 BOUNDARY-LAYER STRUCTURE

The structure and evolution of the boundary layer under cyclone simulation  $AM_{BL}$  (Section 2.5.2) will now be discussed, demonstrating how large-scale processes form and maintain the appearance of the boundary layer as the cyclone wave intensifies.

### 4.2.1 SURFACE FLUXES

Surface fluxes of heat and moisture are calculated in the model by bulk relations, given in Equations 2.10b and 2.10c. The surface fluxes are shown in Figure 4.1 after 7 days and show broadly similar patterns. Within the warm-conveyor belt region there are negative fluxes of both sensible

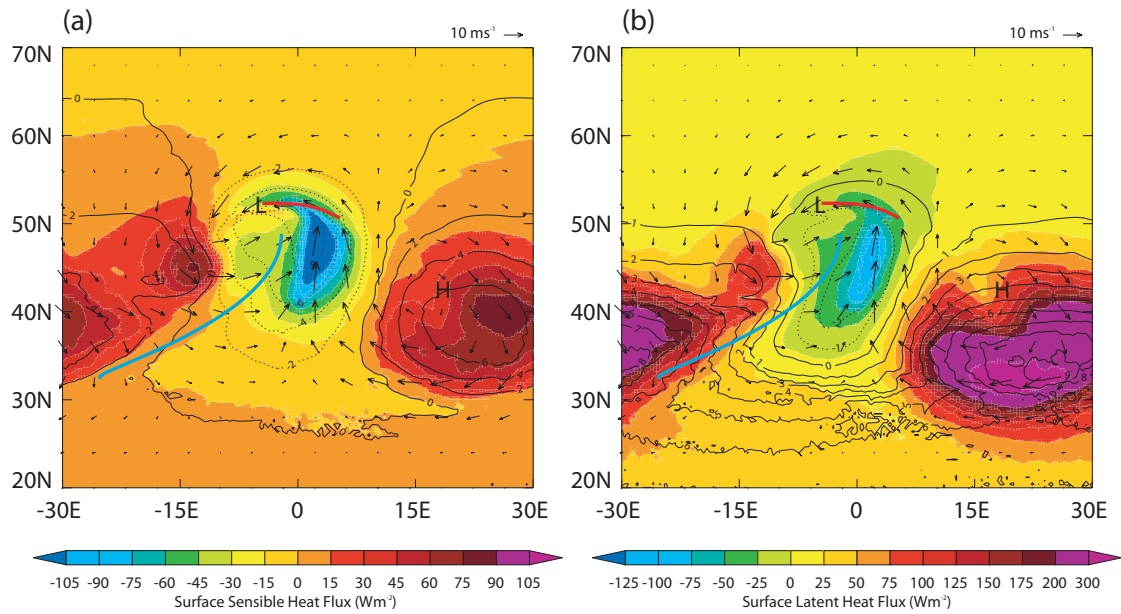


**Figure 4.1** Surface fluxes at day 7 showing (a) sensible heat (coloured) with  $\theta_s - \theta_1$  (contoured, interval 2 K, negative values dotted), and (b) latent heat (coloured) with  $q_{\text{sat}}(\theta_s) - q_1$  (contoured, interval 1  $\text{gkg}^{-1}$ , negative values dotted). Wind vectors for every tenth gridpoint at the lowest model level (10 m) are over-plotted on both panels. The L and H are added to mark the low and high pressure centres.

and latent heat: warm, moist air moves over the cooler sea-surface, losing heat and becoming super-saturated with respect to the surface, forcing the moisture to condense out in a similar manner to dew formation over land.

The main regions of positive heat fluxes are behind the cold front, extending into the high pressure part of the wave. It is noticeable that the maximum values for sensible and latent heat are not coincident. The greatest sensible heat-flux can be seen to the east of the high centre, where there is the greatest thermal advection of cold air over the warm sea-surface, giving the greatest contrast in temperature. However, the latent heat-flux is greatest where the greatest saturation deficit occurs, which is to the south of the high centre, because the air and sea-surface temperatures (SST) are both higher here, and hence the saturation vapour pressure is larger. The pattern of sensible heat-flux is similar to that in Sinclair *et al.* (2010b) for dry cyclone-wave simulations, and to that in Brown *et al.* (2008) for a real case-study. The main difference from Sinclair *et al.* (2010b) occurs in the secondary maximum of sensible (and latent) heat to the south-west of the

low centre (−15E, 45N). This is due to a low-level jet which wraps around the cyclone centre, generating stronger wind speeds in this location. Coupled with the stronger advection of cold (dry) air over a higher SST, this gives rise to the secondary maximum. This feature is caused by a combination of differences in the cyclone dynamics and the large-scale effect of moisture intensifying the system. The range of values of surface fluxes in the simulation are similar to those reported in observational studies (e.g. Neiman *et al.*, 1990; Kuo *et al.*, 1991), and previous idealised studies (e.g. Nuss, 1989).

Within the surface layer, the stress is given by the bulk aerodynamic formula, and its distribution and magnitude can be most easily seen in terms of the friction velocity

$$u_* = \left( \frac{|\tau|}{\rho} \right)^{1/2} = C_D^{1/2} |\mathbf{v}_1|. \quad (4.1)$$

The friction velocity is shown in Figure 4.2(a) and shows two distinct regions of enhanced momentum transfer. The first is in the WCB region, coincident with the negative scalar fluxes, whilst the second is in the region of the low-level jet, coincident with the secondary maxima of the scalar fluxes. Section 3.3 discussed how momentum transfer in these two regions can affect the large-scale development of the cyclone. There is also enhanced momentum transfer to the east and south of the anticyclone associated with air circulating around the high pressure system.

#### 4.2.2 BOUNDARY-LAYER STRUCTURE

The bulk stability of the boundary layer is often considered in terms of the dimensionless quantity  $-h/L$ . This stability measure is shown in Figure 4.2(b), indicating that the boundary layer is only weakly stable in the warm-conveyor belt region, with  $-h/L$  values between  $-5$  and  $-10$ . This explains the large values of scalar and momentum fluxes in this region: although the boundary layer is stable, there is still significant turbulent mixing allowing large surface-flux exchanges. Within the high pressure region, the boundary layer is most unstable in the region of highest pressure, but, as in Sinclair *et al.* (2010b), this is not coincident with the largest surface fluxes due to the very low wind speeds here. To the very south of the domain, the boundary layer is very unstable, due to the high moisture content and high SSTs at this latitude, and conversely to the very north of the domain the boundary layer is very stable, due to the low moisture content and low SSTs.

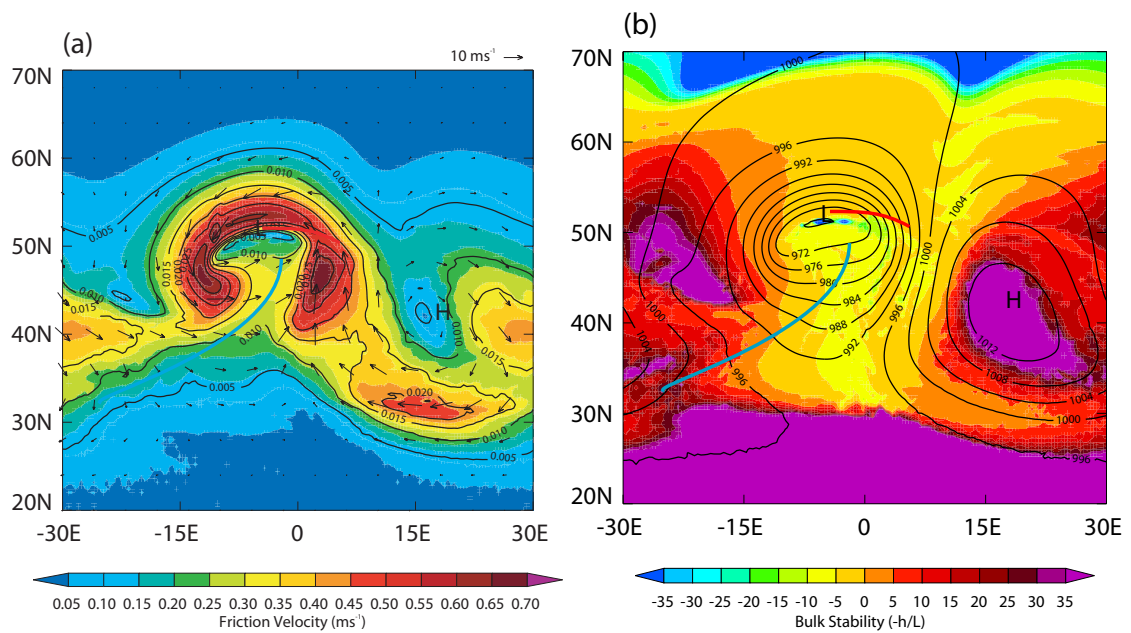


**Figure 4.2** (a) Friction velocity (coloured) with  $C_D$  (contoured, interval 0.005) and wind vectors every tenth gridpoint at the lowest model level over-plotted. (b) Bulk stability ( $-h/L$ , coloured) with pressure at mean sea-level (contoured, interval 4 hPa), at day 7.

Figure 4.2(b) showed how the boundary-layer stability, driven mainly by the surface buoyancy flux, can be broadly characterised as being stable within the cyclonic region and unstable within the anticyclonic region. However, in a simulation with moisture, the presence of cloud has a significant effect on the boundary-layer structure and evolution.

Classical types of boundary-layer development can be observed within different areas of the system, although the forcing is through large-scale thermal advection in this case, rather than through diurnal heating and cooling. In regions of positive surface fluxes, a convective boundary layer grows as the wave intensifies. Initially, a single mixed layer is formed, with capping cloud created when this mixed layer grows higher than the lifting condensation level. By day 4 this stratocumulus becomes decoupled from the surface in some places and shallow cumulus convection may be initiated beneath it. By day 7 the shallow convection has become strong enough in some places to produce a cumulus-capped layer extending up to  $\approx 3$  km. Figure 4.3(a) shows a vertical profile through such a boundary layer at this stage of evolution. There is a moist, well-mixed layer extending up to  $\approx 1$  km, over which the turbulent moisture flux ( $E = \rho \overline{w'q'}$ ) decreases from its surface value down to zero at the cloud base. Above this the atmosphere is conditionally unstable

and moist convection acts to mix the moisture profile throughout the cloud depth. The liquid water content of the shallow cumulus is also shown in the figure.

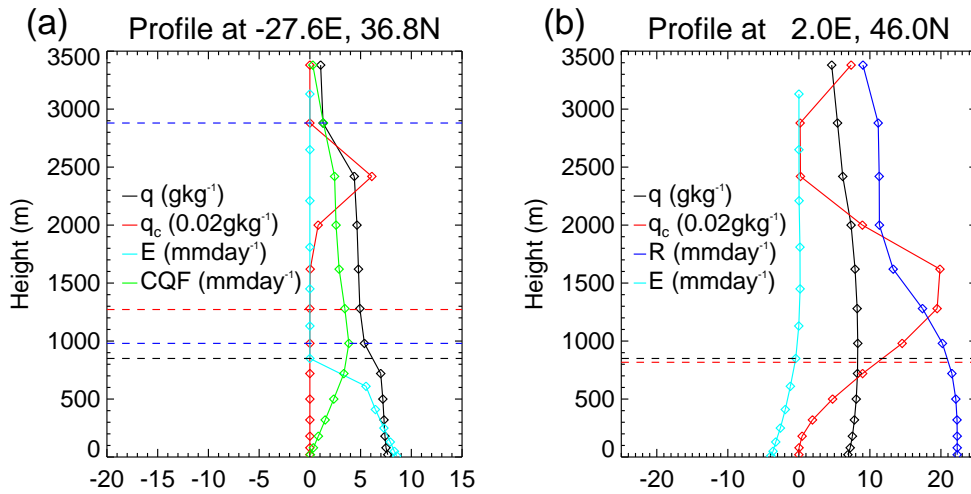


**Figure 4.3** Profiles of specific humidity ( $q$ ), cloud water content ( $q_c$ ), turbulent moisture flux ( $E$ ), convective moisture flux ( $CQF$ ) and precipitation rate ( $R$ ) at day 7, for: (a) the cumulus-capped post-frontal boundary layer; and, (b) the stable WCB boundary layer. The abscissa units for each profile are shown on the panels. The horizontal black dashed lines denote the MetUM diagnosed boundary-layer top ( $z_h$ ), while blue dashed lines denote the extent of convective cloud and red dashed lines denote the boundary-layer depth ( $h$ ) as diagnosed using the method in Section 2.3.4.

Within the warm-conveyor belt region, the boundary layer shows some of the classical features of a nocturnal boundary layer. Dew formation on the surface has already been mentioned in Section 4.2.1, but above the surface, the air becomes super-saturated and moisture is forced to condense out as low-level cloud or fog. The boundary-layer structure here is complicated by large-scale processes which are acting in the lower troposphere. The large-scale ascent on the warm-conveyor belt and associated cloud and precipitation, in addition to strong wind-shear, all contribute to a large amount of mixing within a boundary layer that would be considered stable on buoyancy grounds. Figure 4.3(b) shows a vertical profile through this warm-conveyor belt region. The humidity profile remains well-mixed throughout a large layer of the atmosphere since moisture is being lost to the surface, but also mixed upwards within the cloud layer. Section 4.4.2 will discuss how large-scale advection is having an effect on the boundary-layer moisture distribution at this point. There are two distinct layers of cloud visible, one well above the boundary layer

on the conveyor belt ( $> 3$  km high) and another within the boundary layer ( $\approx 500 - 2500$  m). The upper layer of cloud is precipitating, and this precipitation is enhanced by the lower layer of cloud.

It is also worth noting that the cyclone wave is constantly propagating eastwards, and so at any fixed point in space, the boundary layer will be transitioning between these stable and unstable regimes on a timescale of 3 – 4 days.

### 4.3 MOISTURE REGIMES

Thus far, boundary-layer regimes have only been considered in terms of stable or unstable boundary layers forced by the surface sensible heat-flux. Whilst this classification is undoubtedly useful, it does not provide any information about the boundary-layer moisture structure. Mahrt (1991) attempted to classify regimes dependent on their stability and moisture availability, using bulk stability ( $-h/L$ ) and Bowen ratio ( $H_s/\lambda E_s$ ). The phase space of bulk stability and Bowen ratio is plotted in Figure 4.4(a) for the 30 – 60N latitude range. The figure shows three distinct regions of interest. Quadrant 1 is a region of positive buoyancy with low Bowen ratio. This signifies a convective boundary layer where the latent heat-flux exceeds the sensible heat-flux, and corresponds to an area behind the cold front extending into the high-pressure. Moisture is freely available from the sea-surface and the thermal advection of relatively cold air controls the stability. Within calm regions, near the high centre, buoyancy dominates the turbulence, whilst in windy regions to the east of the high-centre there is also shear-generated turbulence.

Quadrant 2 corresponds to a weakly stable boundary layer with large Bowen ratio. Both the sensible and latent heat fluxes are negative, and this corresponds to the warm-conveyor belt area to the south-east of the low centre. As warm, moist air moves polewards over a colder sea-surface, fluxes act to reduce both the heat and moisture content. The latent heat-flux is limited since dew-formation is only one of three possible processes that remove moisture from this air. As discussed in Section 4.2.2, the moisture can also condense out within the air to form low-level cloud or fog, whilst the large-scale ascent on the warm-conveyor belt can also ventilate moisture from the boundary layer into the troposphere. In contrast, the sensible heat-flux can grow very large because the loss of heat to the surface is the only way to cool the air. This gives rise to the

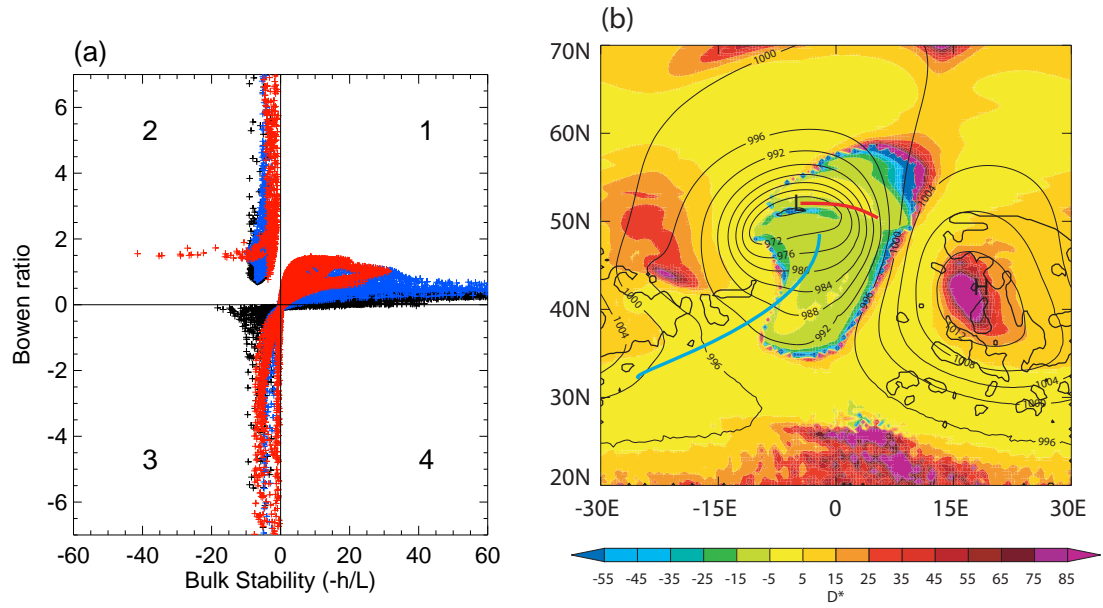


**Figure 4.4** (a) Bowen ratio and bulk stability phase space for the 30 – 60N latitude band (black, 30 – 40N; blue, 40 – 50N; red, 50 – 60N). The quadrants are labelled for ease of reference within the main text. (b)  $D^* = (-h/L)(H_s/\lambda E_s)$  (coloured) with mean sea-level pressure (thin contours, interval 4 hPa) at day 7. Regions of cumulus-capped boundary layers are also marked, by thick lines.

large Bowen ratios observed in this regime.

The third region, in Quadrant 3, consists of a weakly stable boundary layer with negative Bowen ratio, implying a positive latent heat-flux. This region represents a transitional regime between the two extreme cases discussed above. Figure 4.1 shows the relevant areas within the wave, where the boundary layer is only weakly stable on buoyancy grounds, but shear-induced turbulence from the low-level winds is sufficient to cause evaporation into the unsaturated boundary layer. In some places, values of both  $H_s$  and  $\lambda E_s$  are small however, which can result in some large values of Bowen ratio where  $\lambda E_s$  approaches zero more rapidly than  $H_s$ .

Mahrt (1991) considered two prototype moisture regimes: a boundary layer drying by entrainment from above, or one moistening due to surface fluxes. These were characterised in terms of the nondimensional quantity  $D^*$ , defined as

$$D^* = \left( -\frac{h}{L} \right) \frac{H_s}{\lambda E_s}. \quad (4.2)$$

Figure 4.4(b) shows this quantity at day 7 in the life cycle.  $D^*$  is largest when  $-h/L$  is large and  $E_s$  is small, which corresponds to a convective boundary layer with little surface moisture flux. Under these conditions, the boundary layer is characterised by large eddies, which will contribute to significant entrainment of drier air from above, hence characterising the entrainment drying regime. Conversely,  $D^*$  is small and positive when  $-h/L$  is small and  $E_s$  is large, corresponding to a weakly convective or shear-driven boundary layer with large surface evaporation. Here, the boundary layer is moistening from below with little entrainment of drier air from above. Both these regimes can be seen in the post frontal and anticyclonic areas of the wave, with large  $D^*$  coincident with the high-centre and small  $D^*$  to the east of this. It is also noticeable that small values of  $D^*$  match regions of cumulus convection, whereas large values of  $D^*$  are coincident with areas of a single mixed layer, consistent with the notion that entrainment drying of the boundary layer is inhibiting shallow convection and cloud formation.

The results presented here show that a third moisture regime is also required in this classification scheme, one defined by negative values of  $D^*$  and characterised by a stable boundary layer losing moisture to the surface via condensation. However, complex synoptic-scale airflows within this area of the cyclone wave could result in the boundary layer as a whole either drying or moistening, depending on the composition of the air converging into it. For this reason, a budgeting technique is applied in the next section to unravel the effects of the relevant airflows.

## 4.4 BOUNDARY-LAYER BUDGETS

### 4.4.1 DERIVATION OF MOISTURE BUDGET

To determine the redistribution of moisture by the cyclone wave, the boundary-layer budgeting techniques used by Sinclair *et al.* (2010b) are followed, only instead of the total mass content of the boundary layer, the total moisture content is of interest:

$$\int_A \int_0^h \rho q dz dA, \quad (4.3)$$

where  $q = q_v + q_l + q_f$ . Reynolds averaging Equation 2.5 gives rise to the moisture equation

$$\frac{\partial}{\partial t}(\rho q) + \nabla \cdot (\rho q \mathbf{u}) = -\frac{\partial}{\partial z}(\rho \overline{w'q'}) + s, \quad (4.4)$$

where  $S$  is a source or sink term from processes other than boundary-layer turbulence. The evolution of total moisture is obtained from a volume-integral of Equation 4.4. The first term from the left-hand side of Equation 4.4 can be simplified using the Leibniz-rule:

$$\int_A \int_0^h \frac{\partial}{\partial t} (\rho q) dz dA = \int_A \left[ \frac{\partial}{\partial t} \left( \int_0^h \rho q dz \right) - (\rho q)_h \frac{\partial h}{\partial t} \right] dA. \quad (4.5)$$

The second term from the left-hand side of Equation 4.4 requires the use of the divergence theorem:

$$\int_A \int_0^h \nabla \cdot (\rho q \mathbf{u}) dz dA = \int_S \rho q \mathbf{u} \cdot \mathbf{n} dS, \quad (4.6)$$

where  $S$  is the surface enclosing the boundary-layer control volume and  $\mathbf{n}$  is the unit normal to this. Since the equation is already Reynolds averaged, there is no mean flow through the bottom surface and the surface integral can be separated into contributions from the sides ( $B \times h$ , where  $B$  is the boundary to  $A$ ) and top ( $T$ ) of the control volume:

$$\int_S \rho q \mathbf{u} \cdot \mathbf{n} dS = \int_B \int_0^h \rho q \mathbf{v} \cdot \mathbf{n} dz dB + \int_T (\rho q)_h \mathbf{u} \cdot \mathbf{n} dT. \quad (4.7)$$

Since the boundary-layer top can slope in  $x$  and  $y$ , the area element  $dT \neq dA$ , but rather they are related by

$$dT = \sqrt{1 + \left( \frac{\partial h}{\partial x} \right)^2 + \left( \frac{\partial h}{\partial y} \right)^2} dA. \quad (4.8)$$

Using this relation and the divergence theorem in two dimensions gives

$$\int_A \int_0^h \nabla \cdot (\rho q \mathbf{u}) dz dA = \int_A \left[ \nabla_2 \cdot \left( \int_0^h \rho q \mathbf{v} dz \right) + (\rho q)_h \mathbf{u} \cdot \tilde{\mathbf{n}} \right] dA, \quad (4.9)$$

where  $\tilde{\mathbf{n}} = \mathbf{n} \sqrt{1 + \left( \frac{\partial h}{\partial x} \right)^2 + \left( \frac{\partial h}{\partial y} \right)^2}$ . Finally, the terms on the right-hand side of Equation 4.4 are volume-integrated thus:

$$\int_A \int_0^h \left[ -\frac{\partial}{\partial z} (\overline{\rho w' q'}) + S \right] dz dA = \int_A \left[ -(\overline{\rho w' q'})_h + (\overline{\rho w' q'})_0 + \int_0^h S dz \right] dA. \quad (4.10)$$

Combining Equations 4.5, 4.9 and 4.10 and dropping the integration over the arbitrary area  $A$ , the moisture budget equation is obtained:

$$\frac{\partial}{\partial t} \widehat{\rho q} = \underbrace{(\rho q)_h \frac{\partial h}{\partial t}}_1 - \underbrace{(\rho q)_h \mathbf{u} \cdot \tilde{\mathbf{n}}}_2 - \underbrace{\nabla_2 \cdot \widehat{\rho q \mathbf{v}}}_3 - \underbrace{(\overline{\rho w' q'})_h + (\overline{\rho w' q'})_0}_4 + \underbrace{\widehat{S}}_5, \quad (4.11)$$

where  $\widehat{\chi} = \int_0^h \chi dz$ . The subscript  $h$  denotes a quantity evaluated at the boundary-layer top, or if there is a sharp inversion present, just below the inversion, since the entrainment flux is contained in term 4. Written in this form, term 1 represents the local change in boundary-layer depth,

term 2 represents advection across the boundary-layer top, term 3 horizontal divergence within the boundary layer, term 4 the net vertical transport by boundary-layer turbulence and term 5 the net precipitation falling through the boundary layer. A caveat follows to this: shallow cumulus convection is also capable of moving moisture across the boundary-layer top, and if the model were fully convection resolving, then such transport would be included within term 2. However, shallow cumulus is parameterised within the model, separately from the boundary-layer parameterisation. Thus, there is an additional contribution to transport across the boundary-layer top, which will be considered separately and denoted as  $(\rho q w)_{\text{conv}}$ .

#### **4.4.2 APPLICATION OF MOISTURE BUDGET**

Numerical evaluation of the individual terms in Equation 4.11 produces a budget which is well-balanced. It also demonstrates that there is a negligible contribution from the fifth term,  $\widehat{S}$ , since the precipitation is generally falling from above the boundary layer straight through to the surface, with little evaporation into the moist air beneath the warm-conveyor belt. There is also a negligible contribution from the entrainment flux,  $\overline{w'q'_h}$ , since entrainment is typically of drier air which does not affect the total moisture content. At any fixed point in space, the overall rate of change of total moisture (left-hand side of Equation 4.11) is strongly linked to the rate of change of  $h$  (term 1), due to the eastwards progression of the cyclone wave forcing the transitioning boundary-layer structures discussed in Section 4.2. This is shown in Figure 4.5, and shows that moisture is gained as the boundary layer grows with the passage of the cold front, and is lost as the boundary layer shrinks with the approach of the stable WCB region.. The other terms in the budget (2, 3, 4 and  $(\rho q w)_{\text{conv}}$ ) provide insight into the system-relative moisture flows and low-level water cycle, and these are shown in Figure 4.6.

As moisture is evaporated from the sea-surface behind the cold front and in the high pressure regions (Figure 4.6(c)), horizontal divergence forced by boundary-layer drag transports moisture within the boundary layer away from this region. This maintains the saturation deficit, allowing strong evaporation to be maintained. This is a continual process occurring throughout the life cycle, ensuring that regions of positive latent heat-flux never become saturated and regions of frictional divergence never dry out.

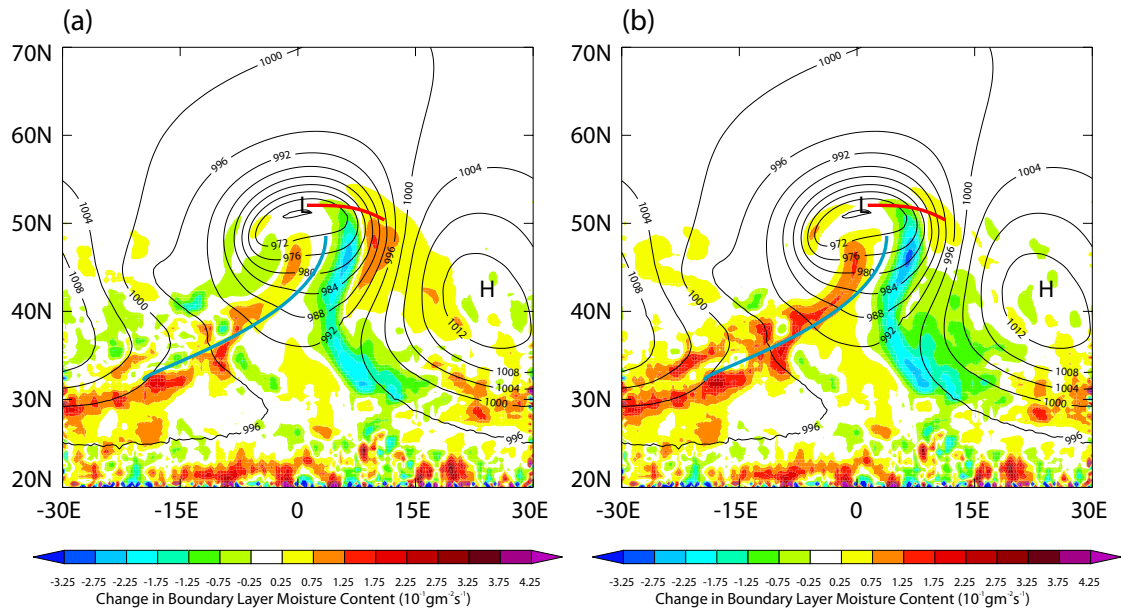


**Figure 4.5** (a) Rate of change of total moisture in the boundary layer (left-hand side of Equation 4.11 and (b) tendency in boundary-layer moisture content due to the change in boundary-layer depth (term 1), both at day 7 (coloured). The pressure at mean sea-level is overplotted (contoured, interval 4 hPa).

Since the divergence term (Figure 4.6(b)) cannot produce net moisture transport out of the boundary layer, this moisture must converge elsewhere in the cyclone-wave boundary layer. The convergence, forced by surface drag and large-scale ageostrophic flow, occurs in the footprint of the warm-conveyor belt. This leads to a large build-up of moisture in the WCB region, resulting in the saturated boundary layer discussed in Section 4.2. Some moisture is returned to the surface via latent heat exchange, but the majority of this moisture is loaded onto the warm-conveyor belt and ventilated from the boundary layer by the large-scale ascent (Figure 4.6(a)).

Warm-conveyor belts are almost 100% efficient at converting moisture into precipitation (Eckhardt *et al.*, 2004), and hence most of this moisture loaded onto the WCB will ultimately return to the surface as precipitation. This completes a cycle of moisture transport from the surface to the troposphere and back, forced by the cyclone wave and mediated by the boundary-layer dynamics. However, it is noticeable from Figures 2.12(a) and 4.1(b) that the surface precipitation from the WCB is in a very different location to the surface evaporation, showing how the cyclone wave and boundary layer act together to transport moisture large distances, both in the east-west and

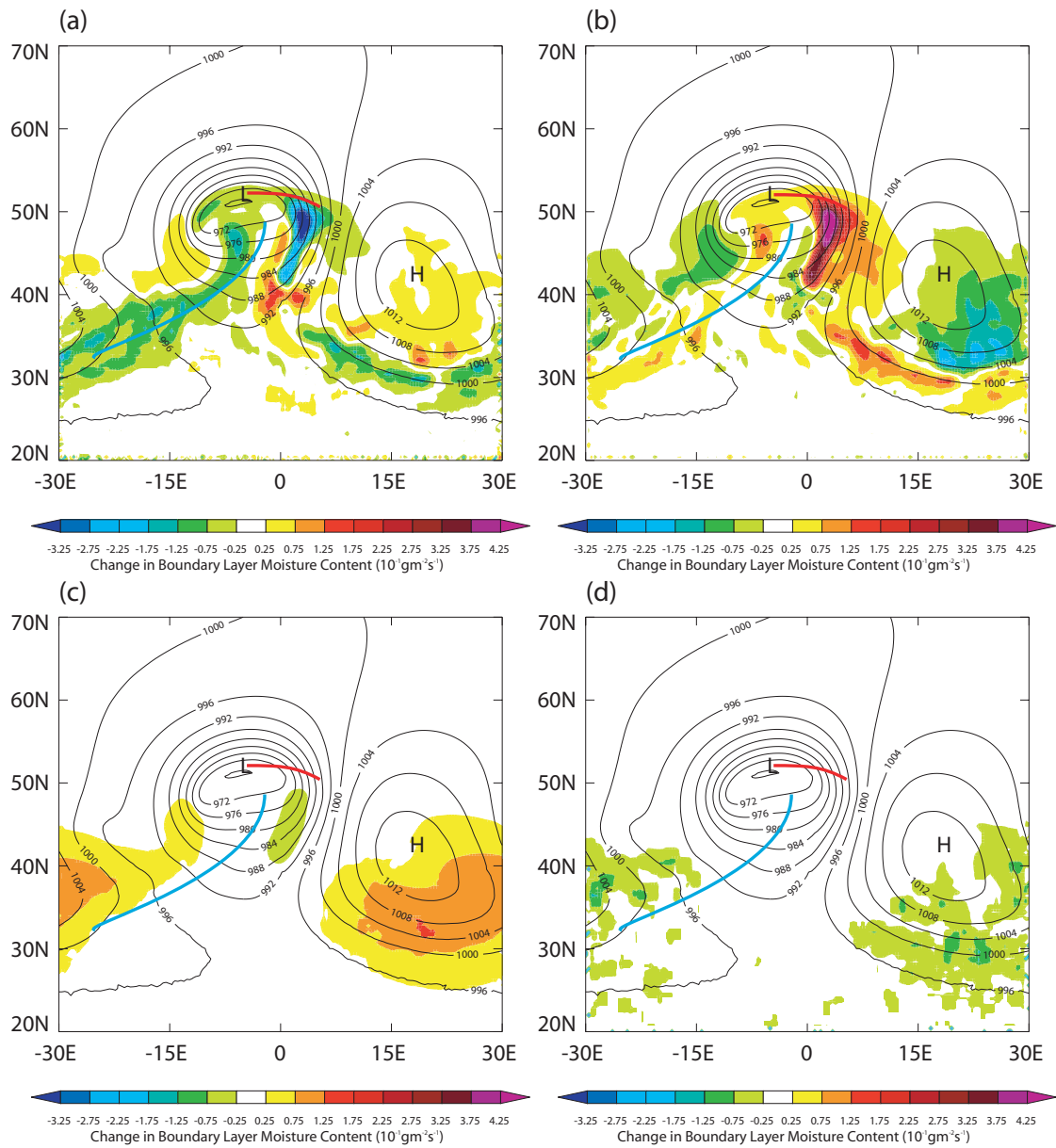


**Figure 4.6** Tendencies in boundary-layer moisture content (coloured) at day 7 due to various terms in the budget (Equation 4.11). (a) advection across the boundary-layer top (term 2); (b) horizontal divergence within the boundary layer (term 3); (c) net vertical transport by boundary-layer turbulence (term 4); and, (d) transport by shallow convection ( $(\rho q w)_{\text{conv}}$ ). The pressure at mean sea-level is overplotted (contoured, interval 4 hPa).

north-south directions.

Within the anticyclonic region, large-scale subsidence moves some moisture from the free troposphere into the boundary layer. However, this term (Figure 4.6(a)) is small compared to the evaporation term (Figure 4.6(c)), which leads to a major difference between the moisture budget and the mass budget, which was considered by Sinclair *et al.* (2010b). Large-scale subsidence is a major source of mass-flow into the boundary layer, but this is not the case for moisture since the subsiding air tends to be much drier. There is also some ventilation noticeable south of the low centre and wrapping westwards around the south of the high pressure. This is matched by convergence, as shown in Figure 4.6(b), and is associated with the cold front, which at this stage is intensifying and starting to form a long, trailing front which almost wraps around the entire domain. The convergence of air forming the front is also responsible for moisture convergence and ventilation through frontal ascent. Ventilation appears enhanced directly south of the low centre due to sharp gradients in  $h$  near the cold front, so that there is a tendency for the boundary layer to be ventilated via frontal outflow. However, term 1 in Equation 4.11 acts to balance this frontal outflow, since at a fixed point in space, the boundary layer is growing in time as the front passes over it.

The other major difference to the dry simulations is the transport of moisture by shallow convection (Figure 4.6(d)). Whilst the strongest ventilation of moisture is on the warm-conveyor belt, the large area over which shallow convection occurs means that the total, domain-integrated, moisture ventilated by the two processes is comparable. At the time shown (day 7), moisture is being ventilated at a rate of  $3.1 \times 10^8 \text{ kgs}^{-1}$  by large-scale advection (i.e., due to term 2, as in Figure 4.6(a)), compared with  $3.5 \times 10^8 \text{ kgs}^{-1}$  by shallow convection (i.e., due to  $(\rho q w)_{\text{conv}}$ , as in Figure 4.6(d)). Indeed, the two processes are of comparable importance throughout much of the life cycle, albeit with shallow convection triggering slightly earlier in the life cycle and with the large-scale moisture flux becoming the stronger process as the cyclone-wave intensifies. Gutowski and Jiang (1998) discussed how moisture introduced into the troposphere at the shallow convective cloud-tops can be advected eastwards and polewards by the cyclone wave. However, unlike the warm-conveyor belt flow, this moisture flow does not ascend, but rather remains between 3 and 4 km for several days, before converging in the region of the cold front. This shall therefore be investigated further in the next section.

## 4.5 MOISTURE CYCLE OF A CYCLONE-WAVE

Section 4.4.2 has demonstrated that there are two main processes by which moisture is ventilated from the cyclone-wave boundary layer – large-scale ascent on the warm-conveyor belt and convective ventilation in shallow cumulus clouds behind the cold front. However, it was also shown that the main source of boundary-layer moisture was from surface evaporation behind the cold front. Therefore, the cyclone boundary layer is capable of taking moisture from a single source region and processing it through two separate ventilation regions.

Figure 4.7(a) shows a time series of boundary-layer ventilation from these two processes over the life-cycle. As discussed in Section 4.4.2, the shallow convection triggers around day 4 and

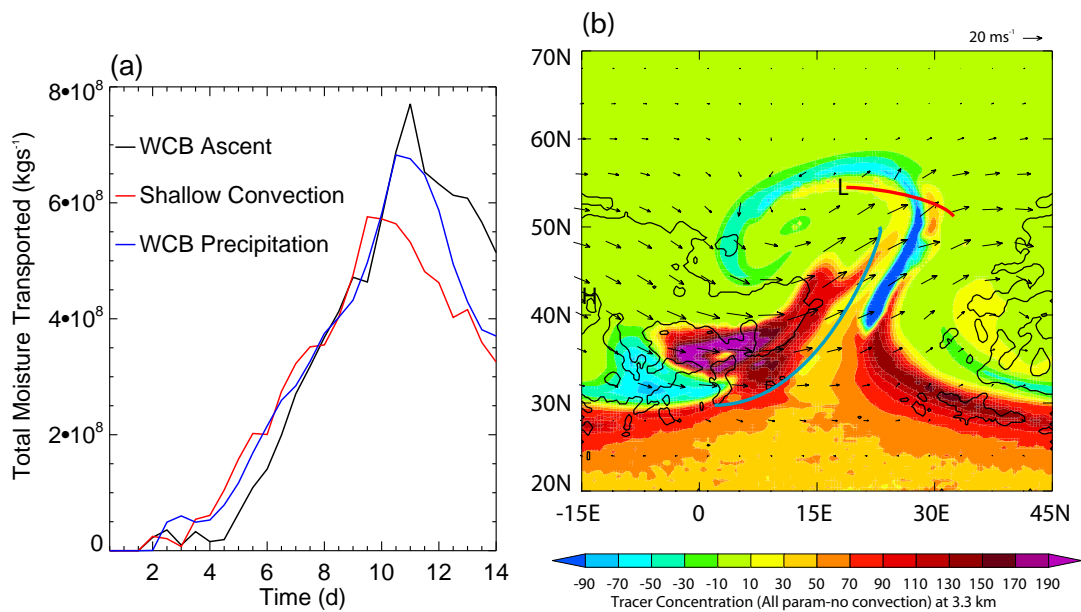


**Figure 4.7** (a) Time series of total moisture ventilated from the boundary layer by warm-conveyor belt ascent (black) and shallow convection (red). Also shown is the surface precipitation rate in the warm-conveyor belt (blue). (b) Tracer concentration (arbitrary units) ventilated by convection at 3.3 km (coloured) with wind vectors at 3.3 km overplotted, at day 9. Regions of cumulus-capped boundary layers are also marked, by thick lines.

ventilates at a slightly faster rate than the WCB up to day 8. The shallow convective ventilation peaks at day 10 before decaying, whilst the WCB ventilation continues to day 11, coincident with the peak EKE, shown in Figure 2.11(b). The WCB ventilation also peaks approximately 20%

higher than the convective ventilation, before starting to decay at a similar rate. This increased peak means that over the 14 days of the life-cycle, the WCB ventilates  $\approx 10\%$  more moisture than the shallow convection.

Figure 4.7(a) also shows the precipitation rate in the warm-conveyor belt region. Here, and throughout the rest of this thesis, the warm-conveyor belt area is defined using the method of Sinclair *et al.* (2008), which locates the 95th percentile of the entire  $w_h$  data-set, and defines the WCB as any ascent greater than this value. Sinclair *et al.* (2008) demonstrated that this definition finds the majority of the WCB, rather than just the core. Increasing the percentile would result in only part of the WCB ventilation being observed, whereas reducing the percentile leads to the inclusion of areas which are not part of the WCB. As shown, the precipitation rate closely matches the WCB ventilation rate, confirming the statement in Section 4.4.2 and the findings of Eckhardt *et al.* (2004) that WCBs are approximately 100% efficient at converting moisture into precipitation. There is no time-lag in this process, due to the presence of a background moisture profile. As soon as ascent starts (around day 3), some moisture present within the troposphere is forced to ascend past its lifting condensation level, condensing into cloud and eventually precipitating. At the same time, moisture is ventilated from the boundary layer to replace the moisture lost from the troposphere. Hence the conveyor belt analogy is a good one, as moisture is “loaded” onto the conveyor belt at one end (in the boundary layer), whilst microphysical processes remove moisture at the other end (in the troposphere) at approximately the same rate. The total moisture content of the troposphere is therefore unchanged by this process, although its spatial distribution is. Since the WCB also flows polewards, atmospheric water vapour is moved polewards by the WCB. Hence the WCB forms part of the cyclone’s ability to transport water vapour long distances polewards, as discussed by Stohl *et al.* (2008).

Attention is now focussed on the moisture ventilated by shallow convection. To ascertain how this moisture is transported by the cyclone, a tracer study has been performed. A passive tracer is emitted at the surface continually throughout the life-cycle. It is massless and so its quantity is meaningless: it acts simply as a tracer to track airflows within the cyclone. The advantages of a tracer study are that different tracers can be passed through different parameterisation schemes, demonstrating the importance of different physical processes on tracer transport. Two tracers are emitted at the same rate from the surface, the first of which is acted upon by the model dynamics,

the boundary layer parameterisation and the convective parameterisation. The second tracer is only acted upon by the model dynamics and the boundary-layer scheme. Therefore the second tracer represents what would happen if no convection was present, and the difference between the two tracers represents the action of convection on the tracer concentrations. The tracer transport can be used as a proxy for moisture transport by convection because the convection occurs over regions of large, positive surface latent heat fluxes, and so the continual tracer source from the surface represents the moisture source. The convection occurs above a well-mixed sub-cloud layer, and so the concentrations of both moisture and tracer are well-mixed below the cloud base. Figure 2.12 shows that there is no heavy precipitation in the convective regions – there are some showers, which will act to remove some moisture, but they are not heavy enough to remove all moisture. Therefore a tracer which is not removed by precipitation is representative of what will happen to any moisture which is not precipitated.

Figure 4.7(b) shows the distribution of this tracer difference at day 9 at the approximate height of the convective cloud tops. The figure shows a large increase in tracer behind the cold front, between 0-15E, 30-40N, which is tracer ventilated by shallow convection. It is noticeable that this tracer is no-longer located in the region of cumulus capped boundary layer, but has been advected eastwards by the jet, towards the cold front. This is consistent with the results of Gutowski and Jiang (1998), who demonstrated that tracers released near convective cloud tops can be transported eastwards and polewards over several days, towards the cold front. The poleward motion of these tracers is noticeable around 15E, 45N, as a tongue of high tracer concentration extends towards the low centre. This tracer therefore demonstrates how moisture ventilated by shallow convection is transported eastwards and polewards (in a system relative sense) within the troposphere, towards the cyclone cold front. Comparing to Figure 2.12(b) shows that some of this moisture is precipitated back to the surface in showers located within the cold air outbreak. The remaining moisture must eventually return to the surface as precipitation, since over the whole life-cycle precipitation approximately balances evaporation, and this is likely to occur on the cold front.

Section 2.4.2 discussed how these idealised cyclones remain confined within the latitude band of the initial zonal jet, particularly in Cartesian simulations. However, in reality cyclones are known to migrate polewards, especially in the North-Atlantic where the jet orientation is typically

south-west to north-east. It has been demonstrated that moisture is transported polewards in a system relative sense and therefore if the system is also migrating significantly polewards, the poleward moisture transport will be enhanced. Therefore, convective processes are a significant contributor to the poleward moisture transport by mid-latitude cyclones.

Figure 4.7(b) also shows a large decrease in tracer in the WCB region (20-30E, 40-50N). There is also a decrease in tracer concentrations near the high pressure centre, around  $-10\text{E}$ ,  $35\text{N}$ , which is part of the anticyclonic branch of the WCB which has descended under large-scale subsidence. This implies that the concentrations in these regions are higher for the tracer not acted upon by the convection parameterisation than the tracer acted upon by all parameterisations. Therefore, it appears that the convection is reducing the ability of the WCB to ventilate tracer. Since convection removes tracer from the post-frontal regions on the timescale of hours, there is less tracer in these regions to be transported within the boundary layer by divergent motions. Therefore, less tracer converges into the WCB footprint and less is available for ventilation. When the tracer cannot be ventilated by shallow convection, it accumulates in the boundary layer and is transported and ventilated by large-scale processes. Moist convection acts as a limiting process on the tracer ventilation by the WCB.

The consequences of this for moisture transport are less certain. The results suggest that if there were no convection, then, as happened with the tracer, more moisture could be ventilated by the WCB, ultimately enhancing WCB precipitation rates. Whilst this would not happen in reality, as convection cannot simply be turned off, the results do have consequences for NWP and climate simulations. The convection parameterisation is not perfect, and different models use different convection parameterisations, which could ventilate different amounts of moisture. Whilst it is beyond the scope of this study to investigate the sensitivity of the convective ventilation to the parameterisation used, the tracer study demonstrates that any differences in the convective ventilation could feed back onto the large-scale. Therefore, it is possible that two different convection schemes ventilating different amounts of moisture could lead to changes in the large-scale ventilation and WCB precipitation.

The boundary layer therefore plays an important role in the moisture cycle of a cyclone-wave. By latent-heat exchange with the surface, boundary-layer processes provide an important source of moisture to the atmosphere. Fast convective processes are able to remove large amounts of

moisture from the boundary layer, which is transported eastwards and polewards by the cyclone system. The convection also regulates the amount of moisture that is available to be transported by slower, large-scale processes within the boundary layer. Ultimately, this affects the ventilation rate by the WCB and the precipitation delivered by the cyclone, demonstrating that boundary-layer processes play a key role in the mid-latitude water cycle.

## 4.6 CONCLUSIONS

The boundary-layer structure that evolves under a developing mid-latitude cyclone wave has been investigated, with the aim of expanding conceptual models of dry boundary layers on this scale. Locally and instantaneously, the structures observed mirror closely textbook boundary-layer types. In post-frontal and high-pressure regions, the evolution is analogous to daytime convective boundary-layer growth, with a single mixed layer growing past the lifting-condensation-level, capping stratocumulus becoming decoupled from the surface and cumulus convection initiating beneath it. Within the warm sector, the evolution is more typical of a nocturnal boundary layer, with a stable profile, low-level cloud or fog formation, and dew condensing out onto the surface. These two extremes are also linked by transitional regions as the cyclone wave progresses.

The inclusion of moisture introduces an extra aspect for the conceptual boundary-layer structures formed, and the quantity  $D^*$  allows further classification of three boundary-layer moisture regimes. Low, positive  $D^*$  corresponds to the bottom-up, moistening, boundary layer, which can evolve to support cumulus convection above. High, positive  $D^*$  corresponds to the top-down, entrainment-drying boundary layer, which results in cloud-free air or thin stratocumulus. Negative  $D^*$  corresponds to a boundary layer losing moisture to the surface.

However, these processes are fundamentally different from the traditional “single-column” view of boundary layers. The regimes are not forced by solar heating and the local surface energy balance, but rather by large-scale thermal advection by the synoptic system. It is this synoptic-scale forcing which maintains the structure of the boundary layer over large areas. The character of this forcing also creates subtle differences in the profiles. The warm-conveyor belt boundary layer, for example, departs in some important ways from the classical nocturnal boundary layer, containing Lagrangian, three-dimensional features. Moisture advection, cloud formation

and precipitation all contribute to a well-mixed moisture profile throughout a large depth of the atmosphere, in a region that is stable on buoyancy grounds. This highlights the importance of considering the full three-dimensional structure of the boundary layer in cases where horizontal divergence is large.

Through the use of a boundary-layer moisture budget, it has been possible to quantify how moisture is moved within and ventilated from the boundary layer. There are two main pathways through which moisture is ventilated, and these are shown schematically in Figure 4.8. The warm-

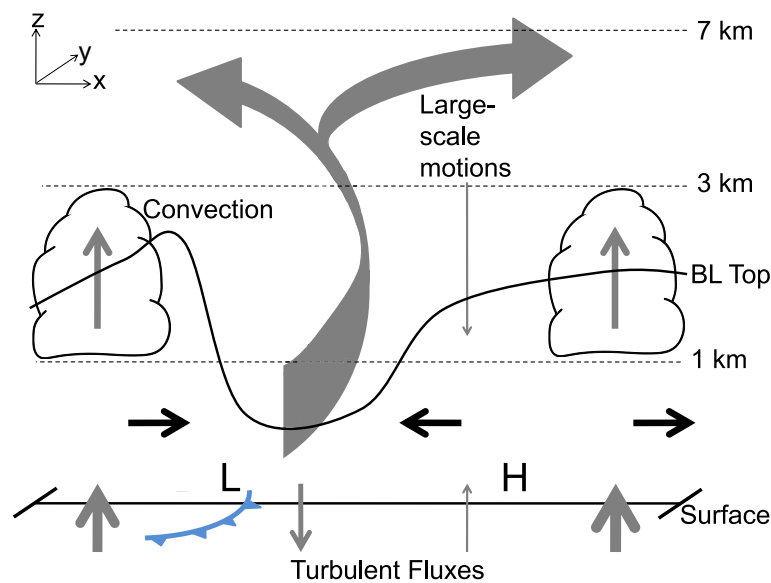


**Figure 4.8** Schematic representing the flows of moisture within the cyclone boundary layer, grey arrows representing sources and sinks of boundary-layer moisture and black arrows representing movement within the boundary layer. The arrow thickness provides a qualitative indication of the relative strength of the various flows. L and H denote the low and high pressure centres respectively, with the cold front marked in blue. The approximate height of features is marked, along with the height of the boundary layer.

conveyor belt ventilates moisture in much the same way as it does mass (Sinclair *et al.*, 2010b), with the moisture source being provided by convergence within the boundary layer. However shallow convection has been demonstrated to be an equally efficient mechanism of ventilating moisture into the free troposphere.

The importance of warm-conveyor belts for moisture transport and precipitation events is

well documented (Eckhardt *et al.*, 2004; Field and Wood, 2007), but until now the importance of boundary layer processes has not been recognised. The moisture budget considered here has uncovered how long-range transport within the boundary layer leads to this moisture convergence under the WCB region. The moisture is evaporated far from the WCB region, into the post frontal and anticyclonic boundary layer, where the latent heat-flux is large and positive. It is then transported by divergent motions that are forced by surface drag and ageostrophic flow, ultimately converging under the warm-conveyor belt source.

A key difference between moisture and some other variables, such as mass or heat, is that moisture flux is almost always directed upwards at the boundary-layer top. In the convective boundary-layer regime, heat and mass are moved into the boundary layer by large-scale subsidence. Although large-scale subsidence does move a small amount of moisture into the boundary layer, in these cyclone waves it is typically co-located with shallow convection, which acts to maintain a net flux of moisture out of the boundary layer. This ventilation mechanism will also have consequences for pollutant transport out of the boundary layer. Sinclair *et al.* (2008) discussed how dry cyclone waves can remove pollutants from the boundary layer on the WCB, but this study has shown that shallow convection would be expected to increase the ventilation rate.

Figure 4.8 shows how moisture is continually being redistributed within the cyclone wave so that there are no locations where the boundary layer is strongly moistening or drying. This again demonstrates the importance of examining the three-dimensional boundary-layer structure, since the simple  $D^*$  measure cannot account for this continual transport. Evaporation acts to moisten post-frontal and high-pressure regions, while divergence and convection act to dry these regions. By contrast, convergence acts to moisten the low-pressure regions, whilst condensation and large-scale ascent act to dry these regions. Large-scale motions outside the boundary layer act to move the moisture ventilated eastwards and northwards, eventually returning it to the surface as precipitation great distances from where it was originally evaporated.

Other processes not included in this study will also affect the boundary-layer structure. Whilst the diurnal cycle is small over the ocean, cloud-radiation feedbacks will affect the observed cloud structure. If radiation had been included in the simulations, a de-stabilising effect on the atmosphere would be anticipated, reducing the size of the stable areas and increasing the extent of the convective boundary layer. Section 3.3 also demonstrated the large effect that variations in

sea-surface temperature can have on surface fluxes. However, comparison to case studies (e.g. Neiman *et al.*, 1990; Brown *et al.*, 2008) demonstrates that the results presented here are certainly realistic and any such uncertainties would appear most unlikely to affect the qualitative conclusions that have been drawn. Moreover, the techniques employed could be applied to simulations of real cases in order to study the mid-latitude water cycle. Latent heat released from warm-conveyor belt rain has a large affect on cyclone development, and cyclone waves provide the major engine for poleward transport of heat and moisture. Hence the understanding obtained here of how tropospheric moisture is connected to its oceanic source, and how the moisture evolution is mediated by boundary-layer dynamics, has important consequences for weather and climate studies.

# CHAPTER 5:

# FACTORS CONTROLLING CYCLONE

# MOISTURE TRANSPORT

## 5.1 INTRODUCTION

Chapter 4 investigated the boundary-layer structure and low-level moisture transport in an idealised, numerically simulated cyclone-wave. Boundary-layer budgeting techniques were used to quantify the evaporation, transport and ventilation of moisture from the boundary layer. It was shown that large-scale ventilation on the warm-conveyor belt was of similar importance to shallow convective ventilation in cumulus clouds, demonstrating that both processes play an important role in the vertical transport of moisture from the surface into the free troposphere. It was also demonstrated how the moisture was transported zonally and meridionally by the synoptic-scale dynamics, modifying the tropospheric moisture profile or being precipitated back to the surface. However, it was not established how the relative importance of the two ventilation processes may change with large-scale and boundary-layer parameters.

As demonstrated in Section 2.5.2, the idealised cyclone simulated ( $AM_{BL}$ ) was typical of a northern-hemisphere, marine, wintertime system. However, real-world cyclogenesis events tend to be varied in character, with large differences in structure and intensity, caused by variation in large-scale parameters such as the jet strength, moisture availability and the influence of pre-existing systems. The North-Atlantic Oscillation (NAO) is known to exert a strong control over the mid-latitude jet, causing variations in its strength and orientation, which, in turn, exerts a control over the strength and location of mid-latitude cyclones. However, less is known about the relationship between large-scale forcings like this and the mid-latitude water cycle. Stohl *et al.* (2008) and Ruprecht *et al.* (2002) have discussed the link between poleward moisture transport and the NAO. Stohl *et al.* (2008) demonstrated that in a positive phase of the NAO, characterised

by a stronger mid-latitude jet, subtropical sources of moisture are more important for heavy rainfall events in mid-to-high latitudes. Ruprecht *et al.* (2002) also demonstrated higher polewards moisture transport in a positive phase of the NAO, linked to more intense cyclones producing the transport. They also showed that the location of maximum moisture transport was shifted further north in a positive NAO, linked to a poleward shift of the jet under positive NAO conditions.

Moisture transport has important implications for forecasting of extreme cyclogenesis events. The link between mid-tropospheric latent-heat release and cyclone intensity is well established, for example Stoelinga (1996) and Ahmadi-Givi *et al.* (2004) give a PV interpretation of the phenomenon. Zhu and Newell (1994) demonstrated that “atmospheric rivers” are often seen in advance of rapid cyclogenesis or “bombs”. They introduced the term “river”, since these atmospheric moisture flows transported as much water as the Amazon, and suggested that as the evolving cyclone tracks across the location of the atmospheric river, latent heat release causes rapid deepening of the cyclone. Gyakum and Danielson (2000) showed that surface evaporation played a strong role in explosive cyclogenesis, contributing to the higher precipitation rates observed in bomb cyclogenesis. This study will stop short of discussing how the latent-heat release affects cyclone development, but rather will focus on the equally important, but less-studied question of how the moisture gets to a location where it is dynamically important. How and why do changes in surface evaporation affect precipitation rates?

There are also important climatological questions that can be answered by investigating cyclone moisture transport. Recent papers by Field and Wood (2007) and Field *et al.* (2008) have discussed the structure of cyclones in a composite of both real-world events and climate model simulations. They discussed how the cyclone averaged near-surface windspeed,  $\langle V \rangle$ , and water-vapour path,  $\langle WVP \rangle$ , could be used as independent metrics of cyclone intensity and moisture availability, to explain a considerable amount of observed variability. They showed how the warm-conveyor belt rainrate was proportional to the product of these two metrics, and that  $\langle WVP \rangle$  increased with increasing sea-surface temperature (SST) according to the Clausius-Clapeyron equation. They also discussed the implications of their results for how cyclones may change in a warming climate. Allen and Ingram (2002) discuss how the Clausius-Clapeyron equation should give a  $6.5\%K^{-1}$  increase in global atmospheric water vapour storage, but the total global precipitation should only increase at  $2 - 3\%K^{-1}$ , constrained by the global energy balance. Hence

Field and Wood (2007) and Field *et al.* (2008) suggested that cyclones will be fewer in number or less intense to account for this difference, effects which have both been seen in modelling studies (Meehl *et al.*, 2007; Bengtsson *et al.*, 2006), but it is presently unclear which process is more likely. How does the mid-latitude jet structure need to adjust to compensate for these precipitation changes?

This chapter will investigate how the moisture cycle of mid-latitude cyclones varies with changes to large-scale parameters, attempting to answer the questions that have been raised above. Section 5.2 will investigate how changes to large-scale parameters influence the moisture cycle. In Section 5.2.1 changes to the relative humidity distribution will be investigated, demonstrating why the idea that relative humidity remains approximately constant (e.g. Field and Wood, 2007; Allen and Ingram, 2002) works so well for mid-latitude cyclone waves. Section 5.2.2 will investigate the affect of the absolute atmospheric temperature on the cyclone moisture cycle, with Section 5.2.3 considering the effect of the meridional temperature gradient. Scaling arguments for how these large-scale changes affect both the advective and convective moisture ventilation from the boundary layer will be given in Section 5.3. Section 5.4 will then discuss how changes to the boundary-layer structure can have markedly different effects on the two ventilation processes, before conclusions are drawn in Section 5.5.

## 5.2 LARGE-SCALE CONTROLS

This section will investigate how changes to the large-scale atmospheric state, i.e. the initial conditions for the idealised simulations, control the moisture ventilation from the boundary layer. A metric of boundary-layer moisture ventilation has been constructed, given by

$$Q = \int_{\mathcal{T}} \int_A (\rho q)_h w_h dA dt, \quad (5.1)$$

where  $Q$  is the total mass of moisture ventilated by the process of interest,  $\mathcal{T} = 14$  days is the time of a single life-cycle and  $A$  is the area over which ventilation occurs. Motivated by Section 4.5, ventilation by WCB advection (denoted  $Q_{\text{wcb}}$ ) and shallow convection (denoted  $Q_{\text{conv}}$ ) shall be focussed on. It is possible that ventilation can occur by large-scale advection that is not in the WCB: however, direct computation demonstrates this residual term to be small. Therefore,  $Q$

represents the time-integral of each process shown in Figure 4.7(a).  $\tau = 14$  days is chosen as a fixed timescale to average over, and how this may change with the variation of large-scale parameters shall not be considered. The variation of  $w_h$  and  $q_h$ , i.e. the flux of moisture out of the boundary layer, is the primary focus here.

### 5.2.1 RELATIVE HUMIDITY

Section 2.5.1 showed that the relative humidity (RH) profile chosen for simulation  $AM_{BL}$  was representative of the wintertime storm track climatology, based on a comparison with NCEP reanalysis. Equation 2.41 was used to define the vertical profile of RH, with a maximum value of  $RH_0 = 80\%$  at the surface. This maximum surface value will be varied here to identify the effects of RH changes on the cyclone moisture cycle. Figure 5.1 shows a time series of minimum mean sea-level pressure (MSLP) and eddy kinetic energy (EKE) for various values of  $RH_0$ . The

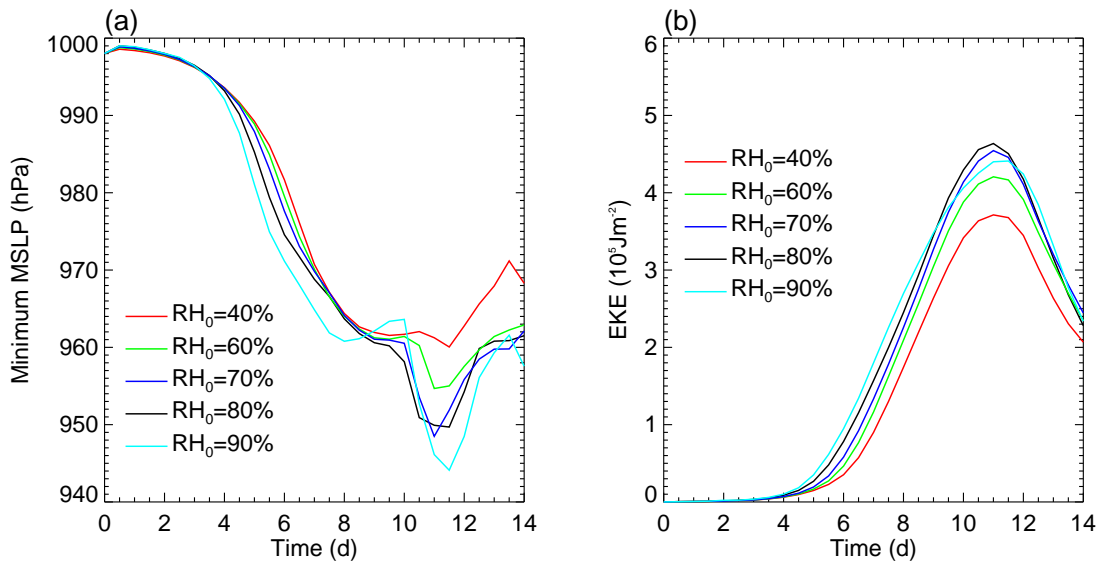


**Figure 5.1** Time series of (a) minimum sea-level pressure and (b) eddy kinetic energy, for various values of the initial surface RH (shown on the plots).

difference in atmospheric moisture starts to affect the cyclone development at day 4, shown by the diverging minimum MSLP curves shown in Figure 5.1(a). However, by day 7, for all but the most intense system, the MSLP curves have joined up again, with most experiments now showing similar values of minimum MSLP. Only  $RH_0 = 90\%$  evolves differently, since there is

initially so much moisture present in the atmosphere that very strong latent-heat release occurs in the cyclone interior, resulting in a stronger cyclone being formed. Most simulations show the localised re-intensification in the MSLP after day 10, as discussed in Section 2.5.2. However, once again the feature responsible does not show up in the EKE, demonstrating that it is small scale. Examination of the simulations again shows that it is associated with near-surface latent-heat release, forcing a localised spin-up. The EKE curves show very little difference between the experiments. There is a slight trend that higher values of  $RH_0$  lead to higher EKE. This is to be expected since the increased moisture intensifies the system by latent-heat release (Emanuel *et al.*, 1987; Ahmadi-Givi *et al.*, 2004), but the variation is small.

The reasons for the similarity between experiments with different  $RH_0$  values can be understood in terms of the moisture cycle discussed in Section 4.5. Figure 5.2 shows how  $Q_{wcb}$  and  $Q_{conv}$  vary with  $RH_0$ . The figure shows that  $Q$  from either process is largely insensitive to

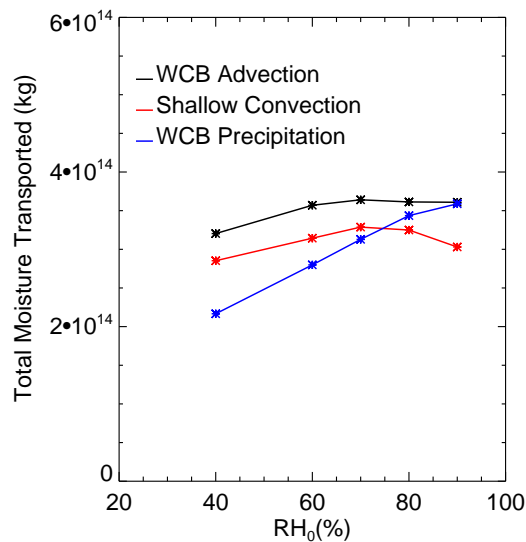


**Figure 5.2** Total mass of moisture ventilated from the boundary layer ( $Q$ ) by WCB advection (black) and shallow convection (red) versus the initial value of  $RH_0$ . Also shown is the total WCB Precipitation delivered by the life-cycle (blue).

changes in  $RH_0$ , demonstrating that boundary-layer ventilation, by both advective and convective processes, has only a weak dependence on the initial RH profile.

The reason for this is that over a sea-surface, moisture is freely available to be evaporated

from the sea, and this supplies moisture that is ultimately ventilated. For the control run ( $AM_{BL}$ ), Chapter 4 has demonstrated that the boundary-layer moisture budget is balanced, with input from evaporation balanced by ventilation. Similarly, the reanalysis data shown in Figure 2.7 demonstrates that the long-term average near-surface RH is around 80% in mid-latitude regions. Therefore,  $RH_{eq} = 80\%$  is defined as the equilibrium value of boundary-layer RH. When  $RH_0 < RH_{eq}$  evaporation from the sea surface increases to restore equilibrium. The timescale to obtain equilibrium can be estimated as the ratio of the moisture required to the rate of moisture input, namely

$$\tau_{adj} = \frac{\rho q_{sat} h (RH_{eq} - RH_0)}{\rho C_H |\mathbf{v}_1| q_{sat} (1 - RH)}. \quad (5.2)$$

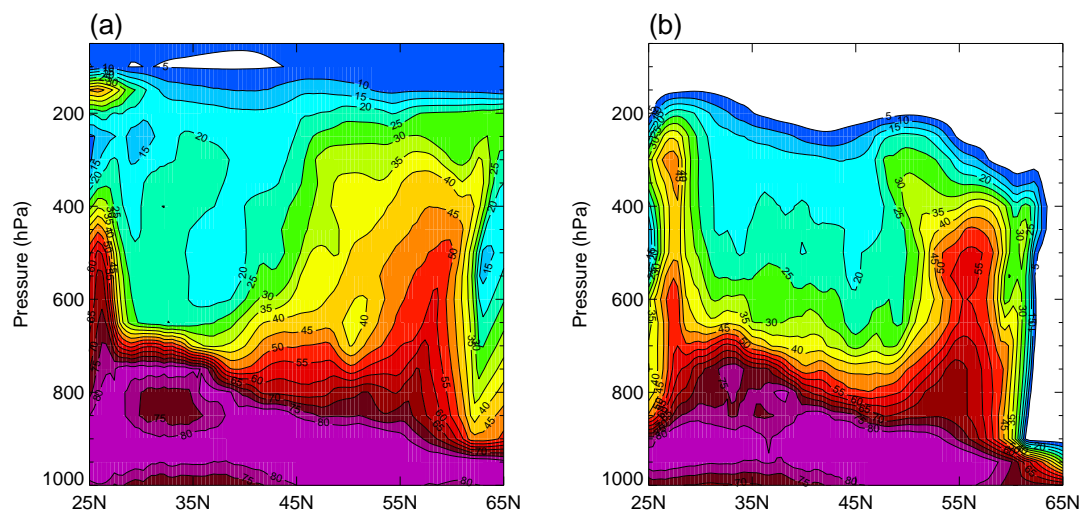
This assumes that ventilation is initially weak, which Figure 4.7(a) shows to be reasonable in the first 4 days of the life-cycle. Estimates of  $h \approx 1$  km,  $C_H \approx 2 \times 10^{-3}$  and  $|\mathbf{v}_1| \approx 5$  ms<sup>-1</sup> are used, and  $RH = RH_{eq}$  is taken as an upper bound for the actual boundary-layer relative humidity. These values give  $\tau_{adj} = 2.3$  days when  $RH_0 = 40\%$ , decreasing to zero as  $RH_0$  is increased to 80%. Therefore, the adjustment timescale of the boundary-layer moisture content is fast compared to the life-cycle timescale, and so the boundary-layer moisture content is close to its equilibrium value throughout the life-cycle, and therefore ventilation is not sensitive to  $RH_0$ . There is a slight reduction in  $Q$  for very low  $RH_0$ , due to the reduced amount of moisture available to be ventilated at early stages of the life-cycle, i.e. when  $t \leq \tau_{adj}$ . In a similar manner, when  $RH_0 > RH_{eq}$ , the evaporation is reduced whilst ventilation is unchanged until  $RH_{eq}$  is reached within the boundary layer.

Figure 5.2 also shows the total mass of moisture returned to the surface by WCB precipitation, which does vary with  $RH_0$ . For the control value,  $RH_0 = 80\%$ , the total precipitation is approximately equal to the total moisture ventilated on the WCB, as discussed in Section 4.5. However, for lower values of  $RH_0$ , the total precipitation delivered is lower, demonstrating that the WCB is no longer 100% efficient at converting moisture ventilated into precipitation. Instead, some of the moisture ventilated is retained within the atmosphere, modifying the background RH profile in the free troposphere.

This finding can explain the time series shown in Figure 5.1. For different values of  $RH_0$ , the large-scale cyclone dynamics initially follow the same evolution. The surface evaporation, boundary-layer transport and ventilation are similar in all experiments. However, precipitation formation is weakened at lower values of  $RH_0$ , since the free troposphere, where most of the

precipitation forms, is further from saturation and needs to be moistened before precipitating cloud can form. Therefore, the precipitation rate is initially lower, demonstrating why the curves diverge at such an early time, due to the modified latent-heat release. Moisture accumulates within the atmosphere, modifying the RH profile, which then approaches that of the control experiment. Later in the life-cycle, the RH profiles are very similar, forcing similar cyclone development towards the end of the life-cycle. For increased initial moisture content ( $RH_0 = 90\%$ ), there is intense precipitation from an early stage of the life-cycle. This releases large amounts of latent heating in the mid-troposphere, which forces a more intense cyclone system to develop. But as shown in Figure 5.1(b), the EKE returns to values typical of lower  $RH_0$  later in the life-cycle (around day 10), when the precipitation rate is reduced.

These simulations show why, for mid-latitude regions, the RH profile remains approximately constant. If, for any reason, the RH profile is moved away from its equilibrium state, evaporation and precipitation processes, driven by the large-scale cyclone dynamics, redistribute moisture until the equilibrium state is returned. This adjustment process is fast and can happen within one cyclone life-cycle. Figure 5.3 shows the zonal-mean relative humidity at day 14 from simulations



**Figure 5.3** Zonal-mean relative humidity (contoured, interval 5%) at day 14 from (a) simulation  $AM_{BL}$ , i.e.  $RH_0 = 80\%$ , and (b) a simulation where  $RH_0 = 0\%$ .

with  $RH_0 = 80\%$  and  $0\%$  respectively. It can be seen that between  $30 - 60N$  and up to 200 hPa (the region the cyclone system influences), the two simulations are similar qualitatively and even

quantitatively, demonstrating that even a single life-cycle can create a profile close to climatology (shown in Figure 2.7(a)). The cyclone has not produced any moisture transport further north than 60N, and has also not exported any moisture into the stratosphere, meaning other processes are important for these transports.

### **5.2.2 ABSOLUTE TEMPERATURE**

Dry simulations of cyclogenesis are not affected by the absolute temperature of the atmosphere – only the meridional temperature gradient is important, as shown by the Eady growth rate (Eqn. 1.8). Section 5.2.1 demonstrated that the initial moisture content of the atmosphere does not affect the cyclone moisture cycle to any great extent, since the atmosphere recovers its equilibrium relative humidity by evaporation and precipitation processes. The absolute temperature of the atmosphere does change the potential for holding moisture within the atmosphere, through the Clausius-Clapeyron relation, and so should affect the moisture cycle, and hence possibly the large-scale development of the system via higher latent-heat release.

These possibilities are investigated by a series of simulations where a constant value is added to or subtracted from the atmospheric and surface temperature profiles. The temperature changes will be interpreted in terms of the surface temperature at 45N (the jet centre,  $\hat{\phi}$ ), which is denoted by  $T_0$ . For simulation AM<sub>BL</sub>  $T_0 = 280$  K. The relative humidity profile is fixed across all experiments and therefore the specific humidity profile changes for each simulation, dependent on the atmospheric temperature. Figure 5.4 shows the evolution of minimum MSLP and EKE for several simulations with different temperatures. The general trend is that a higher temperature leads to more intense systems.

Figure 5.5 shows the variation of  $Q$  with  $T_0$ . As anticipated by the Clausius-Clapeyron equation, there is a strong relation between the moisture ventilated and the absolute temperature. These results are consistent with those presented by Field and Wood (2007) and Allen and Ingram (2002). Field and Wood (2007) demonstrated that an increase of 7 K in the SST led to an approximately 50% increase in precipitation rate, whilst Allen and Ingram (2002) suggested that if precipitation increased at the same rate as the global increase in atmospheric water vapour storage, then there should be a  $6.5\text{K}^{-1}$  increase. Both of these quantitative predictions fit well with

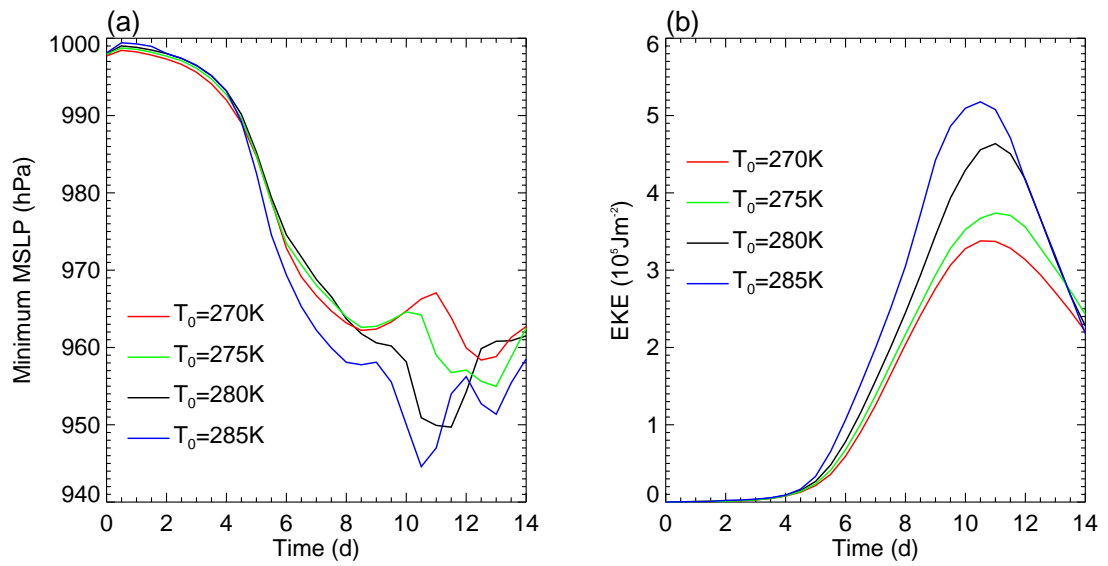


Figure 5.4 Time series of (a) minimum sea-level pressure and (b) eddy kinetic energy, for various values of the initial surface temperature at  $\hat{\phi} = 45\text{N}$  (shown on the plots).

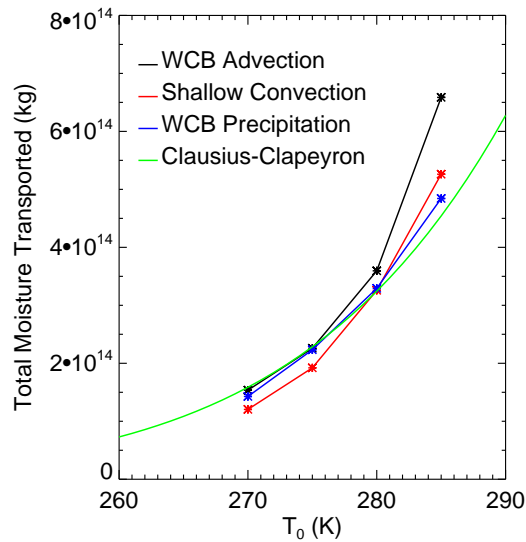


Figure 5.5 Total mass of moisture ventilated from the boundary layer ( $Q$ ) by WCB advection (black) and shallow convection (red) versus the initial value of  $T_0$ . Also shown is the total WCB Precipitation delivered by the life-cycle (blue), and the Clausius-Clapeyron relation (green).

the observed variation in these simulations. The variation in WCB precipitation closely matches what would be expected from the Clausius-Clapeyron relation, as shown in Figure 5.5, whilst the WCB advection and shallow convection have a slightly stronger variation, especially at higher temperatures. This is likely to be due to a positive feedback within the system – at very high temperatures, there is so much latent heat release that  $w_h$  is increased. Examination of the model output has shown that  $w_h$  does show a slight increase as  $T_0$  is increased. Therefore, most of the variation in  $Q$  can be explained by the change in  $q_h$  due to Clausius-Clapeyron, and the additional variation comes from the higher values of  $w_h$ .

### 5.2.3 MERIDIONAL TEMPERATURE GRADIENT

The meridional temperature gradient, characterised by the peak jet speed ( $U_0$ ) is known to be one of the three key large-scale parameters affecting cyclone evolution. The others, as shown by the Eady model growth rate (Eqn. 1.8), are the static stability ( $N$ ) and Coriolis parameter ( $f$ ). A recent paper by Sinclair *et al.* (2010a) has discussed how these three parameters affect boundary-layer ventilation of passive tracer in dry life cycles (simulation AD<sub>BL</sub>). In this section, the meridional temperature gradient is focussed on as a large-scale driver of cyclone intensity. The meridional temperature gradient is the most variable of these three parameters, changing on seasonal timescales (the winter jet is stronger than the summer jet), interannual timescales (the NAO exerts a control on the jet strength) and climatological timescales (the meridional temperature gradient may change as the climate changes).

Equation 2.38 was used to define the jet structure, with the peak jet speed  $U_0 = 45\text{ms}^{-1}$  in simulation AM<sub>BL</sub>. Figure 5.6 shows the time series of minimum MSLP and EKE for simulations with various values of  $U_0$ . As anticipated, the jet strength acts as a sensitive control on the cyclone intensity, with faster jet speeds forcing stronger cyclone systems.

The variation of  $Q$  with  $U_0$  is shown in Figure 5.7, and shows a strong dependence. A regression on a log-plot shows the dependence to be  $Q \sim U_0^3$ . The results presented by Sinclair *et al.* (2010a) demonstrated that  $w_h \sim U_0^2$ , and it is anticipated that, for the large-scale ascent, this relationship should hold true here. There must therefore be an additional scaling of  $q_h \sim U_0$ , which can be explained in terms of the moisture cycle as follows. According to thermal wind balance, if

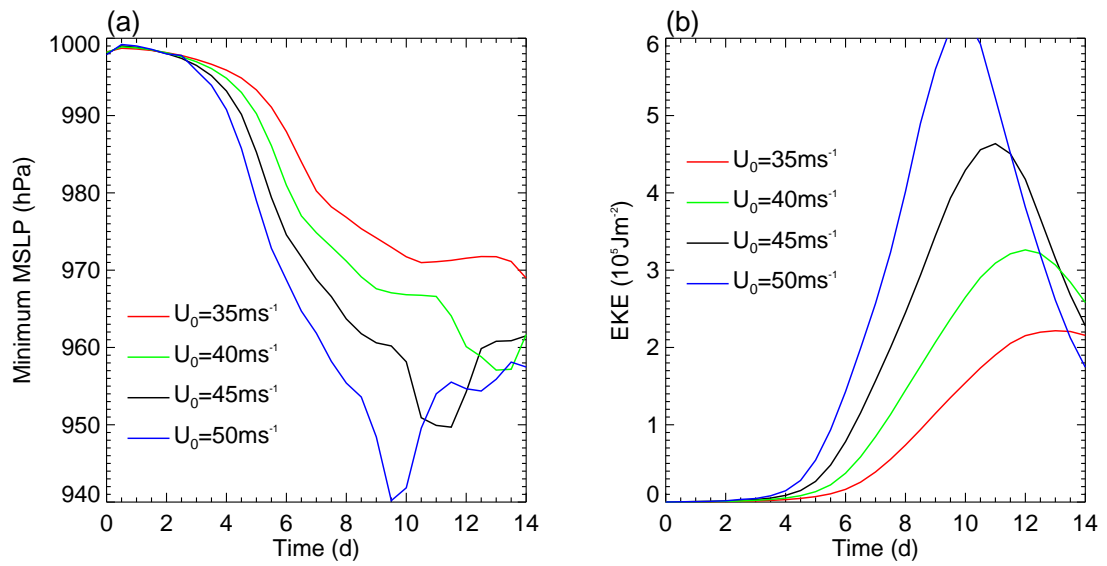


**Figure 5.6** Time series of (a) minimum sea-level pressure and (b) eddy kinetic energy, for various values of the peak jet speed (shown on the plots).

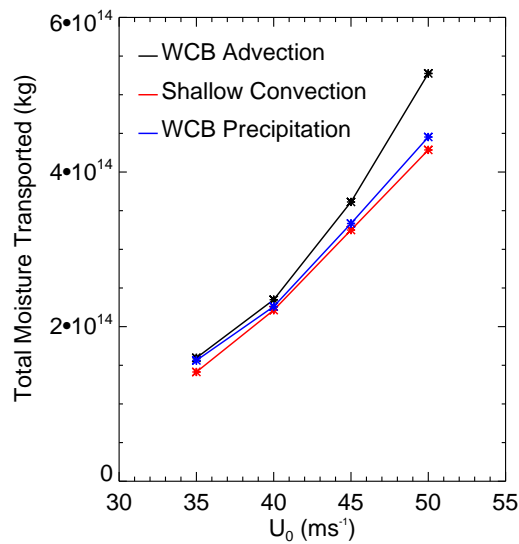


**Figure 5.7** Total mass of moisture ventilated from the boundary layer ( $Q$ ) by WCB advection (black) and shallow convection (red) versus the initial value of  $U_0$ . Also shown is the total WCB Precipitation delivered by the life-cycle (blue).

$U_0$  changes then so does the meridional temperature gradient.  $T_0$  is held constant across this set of simulations and so for increased  $U_0$ , the air (and SST) to the south of the jet is warmer. This increases the potential for the atmosphere in this region to retain more moisture, as demonstrated in Section 5.2.2. Chapter 4 demonstrated that the moisture ventilated has its origins to the south of the jet centre, within the high-pressure part of the wave. Therefore it appears that  $q_h$  has been increased by the higher temperatures in the source region of the moisture. The reasons for the linear scaling will be discussed next.

### 5.3 SCALING MOISTURE VENTILATION

Scaling arguments can be used to assess quantitatively how changes in one or more large-scale variables will affect cyclone characteristics, and in this case, moisture ventilation. Each of the factors in Equation 5.1 will need to be scaled to establish the dependence of the total moisture ventilated over a life-cycle. As stated previously,  $\mathcal{T} = 14$  days will be used for the timescale of a cyclone life-cycle, and thus the scalings developed will be equally applicable to the total moisture ventilated or the average flux of moisture out of the boundary layer.

#### 5.3.1 SCALING VENTILATION BY THE WARM CONVEYOR BELT

Sinclair *et al.* (2010a) developed a scaling for  $w_h$  based on theory of baroclinic instability. Either by applying scaling arguments to the relevant terms in the QG omega equation, or from the Eady model, they obtained

$$w_h \sim \frac{v_g f \frac{\partial u_g}{\partial z}}{2N^2}, \quad (5.3)$$

where  $v_g \sim U_0$  and  $\frac{\partial u_g}{\partial z} \sim U_0/z_T$ . Therefore, they obtained a scaling for  $w_h$  in terms of parameters of the initial condition, and demonstrated that the WCB ascent in simulation AD<sub>BL</sub> closely matched Equation 5.3. In simulation AM<sub>BL</sub>, the ascent rate is enhanced on the WCB, but the scaling argument still applies. It is found that  $v_g = 0.36U_0$  gives a very close numerical match between the observed WCB ascent rate and the prediction of Equation 5.3, shown in Figure 5.8(a) for variations in  $U_0$ .

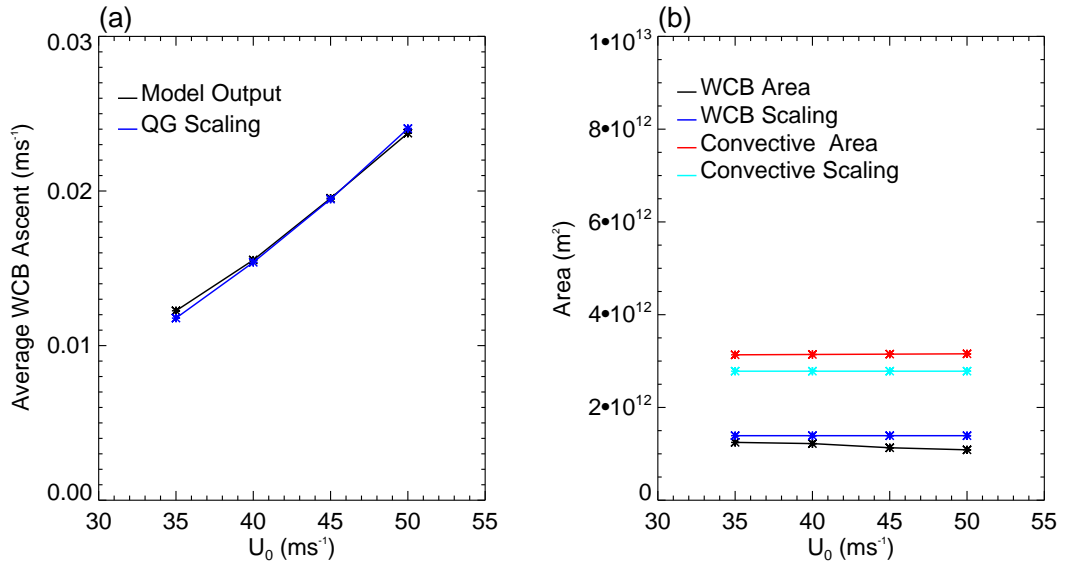


**Figure 5.8** (a) Variation of  $w_h$ , averaged over the WCB area and the life-cycle, with  $U_0$ , and the QG scaling of Equation 5.3 assuming  $v_g = 0.36U_0$ . (b) Variation of the spatial and temporal averaged area of the WCB and convective ventilation, with the scalings used for both as described in the text.

Sinclair *et al.* (2010a) also scaled the area of the WCB as follows

$$\mathcal{A} = \left( \frac{\pi a}{2m} \right)^2, \quad (5.4)$$

based on the assumption that the WCB area was approximately a quarter of the total wavelength. Comparison to model output from simulation AM<sub>BL</sub>, shown in Figure 5.8(b), demonstrates that this approximation is too large by a factor of two, and so  $\mathcal{A}_{\text{wcb}} = \mathcal{A}/2$  is used for the scalings presented here.

In these simulations, the density  $\rho_h \approx 1 \text{ kg m}^{-3}$  and is approximately constant. A final scaling for  $q_h$  is required. By definition

$$q = \frac{e}{1.61(p-e) + e} \approx \frac{e}{1.61p}, \quad (5.5)$$

where  $e$  is the partial pressure of water vapour in air and the approximation is good for  $e \ll p$ . Similarly, by definition  $e = RH \times e_{\text{sat}}$ , therefore

$$q \approx \frac{RHe_{\text{sat}}}{1.61p}. \quad (5.6)$$

Finally,  $e_{\text{sat}}$  is a function of temperature, governed by the Clausius-Clapeyron equation, for which an empirical approximation (Bolton, 1980) is used here, which when substituted into Equation 5.6 gives

$$q \approx \frac{RH}{1.61p} 6.112 \exp\left(\frac{17.67(T - 273.15)}{T - 29.65}\right) = \frac{RH}{1.61p} C(T), \quad (5.7)$$

where  $C(T)$  is introduced to represent the empirical solution to the Clausius-Clapeyron equation as a function of temperature. To obtain a representative value of  $q_h$ , it is therefore necessary to obtain scalings for  $T_h$ ,  $RH_h$  and  $p_h$ , i.e. boundary-layer top values are required since this is where the ventilation is occurring. Comparison to model output demonstrates that the boundary layer is well-mixed in relative humidity, therefore  $RH_h \approx RH_{\text{eq}} = 80\%$ .  $p_h \approx 900$  hPa is used as a typical value of pressure near the boundary-layer top. As discussed in Section 5.2.3, most of the moisture ventilated has its origins to the south of the jet, and therefore a temperature appropriate for the southern part of the domain is required. Since the jet is specified by Equation 2.38 and the temperature profile obtained from thermal wind balance, a scaling for  $T_h$  based on thermal wind balance (Eqn. 1.1) is adopted here:

$$\frac{g}{T_{\hat{\phi}}} \frac{\partial T}{\partial y} = -f \frac{\partial u}{\partial z} \Rightarrow \frac{g}{T_{\hat{\phi}}} \frac{T_{\hat{\phi}} - T_h}{L} \sim -f \frac{U_0}{z_T}, \quad (5.8)$$

where  $T_{\hat{\phi}}$  is a typical value of the boundary-layer top temperature at  $\hat{\phi}$ .  $L = \sqrt{A}$  is a horizontal lengthscale which does not vary between experiments due to the fixed wavenumber used in this study. Re-arranging Equation 5.8 gives

$$T_h \sim T_{\hat{\phi}} \left(1 + \frac{fU_0L}{z_T g}\right). \quad (5.9)$$

In practice,  $T_{\hat{\phi}} = T_0$  is too high to be representative of the boundary-layer top temperature, and therefore  $T_{\hat{\phi}} = T_0 - 5$  is used. 5 K is typical of the drop in temperature across the boundary layer, and this value gives a close match between  $q_h$  defined by Equation 5.7 and the observed values of  $q_h$  within the model.

Combining these scaling arguments gives the following formula for moisture ventilation by the WCB:

$$Q_{\text{wcb}} = \rho_h \tau \cdot \frac{1}{2} \left(\frac{\pi a}{2m}\right)^2 \cdot \frac{0.36 f U_0^2}{2N^2 z_T} \cdot \frac{RH_{\text{eq}}}{1.61 p_h} C \left( (T_0 - 5) \left(1 + \frac{f U_0 L}{z_T g}\right) \right). \quad (5.10)$$

### 5.3.2 SCALING VENTILATION BY SHALLOW CONVECTION

A scaling for the convective ventilation is also desired, to establish why the convection appears to scale in the same manner as the large-scale ventilation in Sections 5.2.1-5.2.3.  $\mathcal{T}$  is identical for the convective ventilation, whilst model output, shown in Figure 5.8(b), demonstrates that  $\mathcal{A}_{\text{conv}} \approx \mathcal{A}$ , where  $\mathcal{A}_{\text{conv}}$  is defined as the number of grid points which contribute to the convective ventilation. The convection occupies approximately a quarter of a wavelength, behind the low centre. As discussed in Chapter 4, the convection forms behind the cold front, in a cold-air outbreak. It is driven by the large-scale dynamics of the cyclone system, which create the positive surface fluxes of sensible and latent heat that drive the convection. To estimate the moisture flux, consider a steady-state boundary layer in which the convective ventilation is entirely governed by the surface moisture flux, namely

$$\overline{w'q'}_{\text{conv}} \sim \overline{w'q'}_0 = C_H |\mathbf{v}_1| (q_{\text{sat}}(\theta_s) - q_1). \quad (5.11)$$

It is found that the convective ventilation is approximately half of the surface moisture flux at any time, i.e.  $\overline{w'q'}_{\text{conv}} \approx 0.5 \overline{w'q'}_0$ . This is shown in Figure 5.9 for simulation AM<sub>BL</sub>, although a similar relation can be found for any of the other experiments conducted. Although  $C_H$  is a function of the

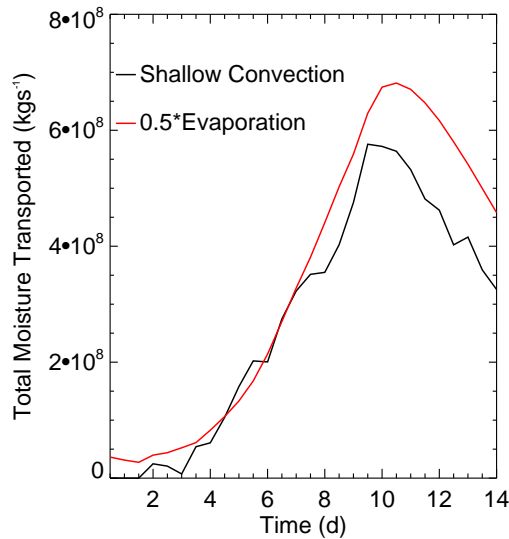


**Figure 5.9** Time series of total moisture ventilated by shallow convection (black) and half the total moisture input from evaporation (red), for simulation AM<sub>BL</sub>.

Obukhov length (Eqn. 2.17), for simplicity it is assumed constant and of value  $2 \times 10^{-3}$ , which

is representative of the convective boundary-layer region over which the convection occurs.  $|\mathbf{v}_1|$  is governed by the large-scale cyclone parameters, driven by the large-scale ascent on the WCB forcing convergence of near-surface winds into frontal regions. Therefore, it is scaled by the continuity equation (Eqn. 2.1b) as follows:

$$\frac{\partial u}{\partial x} + \frac{\partial v}{\partial y} = -\frac{\partial w}{\partial z} \Rightarrow |\mathbf{v}_1| \sim \frac{w_h}{h} \mathcal{L}. \quad (5.12)$$

Finally,  $q_{\text{sat}}$  and  $q_1$  are given by Equation 5.7 as a function of  $T$ ,  $p$  and  $RH$ .  $T$  is estimated using Equation 5.9 to be representative of the location of the convecting region, which is to the south of the jet. Here, surface values are required, and therefore  $RH = RH_{\text{eq}} = 80\%$  is used for  $q_1$  and  $RH = RH_{\text{sat}} = 100\%$  is used for  $q_{\text{sat}}$ .  $p = p_0 = 1000$  hPa and  $T_{\hat{\phi}} = T_0$  are used as representative values near the surface, whilst  $h \approx 1$  km is used as a typical value of the boundary-layer depth.

Combining these scaling arguments gives the moisture ventilation by shallow convection as

$$Q_{\text{conv}} = \rho_h \tau \cdot \left(\frac{\pi a}{2m}\right)^2 \cdot \frac{1}{2} C_H \frac{\mathcal{L}}{h} \frac{0.36 f U_0^2}{2N^2 z_T} \cdot \frac{RH_{\text{sat}} - RH_{\text{eq}}}{1.61 p_0} C \left( T_0 \left( 1 + \frac{f U_0 \mathcal{L}}{z_T g} \right) \right). \quad (5.13)$$

### 5.3.3 COMPARISON OF SCALINGS WITH SIMULATIONS

The scalings presented in Equations 5.10 and 5.13 show how the moisture ventilated varies with  $T_0$  and  $U_0$ . For the large changes in  $T_0$  discussed in Section 5.2.2, the Clausius-Clapeyron relation,  $C(T)$ , produces strong, nonlinear changes to  $Q$ . However, the changes to  $U_0$  discussed in Section 5.2.3, produce only small changes to  $T$ , and the Clausius-Clapeyron relation is in a region of almost linear variation. This explains the apparent  $U_0^3$  variation of  $Q$  observed in Section 5.2.3: the correct scaling should be  $Q \sim U_0^2 C(T)$ , however for the values of  $U_0$  used,  $C(T) \sim U_0$ . Equations 5.10 and 5.13 also suggests some additional factors that may influence  $Q$ , for example, there should be an  $f^2$  and an  $N^{-2}$  dependence of the ventilation. Therefore, four further experiments were performed. Two of these varied the initial values of tropospheric stability, from the control value of  $4 \text{ Kkm}^{-1}$  to a more stable value of  $6 \text{ Kkm}^{-1}$  and a less stable value of  $3.5 \text{ Kkm}^{-1}$ . The other two varied the jet latitude from the control value of  $45\text{N}$  to  $40\text{N}$  and  $50\text{N}$  respectively, thus varying the Coriolis parameter. For these experiments, the use of Cartesian geometry is important, since it ensures that only  $f$  changes, with  $\mathcal{A}$  remaining constant.

Figure 5.10 shows the expected values of  $Q$  obtained from Equations 5.10 and 5.13 plotted

against the observed values from the full range of simulations conducted. A strong correlation is

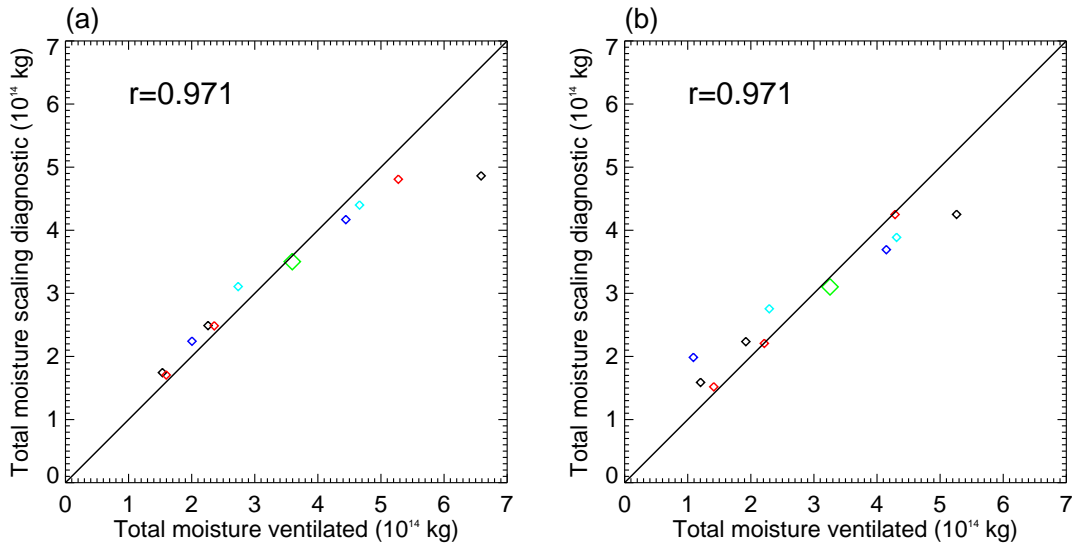


**Figure 5.10** Scatter plots showing the observed values of  $Q$  from direct model output versus the scaled diagnostic of moisture ventilation for (a) the advective WCB ventilation, and (b) the convective ventilation. The green diamond represents the control run, with other simulations performed with varied values of  $T_0$  (black),  $U_0$  (red),  $N^2$  (dark blue) and  $f$  (light blue). The Pearson correlation coefficient is also shown.

shown for both the advective and convective scaling arguments, with correlation coefficients in excess of 0.97. The points are also scattered closely around the 1 : 1 line, demonstrating that the magnitude and variation of ventilation given by the scaling arguments is reasonable. Both plots do however show a gradient slightly less than 1, found to be  $\approx 0.7$  in both cases. This seems likely to be due to latent-heat release feeding back onto cyclone development. In both scaling arguments, the cyclone intensity, characterised by  $w_h$  (Eqn. 5.3) and the moisture content, characterised by  $q_h$  (Eqn. 5.7), have been assumed to be independent. However, as discussed in Sections 5.2.1 and 5.2.2, they are not independent, since increased moisture leads to a more intense cyclone, as shown in Figures 5.1 and 5.4.

Throughout this chapter,  $\mathcal{T} = 14$  days has been chosen as the timescale to average all quantities over. This makes the scalings applicable to the total moisture ventilated in 14 days, or the average flux of moisture out of the boundary layer. In Sections 5.2.1 and 5.2.2, all experiments developed over a similar timescale, with the peak EKE always around day 11, and so the choice

not to vary  $\mathcal{T}$  is reasonable. However, as shown in Figure 5.6, when  $U_0$  is modified (and equally when  $f$  and  $N^2$  are modified), the timescale of the life-cycle is changed. Therefore, to demonstrate that the results really are applicable to the moisture flux, Figure 5.11 shows the moisture flux out of the boundary layer at the time of peak EKE, plotted against the moisture flux scaling diagnostic. The moisture flux scaling diagnostic is obtained by removing the factor  $\mathcal{T}$  from

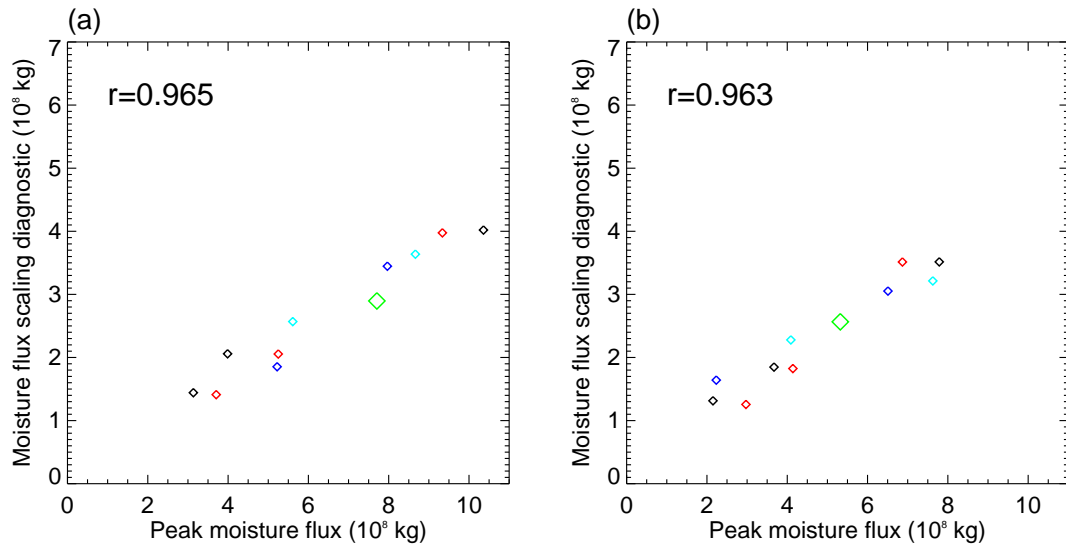


**Figure 5.11** Scatter plots showing the observed values of moisture flux out of the boundary layer at the time of peak EKE, from direct model output, versus the scaled diagnostic of moisture flux for (a) the advective WCB ventilation, and (b) the convective ventilation. The green diamond represents the control run, with other simulations performed with varied values of  $T_0$  (black),  $U_0$  (red),  $N^2$  (dark blue) and  $f$  (light blue). The Pearson correlation coefficient is also shown.

Equations 5.10 and 5.13. The figure shows that a strong correlation is found between the peak flux and the scalings. The magnitudes no longer show as 1 : 1 correspondence, since the scalings have been developed based on average values rather than peak values. The correlation coefficients are still in excess of 0.96, demonstrating that the scalings developed in this section are equally applicable to the flux of moisture out of the boundary layer, even in cases when  $\mathcal{T}$  varies.

## 5.4 SURFACE MOISTURE AVAILABILITY

The warm-conveyor belt is a large-scale, cyclone driven process and so it is expected to be largely insensitive to changes in the boundary-layer structure. For example Sinclair *et al.* (2010a) demonstrated that tracer ventilation on the WCB was insensitive to the amount of boundary-layer drag applied. However, shallow convection is very closely linked to the boundary-layer structure beneath the cloud base, and so it is anticipated that convective moisture ventilation will be affected differently to the WCB ventilation.

To investigate how the two ventilation processes vary differently with possible changes to the boundary-layer structure, the surface moisture availability has been chosen as the parameter to change. As discussed in Chapter 2, all experiments discussed so far have been conducted over a sea-surface, and therefore moisture is freely available to be evaporated from the sea. However, cyclones regularly track over land (for example at the end of the North-Atlantic and Pacific stormtracks), and can also form over land (for example over the central United-States in the lee of the Rocky mountains). Instead of implementing a full land-surface scheme with surface energy balance, a simplified view is taken here, consistent with the idealised modelling strategy. Within the model, the surface moisture flux (Eqn. 2.10c) is adjusted thus

$$E_s = \alpha \rho C_H |\mathbf{v}_1| (q_{\text{sat}}(\theta_s) - q_1), \quad (5.14)$$

where  $\alpha \in [0, 1]$  is a parameter to describe the surface moisture availability.  $\alpha = 1$  results in the control simulation, whilst  $\alpha = 0$  would result in no surface evaporation, with values in-between representing various levels of moisture availability.

A series of experiments were conducted with various values of  $\alpha$ . Results are shown in Figure 5.12. As expected, the changes to the surface evaporation do not have a great affect on the large-scale development of the system. There is a general trend of higher EKE and lower minimum MSLP for experiments with higher values of  $\alpha$ , caused by the increased moisture leading to greater latent-heat release and so more intense systems.

Figure 5.13(a) shows the moisture ventilation plotted against  $\alpha$  for this series of experiments. It is immediately clear that modifying the surface moisture availability has affected the moisture transport in distinctly different ways. Both the advective and convective ventilation appears to

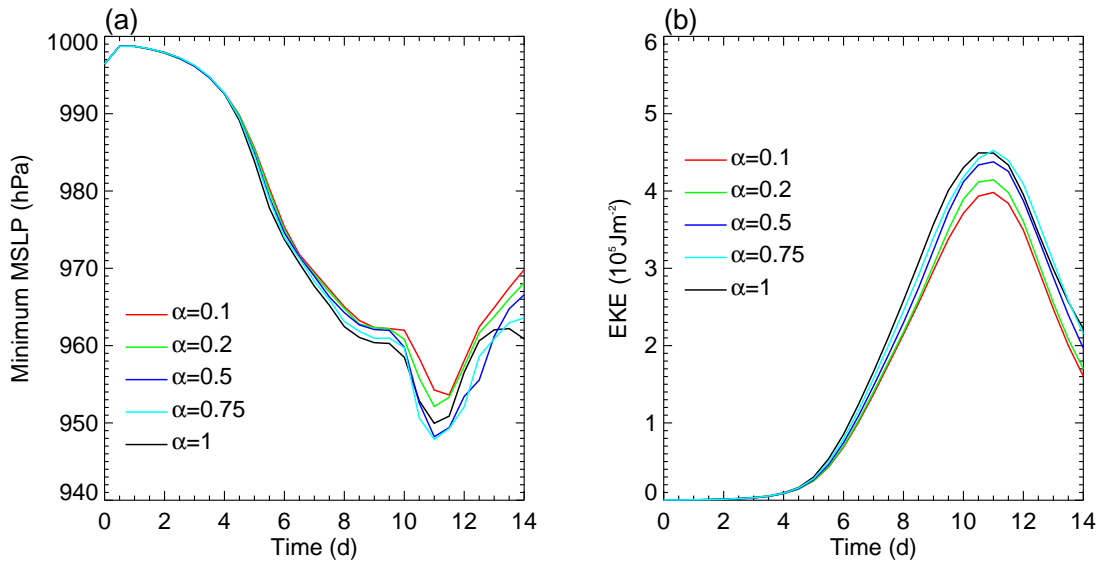


**Figure 5.12** Time series of (a) minimum sea-level pressure and (b) eddy kinetic energy, for various values of  $\alpha$  (shown on the plots).

vary linearly with  $\alpha$ , but with a different gradient. The large-scale transport reduces from its peak value of  $\approx 3.6 \times 10^{14}$  kg to a value of  $\approx 1.9 \times 10^{14}$  kg as  $\alpha$  is reduced towards zero. It appears that if there were no evaporation, the amount of ventilation would be approximately half the value when  $\alpha = 1$ . This is because, even when there is no evaporation, there is some atmospheric moisture in the initial condition, which is ventilated on the WCB. However, once this moisture has been ventilated (and eventually precipitated from the atmosphere), there is no evaporation to replace the lost moisture. Therefore, the ventilation rate drops off quickly towards the end of the life-cycle, since  $q_h$  is reduced.

The convective ventilation reacts differently however, since, as discussed in Section 5.3.2, the triggering of convection is closely linked to the surface fluxes of heat and moisture. When the surface moisture flux is zero, a single mixed layer grows above the surface and moist convection is never triggered. Therefore, there is no convective ventilation. Figure 5.13(b) shows a tephigram at the same time and location from two experiments with  $\alpha = 1$  and  $\alpha = 0.2$ . When  $\alpha = 0.2$ , there is a single mixed layer, with constant potential temperature and specific humidity extending up to  $\approx 850$  hPa. There is then a strong inversion in the potential temperature profile above this, with no convective available potential energy (CAPE), and therefore no convection can occur. When  $\alpha = 1$ , the near-surface potential temperature is unchanged, but the increased evaporation increases the

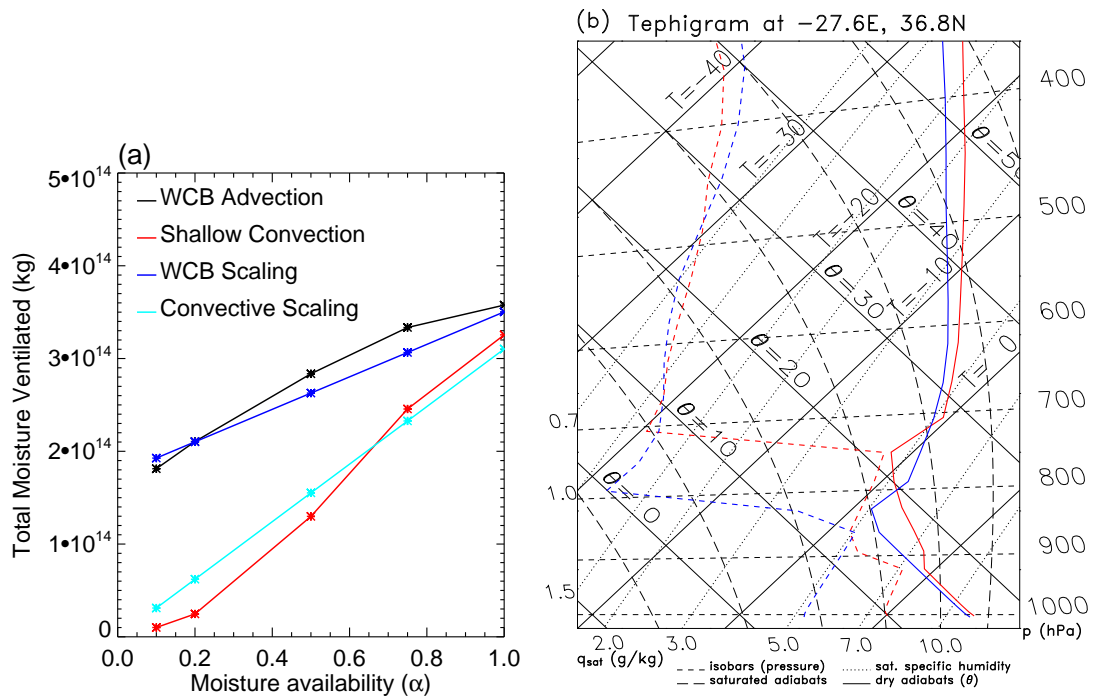


**Figure 5.13** (a) Total mass of moisture ventilated from the boundary layer ( $Q$ ) by WCB advection (black) and shallow convection (red) versus  $\alpha$ . Also shown are the results of the scaling arguments discussed in the text, for large-scale advection (dark blue) and shallow convection (light blue). (b) Tephigram in the shallow convective region at day 7, showing experiments with  $\alpha = 1$  (red) and  $\alpha = 0.2$  (blue).

moisture content of the boundary layer from  $\approx 5 \text{ gkg}^{-1}$  to  $\approx 7 \text{ gkg}^{-1}$ . A Normand's construction now shows a lifting condensation level at  $\approx 900 \text{ hPa}$ , with an area of CAPE extending up to an inversion at  $\approx 750 \text{ hPa}$ . There is therefore a well-mixed boundary layer below  $900 \text{ hPa}$ , with an area of cumulus convection above this, producing a large amount of convective ventilation.

Figure 5.13(a) also shows how the ventilation is expected to vary from the scaling arguments presented in Section 5.3, with some minor modifications. As demonstrated in Section 5.2.1, when  $\alpha = 1$  and moisture is freely available from the surface, the boundary layer RH (or equivalently  $q_h$ ) remained approximately constant throughout the life-cycle. However, as  $\alpha$  is decreased and moisture availability is restricted, the boundary-layer RH reduces as the life-cycle evolves. When  $\alpha = 0$  and there is no convective ventilation, the timescale over which the boundary-layer moisture content is expected to reduce to zero can be estimated. This is given by the ratio of the initial

moisture content to the removal rate on the WCB, i.e.

$$\tau_{\text{rem}} = \frac{\rho q_{\text{BL}} h \mathcal{A}_{\text{cyc}}}{\rho q_h w_h \mathcal{A}_{\text{wcb}}}. \quad (5.15)$$

Again,  $h \approx 1$  km and the scalings of Equation 5.3 for  $w_h$  and Equation 5.4 for  $\mathcal{A}_{\text{wcb}}$  are used.  $\mathcal{A}_{\text{cyc}}$  is the total area of boundary layer which can be ventilated by the cyclone, which is given by  $8\mathcal{A}$ . This is because the cyclone can ventilate an entire wavelength in the zonal direction ( $4\mathcal{L}$ ) and approximately  $30^\circ$  ( $2\mathcal{L}$ ) in the meridional direction. A lower bound of  $\tau_{\text{rem}} \approx 9.5$  days is found when  $q_{\text{BL}} = q_h$ , which is a reasonable assumption to make because divergent and convergent motions within the boundary layer ensure that the WCB footprint always contains any available moisture for ventilation. This value is a lower bound because subsidence and entrainment of moisture from the troposphere into the boundary layer has been neglected, although Chapter 4 demonstrated these terms in the boundary-layer moisture budget to be small compared to the WCB ascent. Therefore, it appears reasonable that over the 14 days of a life-cycle, the WCB can ventilate all moisture initially contained within the boundary layer.

The scalings presented in Section 5.3 require a constant value of all variables throughout the life-cycle, and so an average value of 40% for the boundary layer RH when  $\alpha = 0$  seems appropriate for use in Equation 5.10. When  $\alpha = 1$ , Section 5.3 has demonstrated that  $RH = RH_{\text{eq}} = 80\%$ , and so a simple linear variation of the average value of RH with  $\alpha$  gives

$$RH = RH_{\text{eq}} \frac{1 + \alpha}{2}, \quad (5.16)$$

which is used in Equation 5.10 and gives good agreement with the measured values of  $Q_{\text{wcb}}$  in Figure 5.13(a).

Section 5.3.2 discussed how the convective ventilation is proportional to the surface moisture flux, and therefore the scaling for convective ventilation, given in Equation 5.11, is modified thus:

$$\overline{w'q'}_{\text{conv}} \sim \alpha C_H |\mathbf{v}_1| (q_{\text{sat}}(\theta_s) - q_1). \quad (5.17)$$

This introduces a factor of  $\alpha$  into Equation 5.13, and Figure 5.13(a) also shows this scaling to be in good agreement with the observed values of  $Q_{\text{conv}}$ .

## 5.5 CONCLUSIONS

This chapter has discussed how boundary-layer moisture ventilation by cyclone systems is affected by large-scale and boundary-layer parameters. It has been shown from a combination of numerical experiments and scaling arguments how the moisture ventilation from advective and convective processes scales in a similar way when large-scale changes are considered. It has also been shown how boundary-layer changes can influence the two ventilation processes differently. Whilst results and scaling arguments have typically been presented in terms of the moisture ventilated from the boundary layer, it is important to note that moisture transport can be thought of as a proxy for many other processes. Chapter 4 demonstrated how the large-scale ventilation on the WCB was balanced by a convergence of moisture within the boundary layer, which is, in turn, balanced by divergence of moisture from anticyclonic regions of the cyclone wave. It was also discussed how the WCB is close to 100% efficient at converting ascending moisture into precipitation (Eckhardt *et al.*, 2004), and therefore the scalings presented for WCB ventilation also describe how the WCB precipitation is likely to vary.

A strong dependence of the moisture transport on the jet strength has been demonstrated, with  $Q \sim U_0^3$ . This is in good agreement with the results of Stohl *et al.* (2008), who demonstrate a strong dependence of poleward moisture transport and precipitation on the NAO. A positive NAO causes increased jet strength, and so the  $U_0^3$  scaling shows why there is such a strong variation with the NAO. Ruprecht *et al.* (2002) also demonstrated increased moisture transport in positive NAO conditions due to the poleward shift in the jet, which has also been demonstrated from scaling arguments, with  $Q \sim f^2$ .

Field and Wood (2007) argued for a scaling of the WCB rainrate as follows:

$$R_{\text{wcb}} = c \langle V \rangle \langle WVP \rangle, \quad (5.18)$$

where  $c$  is a constant which depends on the cyclone area, the size of the WCB inflow and the asymmetry in moisture distribution within the cyclone. The scaling arguments presented here have demonstrated consistency with this scaling. It has been shown here that

$$R_{\text{wcb}} = \tilde{c} w_h q_h, \quad (5.19)$$

where continuity implies  $\langle V \rangle \sim w_h$ , whilst  $\langle WVP \rangle \sim q_h$  since most moisture is contained within

the boundary layer, and so the effect of upper-tropospheric moisture, included in  $\langle WVP \rangle$ , is small.  $\tilde{c}$  is new constant incorporating these proportionality relations and  $c$ . It has been shown here from first principles why  $q_h$  varies according to the Clausius-Clapeyron equation, a fact noted in Field and Wood (2007).

The scaling arguments also provide clues as to how extratropical cyclones may evolve in the future. Allen and Ingram (2002) discuss how the Clausius-Clapeyron equation gives an increase in atmospheric water vapour storage of  $\approx 6.5\%K^{-1}$ , whilst energy constraints imply a mean increase in global precipitation of  $2 - 3\%K^{-1}$ . The scaling arguments presented here demonstrate that a reduction in the peak jet speed by  $1 \text{ ms}^{-1}K^{-1}$  is sufficient to reduce the precipitation increase to the energy constrained value. Thermal wind balance demonstrates that this corresponds to a reduction in the equator-pole temperature difference by  $\approx 0.3 \text{ K}$  for every  $1 \text{ K}$  of warming. The scalings also demonstrate where sensitivity to other possible changes in the atmospheric state lies. For example, climate projections also suggest that there will be a poleward shift in the storm track (Bengtsson *et al.*, 2006). This should lead to increased moisture transport and precipitation, since the Coriolis parameter will be increased. However, the scalings demonstrate that a reduction of  $\approx 0.8 \text{ ms}^{-1}$  is required to balance every  $1^\circ$  shift of the storm track poleward, and result in no change to the observed precipitation rate. This analysis assumes no change in the total number of storms, which cannot be estimated from this study of a single storm system. Whether the reduction in meridional temperature gradient results in a reduction in mean storm strength or a reduction in the total number of storms is open to debate (Sinclair and Watterson, 1999; Fyfe, 2003), although recent trends suggest that it is the cyclone frequency which is reducing (Paciorek *et al.*, 2002).

The scaling arguments have demonstrated the key physical variables that influence cyclone moisture transport and precipitation, but they also have many other potential uses. Their simplicity means that they can be used for climatological studies of moisture transport and precipitation, and also for pollution ventilation with some minor modification. Sinclair *et al.* (2010a) discussed how the large-scale advection could be used to create pollution ventilation climatologies. The present work provides a similar scaling for ventilation by moist convection, a process which has been previously shown to be an efficient method of pollution ventilation in the absence of frontal systems (Dacre *et al.*, 2007). The simple expressions can also be used as parameterisations of

moisture transport and precipitation in minimal complexity paleo-climate models, which cannot adequately resolve cyclones.

Section 5.4 has also demonstrated that although advective and convective processes are similarly constrained by the large-scale flow, they react very differently to boundary-layer changes. Sinclair *et al.* (2010a) demonstrated that the WCB was controlled entirely by the large-scale, and reasonable changes to the surface roughness had no effect on its ability to ventilate the boundary layer. This work has demonstrated a much closer link between convective ventilation and the boundary-layer structure, shown here in terms of moisture availability, but future work could investigate the dependence on the surface sensible heat and momentum fluxes. These results, combined with the results of Chapter 4, demonstrate the importance of boundary-layer processes to the mid-latitude water cycle. Convectively ventilated moisture can be transported large distances in the troposphere and even become dynamically important near the cold front, but its evolution depends heavily on the surface energy balance.

## CHAPTER 6:

# CONCLUSIONS

### 6.1 SUMMARY AND MAIN CONCLUSIONS

This thesis has investigated the interaction between mid-latitude cyclones and the atmospheric boundary layer, with the overall aim of improving understanding of the coupling between the two. This improved understanding is important for both weather and climate prediction. For example, the THORPEX-North Atlantic Waveguide and Downstream Impact Experiment (T-NAWDEX) is an experimental campaign tentatively scheduled for Autumn 2011 to observe extra-tropical cyclones and their downstream affects on short-to-medium range weather forecasts. One of the key scientific questions to be answered is (Methven, 2009, Personal comm.): Are the physical processes associated with warm-conveyor belts (WCBs) correctly captured by NWP models? Further sub-questions to facilitate answering this include: Do WCBs in the models start off with the correct humidity and temperature structure? Is the representation of turbulence correct along the WCB? Is the PV evolution correct along the WCB? How do low-level PV anomalies (generated or intensified by a WCB) evolve as they move downstream? To answer any of these questions requires knowledge of the physics and dynamics in the WCB source region, which lies within the atmospheric boundary layer. The importance of understanding the answers to these questions has been shown by Wernli (2009, Personal comm.). He demonstrated that in the ECMWF model, for the ten most extreme cases of an incorrect surface pressure pattern over Europe, the problems were due to an incorrect representation of upstream WCB processes associated with cyclones over the North-Atlantic. Improved understanding and representation of WCBs should help to improve these forecasts in the future.

In Chapter 2 a new numerical model of idealised cyclone development was created. The model initialisation was similar to previous idealised cyclone simulations which are well documented within the literature (e.g. Simmons and Hoskins, 1976; Thorncroft *et al.*, 1993; Wernli

*et al.*, 1998; Polvani and Esler, 2007). The use of the MetUM to perform the simulations adds the possibility of simulating many physical processes in a clean, idealised setting, which have only previously been investigated in intermediate-complexity numerical models or case-study scenarios. This thesis has focussed on the role of boundary-layer processes and atmospheric moisture. However, many other physical processes also have state-of-the-art parameterisation schemes in the MetUM, and the effects of these on cyclone behaviour could also be investigated using this model. For example, the problems with implementation of the radiation scheme discussed in Section 2.5.3 could be overcome by the careful addition of some net warming to the atmosphere to represent the global-scale processes not resolved within the limited area model. The detailed land-surface scheme in the MetUM could be used to run cyclone simulations over a range of different land-surface types. A coupled ocean model could be included to investigate the interaction between cyclones and the sea-surface temperature (SST). This process is often considered to be a one-way effect of the SST affecting the cyclone, as in Chapter 3. However, in reality, cyclones will also modify the SST as they pass over a region. Cyclones can also create significant ocean waves, which can propagate as swell over large distances of the Earth's oceans, for example Hanley *et al.* (2010) describe how a band of swell created by a Southern Ocean cyclone propagated to the coast of India. The MetUM's wave model could be used to investigate the creation of phenomena like this in an idealised setting. The model has also been used to study pollution ventilation from the boundary layer (Sinclair *et al.*, 2010a) and is currently being used to investigate Sting Jets (Baker, 2009, Personal comm.).

Chapter 3 discussed the interaction between the idealised cyclone and the boundary layer in dry simulations, aiming to answer the question:

- What is the mechanism by which the boundary layer spins down a mid-latitude cyclone?

The answer appears to be that a combination of the Ekman pumping and baroclinic potential vorticity (PV) mechanisms work together to maximise the spin-down. Whilst Ekman pumping will act to spin-down a barotropic vortex by vortex squashing, as demonstrated in Section 3.2.1, it also enhances the baroclinic PV mechanism. Ekman driven convergence enhances the low-level ascent on the WCB, which acts to ventilate the baroclinically generated PV from the boundary-layer, in a similar manner to passive tracers (Sinclair *et al.*, 2008) or moisture (Chapter 4). As

the baroclinically generated PV accumulates above the low centre, Ekman pumping forces the lifting of isentropes, which confines the PV anomaly into a flat shape of large horizontal extent, but trapped between the isentropes in the vertical (since in the free troposphere PV cannot cross isentropes). This shape is associated mainly with enhanced static stability, preventing communication between the upper- and lower-levels of the developing wave and reducing the growth rate. It was also established that this combined mechanism works independently of the type of cyclone and the timescale over which it evolves. Both mechanisms appeared robust and acted in a similar way in both the slowly evolving Type-A simulation and the more rapidly intensifying Type-B simulation.

Section 3.3 demonstrated the important effect that the sea-surface temperature and surface heat fluxes can have on the boundary-layer structure and PV distribution. However, unless the heat fluxes modify the boundary layer PV distribution in a location that is well placed for ventilation, they will have little effect on the large-scale cyclone development. This demonstrates why some previous studies, such as Kuo *et al.* (1991), have found differing effects from case study simulations with modified surface heat fluxes. If the surface heat fluxes are negative (positive) in a region well placed for WCB ventilation, then the lower tropospheric PV is increased (decreased) and the spin-down is enhanced (reduced).

Attempts at a PV inversion in Section 3.4 proved difficult, owing to the fact that the PV of interest tended to be in regions of large horizontal convergence, and there is presently no technique of inverting PV within the boundary layer. Despite the problems, the results provide extra support to the results of Adamson *et al.* (2006) and the Eady theory presented in Section 3.2. They demonstrated that the upper-level anomaly was enhancing the surface wave to a greater extent when the low-level PV anomaly was removed. This demonstrates that the shielding effect is at least occurring, although cannot determine the magnitude of the effect.

Chapter 4 included the effects of moisture into the simulations, investigating the question:

- How does the cyclone boundary layer link surface moisture fluxes to ventilation into the free troposphere?

The use of a boundary-layer budgeting technique demonstrated that the greatest input of moisture

from the surface was behind the cold front, in the cold-air outbreak, as the boundary-layer air flowed quickly from the north over a warmer sea-surface. Approximately half of this input was locally ventilated due to shallow convection above this region. The remainder was transported within the cyclone boundary layer, from the high-pressure part of the wave where the horizontal flow was divergent, to the low-pressure part of the wave where the horizontal flow was convergent. The moisture converged under the WCB and was then ventilated from the boundary layer by large-scale ascent.

Sections 4.2 and 4.3 documented how the structure and evolution of the boundary layer changed between the dry and moist simulations. The overall structure remained similar, with large areas of stable and unstable boundary layer, forced by large-scale advection of heat by the cyclone system. However, the addition of moisture created sub-categories within these regions, with different types of capping cloud being formed depending on the moisture availability. Behind the cold front and in the cold-air outbreak, shallow cumulus clouds were formed as the boundary-layer air flowed quickly from the north over a warmer sea-surface. In the very centre of the high pressure, thermal advection was weak and a deep, single mixed layer could grow, similar to the dry simulations. Within the WCB region, the boundary layer was stable and close to saturation, with low-level cloud or fog being formed.

Section 4.5 discussed how the ventilated moisture was transported within the free troposphere. The large-scale ascent on the WCB transported moisture polewards and ascended to  $\sim 7$  km, before being precipitated back to the surface. The moisture ventilated by shallow convection stayed much lower within the atmosphere ( $\sim 3$  km) and was transported eastwards with the jet, converging near the cold-front several days later. This moisture was also transported slightly polewards and could either act to modify the tropospheric humidity structure, or would be precipitated back to the surface in showers behind the front and frontal precipitation.

Chapter 5 investigated further the two methods identified for boundary-layer moisture ventilation, addressing the question:

- What factors control the moisture transport within mid-latitude cyclones?

Variation of key large-scale parameters and scaling arguments demonstrated an exponential de-

pendence of moisture transport on the absolute temperature, due to the Clausius-Clapeyron relation. Strong dependence on the meridional temperature gradient was also found, with a  $Q \sim U_0^3$  scaling, whilst slightly weaker dependences on the Coriolis parameter and vertical temperature gradient were also found. The relative humidity (RH) was found to have very little control over the moisture transport, and this was shown to be due to the fact that evaporation and precipitation processes within the cyclone system could act to restore an equilibrium RH distribution over a short timescale. It was also demonstrated that large-scale parameters exert similar controls over ventilation by advective and convective processes. Within the cyclone system, the convection is ultimately driven by the same large-scale processes that govern the WCB strength, meaning that modification of large-scale parameters affects both processes in the same way. However, the importance of the boundary layer for triggering and regulating convection was demonstrated by a series of experiments with modified surface moisture flux. In this situation, the two ventilation processes did react differently. The WCB structure was largely unchanged by the modified surface flux, with the ventilation only being affected by the limited supply of moisture from the boundary layer. However, the convective process was dramatically changed, with convection being unable to trigger as the surface fluxes were reduced.

This final chapter of work is useful in consideration of how cyclogenesis might change as the climate evolves. The scaling arguments presented demonstrate how apparent discrepancies in projected rainfall amounts (Allen and Ingram, 2002) can be accounted for with only a very minor reduction in the meridional temperature gradient. A  $1 \text{ ms}^{-1} \text{K}^{-1}$  reduction in the peak jet speed is sufficient to reduce the  $\approx 6.5\% \text{K}^{-1}$  increase in precipitation expected from Clausius-Clapeyron arguments to the global energy balance constrained value of  $2 - 3\% \text{K}^{-1}$ . This results does not require any change in the frequency of cyclone events.

## **6.2 FUTURE WORK**

There is great potential to expand upon the work presented in this thesis, and many different directions which future work could take. This thesis has presented an idealised modelling approach, utilising clean and easily changeable experiments to deduce results which should be generic and applicable to all mid-latitude cyclones. Therefore, one obvious next step is to investigate case-

studies or composites of real cyclone systems. The diagnostic techniques developed for analysing Ekman pumping and baroclinic PV generation, and the boundary-layer budgeting techniques, are easily applicable to standard NWP or reanalysis data.

Possibly of greater importance for understanding moisture inflow to WCBs is the possibility of obtaining suitable observational data. Most cyclogenesis events occur over the ocean, making this only possible during field campaigns. However, this is one topic being investigated as part of the pilot project for T-NAWDEX (Methven, 2009, Personal comm.). A series of flights will take place in late 2009, with several of the flights planned to transect a WCB and measure the horizontal fluxes of moisture within the boundary layer. This should hopefully provide enough data to construct several of the budget terms in the WCB region, allowing both qualitative and quantitative comparison to be made to the idealised work presented here, and budget calculations from hindcast runs of the observed events.

Recent work by Hewson (2009, Personal comm.) has demonstrated a link between sea-surface temperature anomalies and precipitation delivered from cyclone WCBs, suggesting that SST anomalies can modify boundary layer air as it flows polewards, modifying the moisture content of the air and ultimately the precipitation delivered. Some idealised experiments using the simulations presented in Chapter 2 could be constructed with carefully placed SST anomalies, allowing the magnitude and location of the SST anomaly to be varied and its effect on the WCB precipitation uncovered. Some preliminary investigations suggest that when the SST gradient is enhanced, i.e. there is a warm anomaly in the SST to the south and a cold anomaly in the SST to the north, the WCB precipitation is enhanced. This enhancement does not appear from any increase in the cyclone intensity, since the atmospheric baroclinicity remains unchanged. It is due to an SST state which is out of balance with the atmosphere, moistening the boundary-layer air, resulting in a lower cloud base and increased precipitation reaching the surface.

Finally, there are significant climate implications from the water cycle work presented in Chapters 4 and 5. Understanding how cyclones will change as the climate changes is of significant socio-economic importance, due to their ability to threaten life and damage property. The moisture budget analysis presented here could be applied to simulations of the future climate, providing quantitative analysis of how the cyclone moisture cycle is modified. This will lead to a better understanding of the changes in precipitation patterns that can be expected. It will also

provide guidance on which areas of climate models are the most important for accurate representation of cyclone precipitation processes and the water cycle, demonstrating in which areas model improvements are likely to lead to the most significant climate projection improvements. This has been highlighted in this study by the importance of convective processes in boundary-layer moisture ventilation. Accurate representation of the convective ventilation is not only important for what the convection ventilates, but also feeds back onto what the WCB can ventilate by removing moisture (or other tracers) from the source region. Therefore, even if representation of the WCB was perfect, if the convection was wrong then one could not hope to obtain the correct outflow from the WCB because the inflow would not be correct. Linkages like this are important for understanding how climate models behave, and also how the real atmosphere behaves.

**APPENDIX A:**  
**NOMENCLATURE**

**A.1 SYMBOLS AND PHYSICAL CONSTANTS**

$A$	Area of a surface [ $\text{m}^2$ ]
$\mathcal{A}$	Cyclone scaling area [ $\text{m}^2$ ]
$a$	Radius of the Earth [6371 km]
$C_D$	Drag coefficient
$C_H$	Stanton number
$C(T)$	Empirical solution to the Clausius-Clapeyron equation [hPa]
$c_p$	Specific heat capacity of air at constant pressure [ $1004 \text{ JK}^{-1}\text{kg}^{-1}$ ]
$c$	Scaling constant from Field and Wood (2007) [ $\text{m}^{-1}$ ]
$\tilde{c}$	Modified scaling constant
$D^*$	Moisture regime parameter
$E$	Turbulent moisture flux [ $\text{kgm}^{-2}\text{s}^{-1}$ ]
$\mathcal{E}$	Shape parameter
$e$	Partial pressure of water vapour in air [Pa]
$F_B$	Surface buoyancy flux [ $\text{kgm}^{-1}\text{s}^{-3}$ ]
$f$	Coriolis parameter [ $\text{s}^{-1}$ ]
$f_{m,h}$	Stability function for momentum/heat
$G_B$	PV generation by baroclinic friction [ $\text{Kkg}^{-1}\text{m}^2\text{s}^{-2}$ ]
$G_H$	PV generation by surface sensible heat fluxes [ $\text{Kkg}^{-1}\text{m}^2\text{s}^{-2}$ ]
$g$	Gravitational acceleration [ $9.81 \text{ ms}^{-2}$ ]
$H$	Turbulent flux of sensible heat [ $\text{Wm}^{-2}$ ]
$\mathcal{H}$	Tropopause height [m]
$h$	Boundary-layer depth [m]
$K_{m,h}$	Eddy diffusivity for momentum/heat [ $\text{m}^2\text{s}^{-1}$ ]

$k$	Zonal wavenumber [ $\text{m}^{-1}$ ]
$\mathbf{k}$	Unit vector in the $z$ -direction
$L_{\text{Ro}}$	Rossby radius of deformation [m]
$L$	Obukhov Length [m]
$L_y$	Jet width [3000 km]
$\mathcal{L}_{m,h}$	Neutral mixing length for momentum/heat [m]
$\mathcal{L}$	Cyclone scaling length [m]
$l_m$	Mixing lengthscale for momentum [m]
$m$	zonal wavenumber [6]
$N^2$	Static stability [ $\text{s}^{-2}$ ]
$N_t$	Tropospheric Brunt-Väisälä frequency [ $1.16 \times 10^{-2} \text{ s}^{-1}$ ]
$N_s$	Stratospheric Brunt-Väisälä frequency [ $2.32 \times 10^{-2} \text{ s}^{-1}$ ]
$\mathbf{n}$	Unit normal to a surface
$\tilde{\mathbf{n}}$	Normal to a surface
$PV$	Potential Vorticity [ $\text{Kkg}^{-1}\text{m}^2\text{s}^{-1}$ ]
$Pr$	Prandtl number
$p$	Pressure [Pa]
$p_0$	Surface pressure [1000 hPa]
$QGVP'$	Quasi-geostrophic potential vorticity perturbation [ $\text{s}^{-1}$ ]
$Q$	Total mass of moisture ventilated by a life-cycle [kg]
$q$	Specific humidity [ $\text{kgkg}^{-1}$ ]
$q_v$	Specific humidity of water vapour in air [ $\text{kgkg}^{-1}$ ]
$q_l$	Specific humidity of liquid water in air [ $\text{kgkg}^{-1}$ ]
$q_f$	Specific humidity of frozen water in air [ $\text{kgkg}^{-1}$ ]
$R$	Ideal gas constant for dry air [ $287 \text{ JK}^{-1}\text{kg}^{-1}$ ]
$Ri$	Gradient Richardson number
$Ri_b$	Bulk Richardson number
$RH$	Relative humidity
$RH_0$	Maximum value of surface relative humidity [80%]
$R_{\text{wcb}}$	Warm-conveyor belt precipitation rate [ $\text{mmday}^{-1}$ ]
$\mathbf{S}^u$	Frictional force per unit mass [ $\text{ms}^{-2}$ ]

$S^\theta$	Source or sink of heat [ $\text{Ks}^{-1}$ ]
$S^q$	Source or sink of water [ $\text{s}^{-1}$ ]
$S$	Arbitrary surface to integrate over [ $\text{m}^2$ ]
$s$	Source or sink of moisture from microphysics [ $\text{kgm}^{-3}\text{s}^{-1}$ ]
$T$	Temperature [K]
$\hat{T}$	Temperature perturbation maximum [1 K]
$T'$	Temperature perturbation [K]
$T_0$	Surface temperature at $\hat{\phi}$ [280 K]
$\mathcal{T}$	Timescale of life-cycle [14 days]
$t$	Time [s]
$U$	Jet speed at $\mathcal{H}$ [ $\text{ms}^{-1}$ ]
$U_0$	Peak jet speed [ $45 \text{ms}^{-1}$ ]
$u$	Zonal velocity [ $\text{ms}^{-1}$ ]
$\mathbf{u}$	3D wind vector: $(u, v, w)$ [ $\text{ms}^{-1}$ ]
$u_*$	Friction velocity [ $\text{ms}^{-1}$ ]
$V_{\text{sc}}$	Stratocumulus scaling velocity [ $\text{ms}^{-1}$ ]
$V$	Near-surface windspeed [ $\text{ms}^{-1}$ ]
$v$	Meridional velocity [ $\text{ms}^{-1}$ ]
$\mathbf{v}$	2D velocity vector: $(u, v)$ [ $\text{ms}^{-1}$ ]
$v_*$	Surface scaling velocity [ $\text{ms}^{-1}$ ]
$WVP$	Water vapour path [ $\text{kgm}^{-2}$ ]
$w$	Vertical velocity [ $\text{ms}^{-1}$ ]
$w_*$	Convective velocity scale [ $\text{ms}^{-1}$ ]
$w_s$	Vertical scaling velocity [ $\text{ms}^{-1}$ ]
$w_e$	Entrainment velocity [ $\text{ms}^{-1}$ ]
$w_{\text{Ek}}$	Ekman pumping velocity [ $\text{ms}^{-1}$ ]
$x$	Zonal distance [m]
$y$	Meridional distance [m]
$z$	Height above surface [m]
$z_{0m,h}$	Roughness length for momentum/heat [m]
$z_h$	Depth of boundary layer scheme operation [m]

$z_{\text{par}}$	Depth of surface based mixed layer [m]
$z_{\text{ml}}$	Depth of cloud top driven turbulence [m]
$z_T$	Temperature scale height [13 km]
$z_q$	Moisture scale height [12 km]
$\alpha_c$	Charnock parameter [0.011]
$\alpha$	Moisture availability parameter
$\gamma_t$	Velocity scaling parameter
$\gamma_h$	Counter-gradient term [ $\text{Km}^{-1}$ ]
$\zeta$	Absolute vorticity [ $\text{s}^{-1}$ ]
$\theta$	Potential temperature [K]
$\theta_v$	Virtual potential temperature [K]
$\theta_w$	Wet-bulb potential temperature [K]
$\kappa$	Von-Karman constant [0.4]
$\Lambda$	Longitude
$\lambda$	Latent heat of condensation of water [ $2.5 \times 10^6 \text{ Jkg}^{-1}$ at 273 K]
$\xi$	Relative Vorticity [ $\text{s}^{-1}$ ]
$\Pi$	Exner pressure
$\rho$	Density of air [ $\text{kgm}^{-3}$ ]
$\sigma$	Eady growth rate [ $\text{s}^{-1}$ ]
$\tau$	Turbulent stress [ $\text{Nm}^{-2}$ ]
$\Phi_{m,h}$	Integrated Monin-Obukhov stability function for momentum/heat
$\Phi$	Geopotential height [m]
$\phi_{m,h}$	Monin-Obukhov stability function for momentum/heat
$\phi$	Latitude
$\hat{\phi}$	Jet Latitude [45N]
$\chi$	Arbitrary Reynolds averaged variable
$\psi$	Streamfunction [ $\text{m}^2\text{s}^{-1}$ ]
$\Omega$	Rotation rate of Earth [ $7.292 \times 10^{-5} \text{ s}^{-1}$ ]
$\omega$	Frequency [ $\text{s}^{-1}$ ]

## A.2 MATHEMATICAL OPERATORS

$\nabla$	3D gradient operator: $(\frac{\partial}{\partial x}, \frac{\partial}{\partial y}, \frac{\partial}{\partial z})$
$\nabla_2$	2D gradient operator: $(\frac{\partial}{\partial x}, \frac{\partial}{\partial y})$
$\frac{D}{Dt}$	Material derivative: $\frac{\partial}{\partial t} + \mathbf{u} \cdot \nabla$
$\bar{x}$	Grid-box mean value of a quantity
$x'$	Fluctuation of quantity from the mean state
$ \mathbf{x} $	$l^2$ -norm of a vector: $\sqrt{\sum_{n=1}^N x_n^2}$
$\langle x \rangle$	Zonal mean of a quantity
$[x]$	Boundary-layer depth-average of a quantity: $h^{-1} \int_0^h x dz$
$\hat{x}$	Boundary-layer depth-integral of a quantity: $h[x]$
$\langle x \rangle$	Quantity averaged over a 2000 km radius circle centred on the minimum sea-level pressure

## A.3 SUBSCRIPTS AND SUPERSCRIPTS

$x_{x,y,z}$	$x$ , $y$ or $z$ component of a vector
$x_g$	Geostrophic value of a quantity
$x_0$	Reference/surface/initial value of a quantity
$x_{\text{sat}}$	Value of a quantity at saturation
$x_s$	Surface value of a quantity
$x_{m,h}$	Momentum/heat-flux related quantity
$x_1$	First model level value of a quantity
$x_h$	Quantity evaluated at the boundary-layer top
$x^{\text{surf}}$	Surface driven quantity
$x^{\text{sc}}$	Cloud-top driven quantity
$x_{\text{eq}}$	Equilibrium value of a quantity
$x_{\text{wcb}}$	Warm conveyor belt value of a quantity
$x_{\text{conv}}$	Shallow-convection related value of a quantity

## A.4 ABBREVIATIONS

CAPE	Convective available potential energy
CCB	Cold-conveyor belt
ECMWF	European Centre for Medium Range Weather Forecasting
EKE	Eddy kinetic energy
IGCM	Intermediate General Circulation Model
LLJ	Low-level jet
MetUM	Meteorological Office Unified Model
MSLP	Mean sea-level pressure
NAO	North-Atlantic Oscillation
NCEP	National Centre for Environmental Prediction
NWP	Numerical Weather Prediction
PV	Potential Vorticity
QG	Quasi-geostrophic
RH	Relative humidity
SST	Sea-surface temperature
TKE	Turbulent kinetic energy
WCB	Warm-conveyor belt

# BIBLIOGRAPHY

- Adamson, D. S., Belcher, S. E., Hoskins, B. J., and Plant, R. S. (2006). Boundary-layer friction in midlatitude cyclones. *Q. J. R. Meteorol. Soc.*, **132**, 101–124.
- Ahmadi-Givi, F., Craig, G. C., and Plant, R. S. (2004). The dynamics of a midlatitude cyclone with very strong latent-heat release. *Q. J. R. Meteorol. Soc.*, **130**, 295–323.
- Allen, M. and Ingram, W. (2002). Constraints on future changes in climate and the hydrologic cycle. *Nature*, **419**, 224–232.
- Anthes, R. A. and Keyser, D. (1979). Tests of a fine-mesh model over Europe and the United States. *Mon. Weather Rev.*, **107**, 963–984.
- Arakawa, A. and Lamb, V. R. (1977). Computational design of the basic dynamical processes of the UCLA general circulation model. *Methods in Comp. Phys.*, **17**, 174–265.
- Balasubramanian, G. and Garner, S. T. (1997). The Role of Momentum Fluxes in Shaping the Life Cycle of a Baroclinic Wave. *J. Atmos. Sci.*, **54**, 510–533.
- Barry, L., Craig, G. C., and Thuburn, J. (2002). Poleward heat transport by the atmospheric heat engine. *Nature*, **415**, 774–777.
- Beare, R. J. (2007). Boundary layer mechanisms in extratropical cyclones. *Q. J. R. Meteorol. Soc.*, **133**, 503–515.
- Beare, R. J., Thorpe, A. J., and White, A. A. (2003). The predictability of extratropical cyclones: Nonlinear sensitivity to localized potential-vorticity perturbations. *Q. J. R. Meteorol. Soc.*, **129**, 219–237.
- Beare, R. J., MacVean, M. K., Holtslag, A. A. M., Cuxart, J., Esau, I., Golaz, J.-C., Jimenez, M. A., Khairoutdinov, M., Kosovic, B., Lewellen, D., Lund, T. S., Lundquist, J. K., McCabe, A., Moene, A. F., Noh, Y., Raasch, S., and Sullivan, P. (2006). An intercomparison of large-eddy simulations of the stable boundary layer. *Boundary-Layer Meteorol.*, **118**, 247–272.

- Becker, A., Kraus, H., and Ewenz, C. M. (1996). Frontal substructures within the planetary boundary layer. *Boundary-Layer Meteorol.*, **78**, 165–190.
- Beljaars, A. C. M. and Holtslag, A. A. M. (1991). Flux parameterization over land surfaces for atmospheric models. *J. Appl. Meteorol.*, **30**, 327–341.
- Beljaars, A. C. M. and Viterbo, P. (1998). Role of the boundary layer in a numerical weather prediction model. In A. A. M. Holtslag and P. G. Duynkerke, editors, *Clear and Cloudy Boundary Layers*, pages 287–304, Royal Netherlands Academy of Arts and Sciences, Amsterdam.
- Bengtsson, L., Hodges, K. I., and Roeckner, E. (2006). Storm tracks and climate change. *J. Climate*, **19**, 3518–3543.
- Berger, B. W. and Friehe, C. A. (1995). Boundary-layer structure near the cold front of a marine cyclone during “ERICA”. *Boundary-Layer Meteorol.*, **73**, 227–253.
- Bjerknes, J. (1919). On the structure of moving cyclones. *Geofys. Publ.*, **1**(2), 1–8.
- Bjerknes, J. and Solberg, H. (1922). Life cycles of cyclones and the polar front theory of atmospheric circulation. *Geofys. Publ.*, **3**(1), 1–18.
- Blumen, W. (2001). Some Effects of an Ekman Boundary-Layer Parameterization on Various Models of Atmospheric Flow. *Boundary-Layer Meteorol.*, **99**, 509–519.
- Bolton, D. (1980). The computation of equivalent potential temperature. *Mon. Weather Rev.*, **108**, 1046–1053.
- Bracegirdle, T. J. and Gray, S. L. (2009). The dynamics of a polar low assessed using potential vorticity inversion. *Q. J. R. Meteorol. Soc.*, **135**, 880–893.
- Branscome, L. E., Gutowski, W. J., and Stewart, D. A. (1989). Effect of surface fluxes on the nonlinear development of baroclinic waves. *J. Atmos. Sci.*, **46**, 460–475.
- Bretherton, F. P. (1966). Critical layer instability in baroclinic flows. *Q. J. R. Meteorol. Soc.*, **92**, 325–334.
- Brown, A. R., Beare, R. J., Edwards, J. M., Lock, A. P., Keogh, S. J., Milton, S. F., and Walters, D. N. (2008). Upgrades to the boundary-layer scheme in the Met Office numerical weather prediction model. *Boundary-Layer Meteorol.*, **128**, 117–132.

- Browning, K. A. (1985). Conceptual models of precipitation systems. *Meteor. Mag.*, **114**, 293–319.
- Burt, S. D. and Mansfield, D. A. (1988). The great storm of 15-16 October 1987. *Weather*, **43**, 90–114.
- Businger, J. A. and Charnock, H. (1983). Boundary layer structure in relation to larger-scale flow: Some remarks on the JASIN observations. *Phil. Trans. R. Soc. Lond. A*, **308**, 445–449.
- Card, P. A. and Barcilon, A. (1982). The Charney stability problem with a lower Ekman layer. *J. Atmos. Sci.*, **39**, 2128–2137.
- Carlson, T. N. (1980). Airflow through midlatitude cyclones and the comma cloud pattern. *Mon. Weather Rev.*, **108**, 1498–1509.
- Charney, J. G. (1947). The dynamics of long waves in a baroclinic westerly current. *J. Meteor.*, **4**, 135–162.
- Charney, J. G. (1955). The use of the primitive equations of motion in numerical prediction. *Tellus*, **7**, 22–26.
- Charney, J. G. and Phillips, N. A. (1953). Numerical integration of the quasi-geostrophic equations for barotropic and simple baroclinic flows. *J. Meteor.*, **10**, 71–99.
- Charnock, H. (1955). Wind stress on a water surface. *Q. J. R. Meteorol. Soc.*, **81**, 639–640.
- Clark, P. A., Browning, K. A., and Wang, C. (2005). The sting at the end of the tail: Model diagnostics of fine-scale three-dimensional structure of the cloud head. *Q. J. R. Meteorol. Soc.*, **131**, 2263–2292.
- Cooper, I. M., Thorpe, A. J., and Bishop, C. H. (1992). The role of diffusive effects on potential vorticity in fronts. *Q. J. R. Meteorol. Soc.*, **118**, 629–647.
- Cullen, M. J. P. (1993). The unified forecast/climate model. *Meteor. Mag.*, **122**, 81–94.
- Dacre, H. F., Gray, S. L., and Belcher, S. E. (2007). A case study of boundary layer ventilation by convection and coastal processes. *J. Geophys. Res.*, **112**, D17106.

- Davies, T., Cullen, M. J. P., Malcolm, A. J., Mawson, M. H., Staniforth, A., White, A. A., and Wood, N. (2005). A new dynamical core for the Met Office's global and regional modelling of the atmosphere. *Q. J. R. Meteorol. Soc.*, **131**, 1759–1782.
- Davis, C. A. and Emanuel, K. A. (1991). Potential vorticity diagnostics of cyclogenesis. *Mon. Weather Rev.*, **119**, 1929–1953.
- Eady, E. T. (1949). Long waves and cyclone waves. *Tellus*, **1**, 33–52.
- Eckhardt, S., Stohl, A., Wernli, H., James, P., Forster, C., and Spichtinger, N. (2004). A 15-year climatology of warm conveyor belts. *J. Climate*, **17**, 218–237.
- Edwards, J. M. and Slingo, A. (1996). Studies with a flexible new radiation code. I: Choosing a configuration for a large-scale model. *Q. J. R. Meteorol. Soc.*, **122**, 689–719.
- Ekman, V. W. (1905). On the influence of the Earth's rotation on ocean currents. *Arkiv. Math. Astron. O. Fysik.*, **2**(11), 1–53.
- Emanuel, K., Fantini, M., and Thorpe, A. (1987). Baroclinic instability in an environment of small stability to slantwise moist convection. Part I: Two-dimensional models. *J. Atmos. Sci.*, **44**, 1559–1573.
- Ertel, H. (1942). Ein neuer hydrodynamischer wirbelsatz. *Meteor. Z.*, **59**, 277–281.
- Farrell, B. (1984). Modal and non-modal baroclinic waves. *J. Atmos. Sci.*, **41**, 668–673.
- Farrell, B. (1985). Transient growth of damped baroclinic waves. *J. Atmos. Sci.*, **42**, 2718–2727.
- Field, P. R. and Wood, R. (2007). Precipitation and Cloud Structure in Midlatitude Cyclones. *J. Climate*, **20**, 233–254.
- Field, P. R., Gettelman, A., Neale, R. B., Wood, R., Rasch, P. J., and Morrison, H. (2008). Midlatitude cyclone compositing to constrain climate model behaviour using satellite observations. *J. Climate*, **21**, 5887–5903.
- Fink, A. H., Brücher, T., Ermert, V., Krüger, A., and Pinto, J. G. (2009). The European storm Kyrill in January 2007: Synoptic evolution, meteorological impacts and some considerations with respect to climate change. *Nat. Hazards Earth Syst. Sci.*, **9**, 405–423.

- Fritsch, J. M. and Chappell, C. F. (1980). Numerical prediction of convectively driven mesoscale pressure systems. Part I: Convective parameterisation. *J. Atmos. Sci.*, **37**, 1722–1733.
- Fyfe, J. C. (2003). Extratropical southern hemisphere cyclones: Harbingers of climate change? *J. Climate*, **16**, 2802–2805.
- Grant, A. L. M. (2001). Cloud-base fluxes in the cumulus-capped boundary layer. *Q. J. R. Meteorol. Soc.*, **127**, 407–421.
- Grant, A. L. M. and Brown, A. R. (1999). A similarity hypothesis for shallow-cumulus transports. *Q. J. R. Meteorol. Soc.*, **125**, 1913–1936.
- Gray, S. L. and Dacre, H. F. (2006). Classifying dynamical forcing mechanisms using a climatology of extratropical cyclones. *Q. J. R. Meteorol. Soc.*, **132**, 1119–1137.
- Greenspan, H. P. (1969). *The theory of rotating fluids*. Cambridge University Press, Cambridge.
- Gregory, D. and Rowntree, P. R. (1990). A mass flux convection scheme with representation of cloud ensemble characteristics and stability-dependent closure. *Mon. Weather Rev.*, **118**, 1483–1506.
- Gutowski, W. J. and Jiang, W. (1998). Surface-flux regulation of the coupling between cumulus convection and baroclinic waves. *J. Atmos. Sci.*, **55**, 940–953.
- Gutowski, W. J., Branscome, L. E., and Stewart, D. A. (1992). Life cycles of moist baroclinic eddies. *J. Atmos. Sci.*, **49**, 306–319.
- Gyakum, J. and Danielson, R. (2000). Analysis of meteorological precursors to ordinary and explosive cyclogenesis in the western North Pacific. *Mon. Weather Rev.*, **128**, 851–863.
- Hanley, K. E., Belcher, S. E., and Sullivan, P. P. (2010). A global climatology of wind-wave interaction. *J. Phys. Oceanogr.* doi: 10.1175/2010JPO4377.1.
- Harold, T. W. (1973). Mechanisms influencing the distribution of precipitation within baroclinic disturbances. *Q. J. R. Meteorol. Soc.*, **99**, 232–251.
- Hewson, T. D. (1998). Objective fronts. *Meteorol. Appl.*, **5**, 37–65.

- Holtstlag, A. A. M. and Boville, B. A. (1993). Local versus nonlocal boundary-layer diffusion in a global climate model. *J. Climate*, **6**, 1825–1842.
- Holtstlag, A. A. M. and Moeng, C.-H. (1991). Eddy diffusivity and countergradient transport in the convective atmospheric boundary layer. *J. Atmos. Sci.*, **48**, 1690–1698.
- Hoskins, B. J. and Simmons, A. J. (1975). A multilayer spectral model and the semi-implicit method. *Q. J. R. Meteorol. Soc.*, **101**, 637–655.
- Hoskins, B. J., McIntyre, M. E., and Robertson, A. W. (1985). On the use and significance of isentropic potential vorticity maps. *Q. J. R. Meteorol. Soc.*, **111**, 877–946.
- James, I. N. (1994). *Introduction to Circulating Atmospheres*. Cambridge Atmospheric and Space Science Series. Cambridge University Press, Cambridge.
- Jones, B. (1992). *Effects of Physical Processes in Baroclinic Waves*. Ph.D. thesis, University of Reading.
- Kuo, Y.-H., Reed, R. J., and Low-Nam, S. (1991). Effects of Surface Energy Fluxes during the Early Development and Rapid Intensification Stages of Seven Explosive Cyclones in the Western Atlantic. *Mon. Weather Rev.*, **119**, 457–476.
- Levy, G. (1989). Surface dynamics of observed maritime fronts. *J. Atmos. Sci.*, **46**, 1219–1232.
- Lock, A. P. (2001). The numerical representation of entrainment in parametrizations of boundary layer turbulent mixing. *Mon. Weather Rev.*, **129**, 1148–1163.
- Lock, A. P. (2007). The parametrization of boundary layer processes. *Unified Model Documentation Paper*, **24**.
- Lock, A. P., Brown, A. R., Bush, M. R., Martin, G. M., and Smith, R. N. B. (2000). A New Boundary Layer Mixing Scheme. Part I: Scheme Description and Single-Column Model Tests. *Mon. Weather Rev.*, **128**, 3187–3199.
- Mahrt, L. (1991). Boundary-layer moisture regimes. *Q. J. R. Meteorol. Soc.*, **117**, 151–176.
- Martin, J. E. (2006). *Mid-Latitude Atmospheric Dynamics*. Wiley, Chichester.

- Meehl, G. A., Stocker, T. F., Collins, W. D., Friedlingstein, P., Gaye, A. T., Gregory, J. M., Kitoh, A., Knutti, R., Murphy, J. M., Noda, A., Raper, S. C. B., Watterson, I. G., Weaver, A. J., and Zhao, Z.-C. (2007). Global climate projections. In *Climate Change 2007: The Physical Science Basis*. Cambridge University Press, Cambridge, United Kingdom and New York, NY, USA.
- Monin, A. S. and Obukhov, A. M. (1954). Basic laws of turbulent mixing in the ground layer of the atmosphere. *Trudy Geofiz. Inst. Akad. Nauk SSSR*, **24**(151), 163–187.
- Natural Environment Research Council (2009). The changing water cycle programme. Technical report, <http://www.nerc.ac.uk/research/programmes/cwc/aims.asp>.
- Neiman, P. J. and Shapiro, M. A. (1993). The Life Cycle of an Extratropical Marine Cyclone. Part I: Frontal-Cyclone Evolution and Thermodynamic Air-Sea Interaction. *Mon. Weather Rev.*, **121**, 2153–2176.
- Neiman, P. J., Shapiro, M. A., Donall, E. G., and Kreitzberg, C. W. (1990). Diabatic Modification of an Extratropical Marine Cyclone Warm Sector by Cold Underlying Water. *Mon. Weather Rev.*, **118**, 1576–1590.
- Nuss, W. A. (1989). Air-sea interaction influences on the structure and intensification of an idealized marine cyclone. *Mon. Weather Rev.*, **117**, 351–369.
- Paciorek, C. J., Risbey, J. S., Ventura, V., and Rosen, R. D. (2002). Multiple indices of Northern Hemisphere cyclone activity, winters 1949-99. *J. Climate*, **15**, 1573–1590.
- Pavan, V., Hall, N., Valdes, P., and Blackburn, M. (1999). The importance of moisture distribution for the growth and energetics of mid-latitude systems. *Ann. Geophys.*, **17**, 242–256.
- Pedlosky, J. (1979). *Geophysical Fluid Dynamics*. Springer, New York.
- Petterssen, S. and Smebye, S. J. (1971). On the development of extratropical cyclones. *Q. J. R. Meteorol. Soc.*, **97**, 457–482.
- Plant, R. S. and Belcher, S. E. (2007). Numerical simulation of baroclinic waves with a parameterized boundary layer. *J. Atmos. Sci.*, **64**, 4383–4399.
- Plant, R. S., Craig, G. C., and Gray, S. L. (2003). On a threefold classification of extratropical cyclogenesis. *Q. J. R. Meteorol. Soc.*, **129**, 2989–3012.

- Polvani, L. M. and Esler, J. G. (2007). Transport and mixing of chemical air masses in idealized baroclinic life cycles. *J. Geophys. Res.*, **112**, D23102.
- Reed, R. J. and Danielsen, E. F. (1959). Fronts in the vicinity of the tropopause. *Arch. Meteorol. Geophys. Bioklim.*, **A11**, 1–17.
- Reed, R. J., Grell, G. A., and Kuo, Y.-H. (1993). The ERICA IOP 5 storm. Part II: Sensitivity tests and further diagnosis based on model output. *Mon. Weather Rev.*, **121**, 1595–1612.
- Rossby, C.-G. (1940). Planetary flow patterns in the atmosphere. *Q. J. R. Meteorol. Soc.*, **66**, 68–87. Suppl.
- Rotunno, R. and Bao, J.-W. (1996). A Case Study of Cyclogenesis Using a Model Hierarchy. *Mon. Weather Rev.*, **124**, 1051–1066.
- Rotunno, R. and Fantini, M. (1989). Petterssen's "Type B" cyclogenesis in terms of discrete, neutral Eady modes. *J. Atmos. Sci.*, **46**, 3599–3604.
- Ruprecht, E., Schröder, S., and Ubl, S. (2002). On the relation between NAO and water vapour transport towards Europe. *Meteor. Z.*, **11**, 395–401.
- Shapiro, M. A. and Keyser, D. (1990). Fronts, jet streams and the tropopause. In *Extratropical Cyclones: The Erik Palmén Memorial Volume*, pages 167–191. Amer. Meteorol. Soc., Boston.
- Shapiro, M. A., Wernli, H., Bao, J.-W., Methven, J., Zou, X., Neiman, P., Donall-Grell, E., Doyle, J. D., and Holt, T. (1999). A Planetary-Scale to Mesoscale Perspective of the Life Cycles of Extratropical Cyclones: The Bridge between Theory and Observations. In *The Life Cycles of Extratropical Cyclones*, pages 139–186. Amer. Meteorol. Soc., Boston.
- Shutts, G. J. and Thorpe, A. J. (1978). Some aspects of vortices in rotating stratified fluids. *Pure Appl. Geophys.*, **116**, 993–1006.
- Simmons, A. J. and Hoskins, B. J. (1976). Baroclinic instability on the sphere: Normal modes of the primitive and quasi-geostrophic equations. *J. Atmos. Sci.*, **33**, 1454–1477.
- Simmons, A. J. and Hoskins, B. J. (1977). Baroclinic instability on the sphere: Solutions with a more realistic tropopause. *J. Atmos. Sci.*, **34**, 581–588.

- Simmons, A. J. and Hoskins, B. J. (1978). The life cycles of some nonlinear baroclinic waves. *J. Atmos. Sci.*, **35**, 414–432.
- Sinclair, M. R. and Watterson, I. G. (1999). Objective assessment of extra-tropical weather systems in simulated climates. *J. Climate*, **12**, 3467–3485.
- Sinclair, V. A., Gray, S. L., and Belcher, S. E. (2008). Boundary-layer ventilation by baroclinic life cycles. *Q. J. R. Meteorol. Soc.*, **134**, 1409–1424.
- Sinclair, V. A., Gray, S. L., and Belcher, S. E. (2010a). Controls on boundary-layer ventilation: Boundary-layer processes and large-scale dynamics. *J. Geophys. Res.* doi:10.1029/2009JD012169.
- Sinclair, V. A., Belcher, S. E., and Gray, S. L. (2010b). Synoptic controls on boundary-layer characteristics. *Boundary-Layer Meteorol.*, **134**, 387–409.
- Smith, R. N. B. (1990). A scheme for predicting layer clouds and their water content in a general circulation model. *Q. J. R. Meteorol. Soc.*, **116**, 435–460.
- Smith, S. D. (1988). Coefficients for sea surface wind stress, heat flux and wind profiles as a function of wind speed and temperature. *J. Geophys. Res.*, **93**, 15467–15472.
- Staniforth, A., White, A., Wood, N., Thuburn, J., Zerroukat, M., Cordero, E., and Davies, T. (2005). Joy of UM 6.1 - Model Formulation. *Unified Model Documentation Paper*, **15**.
- Stoelinga, M. T. (1996). A potential vorticity-based study of the role of diabatic heating and friction in a numerically simulated baroclinic cyclone. *Mon. Weather Rev.*, **124**, 849–874.
- Stohl, A., Forster, C., and Sodemann, H. (2008). Remote sources of water vapour forming precipitation on the Norwegian west coast at 60°N - a tale of hurricanes and an atmospheric river. *J. Geophys. Res.*, **113**, D05102.
- Takemi, T. (2006). Impacts of moisture profile on the evolution and organization of midlatitude squall lines under various shear conditions. *Atmos. Res.*, **82**, 37–54.
- Taylor, P. K. and Guymer, T. H. (1983). The structure of an atmospheric warm front and its interaction with the boundary layer. *Phil. Trans. R. Soc. Lond. A*, **308**, 341–358.

- Thorncroft, C. D., Hoskins, B. J., and McIntyre, M. E. (1993). Two paradigms of baroclinic-wave life-cycle behaviour. *Q. J. R. Meteorol. Soc.*, **119**, 17–55.
- Troen, I. and Mahrt, L. (1986). A simple model of the atmospheric boundary layer; sensitivity to surface evaporation. *Boundary-Layer Meteorol.*, **37**, 129–148.
- Valdes, P. J. and Hoskins, B. J. (1988). Baroclinic Instability of the Zonally Averaged Flow with Boundary Layer Damping. *J. Atmos. Sci.*, **45**, 1584–1593.
- Wernli, H., Fehlmann, R., and Lüthi, D. (1998). The effect of barotropic shear on upper-level induced cyclogenesis: Semigeostrophic and primitive equation numerical simulations. *J. Atmos. Sci.*, **55**, 2080–2094.
- Whitaker, J. S. and Davis, C. A. (1994). Cyclogenesis in a saturated environment. *J. Atmos. Sci.*, **51**, 889–907.
- Williams, G. P. and Robinson, J. B. (1974). Generalized Eady Waves with Ekman Pumping. *J. Atmos. Sci.*, **31**, 1768–1776.
- Wilson, D. R. and Ballard, S. P. (1999). A microphysically based precipitation scheme for the Meteorological Office Unified Model. *Q. J. R. Meteorol. Soc.*, **125**, 1607–1636.
- Zhu, Y. and Newell, R. (1994). Atmospheric rivers and bombs. *Geophys. Res. Lett.*, **21**, 1999–2002.
- Ziemianski, M. (1994). Potential vorticity inversion. *Joint Centre for Mesoscale Meteorology (JCMM) Internal Report*, **39**. University of Reading, Reading, UK.